UNIVERSITAT DE BARCELONA

Role of the TGFβ-NOX4 axis in the liver tumour microenvironment

Rut Espinosa Sotelo

Role of the TGF-β – NOX4 axis in the liver tumour microenvironment

This thesis is submitter to University of Barcelona and presented ***Rut Espinosa Sotelo*** *to obtain de degree of Doctor by University of Barcelona. This work has been developed at Bellvitge Biomedical Research Institute (IDIBELL) under the supervision of* ***Dr. Isabel Fabregat Romero*** *and* ***Dr. Esther Bertran Rodríguez****.*

Dr. Isabel Fabregat Romero

Rut Espinosa Sotelo

Dr. Esther Bertran Rodríguez

TGF-β and Cancer group

Oncobell program, IDIBELL

Doctoral Program in Biomedicine

University of Barcelona

This work has been developed at the Rosalind Franklin Area at IDIBELL (L'Hospitalet de Llobregat, Barcelona).

The author enjoyed the following financial support:

- FPI predoctoral grant from the Agencia Estatal de Investigacion, Ministerio de economia y competitividad (MINECO). Ref: PRE2019-089144; Associated to the project with reference: RTI2018-094079-B-I00. Period: 2016-2019.

This thesis has been possible thanks to the financial support for of the following companies and institutions:

- Agencia Estatal de Investigacion, Ministerio de Innovacion y Universidades (MICINN), Spain, cofounded by FEDER funds/European Regional Development Fund– a way to build Europe (2016-2019). Project: Nuevas aproximaciones experimentales para analizar el papel de la NADPH oxidasa NOX4 en regeneracion y cancer hepaticos. Relacion con la via del TGF-beta. Reference: RTI2018-094079-B-100.
- Agencia Estatal de Investigacion, Ministerio de Ciencia, Innovacion y Universidades (MICINN). Acciones de dinamizacion 'redes de investigacion' (2020- 2023). Project: Redox Biology and Medicine. Reference: RED2018-102576-T
- Agencia Estatal de Investigacion, Ministerio de Innovacion y Universidades (MICINN), Spain, cofounded by FEDER funds/European Regional Development Fund– a way to build Europe (2021-2023). Project: Descifrando el papel de la NADPH oxidasa NOX4 en el carcinoma hepatocelular: relevancia en celulas tumorales y estroma y relacion con la via del TGF-beta. Reference: PID2021-122551OB-I00
- Fundación Asociación Española Contra el Cáncer (AECC), Spain (2021-2024). Project: Towards a precision medicine using TGF-β inhibitors in hepatocellular carcinoma and cholangiocarcinoma. Reference: PRYGN211279FABR
- Agència de Gestió d'Ajuts Universitaris i de Recerca (AGAUR), Generalitat de Catalunya, Spain (2021-2024). Project: Role of TGF-beta and the oxidative stress in human pathologies. Reference: 2021SGR00029
- The CIBEREHD, National Biomedical Research Institute on Liver and Gastrointestinal Diseases, funded by the Instituto de Salud Carlos III, Spain (2018). Project: "Cellular signaling in liver regeneration and carcinogenesis". Reference: CB17/04/00017.

We thank the Generalitat de Catalunya through the CERCA Programme.

A tot I tothom que m'ha portat fins on sóc ara,
a la meva família i al meu amor

ABBREVIATIONS

2D	Two-dimensional
3D	Three-dimensional
ABB	Annexin binding buffer
ATP	Adenosine triphosphate
ATPb	ATP synthase subunit beta
BID	BH3-interacting domain
BMP	Bone morphogenetic proteins
BSA	Bovine serum albumin
CAF	Cancer associated fibroblasts
CCl4	Carbon tetrachloride
CDK	Cyclin-dependent kinase
CEB	Cytoplasmic extraction buffer
CEIC	Comité Ético de Investigación Clínica
CLCF1	Cardiotrophin-like cytokine factor 1
CM-H_2DCFDA	2′,7′-dichlorodihydrofluorescein diacetate
Co-SMAD	Cooperating SMAD
DAB	Diaminobenzidine
DAMP	Damage-associated molecular pattern
DAPI	4’,6-diamidino-2-phenylindole
DEG	Differentially Expressed Genes
DEN	Diethylnitrosamine
DPI	Diphenyleneiodonium
DR	Death receptor
DUOX	Dual oxidase
ECM	Extracellular matrix
EDTA	Ethylenediaminetetraacetic acid
EGF	Epidermal growth factor

EGFR	Epidermal growth factor receptor
EMT	Epithelial-to-Mesenchymal Transition
ER	Endoplasmic reticulum
ETC	Electron transport chain
FAD	Flavine adenine dinucleotide
FBS	Foetal bovine serum
GAPDH	Glyceraldehyde-3-phosphate dehydrogenase
GDF	Growth and differentiation factor
gRNA	Short-guide RNA
GSVA	Gene set variation analysis
H&E	Haematoxylin and Eosin staining
H_2O_2	Hydrogen peroxide
HBSS	Hank's balanced salt solution
HCC	Hepatocellular carcinoma
HGF	Hepatocyte growth factor
HIF-1α	Hypoxia-Inducible Factor 1α
HRP	Horseradish Peroxidase
HSC	Hepatic stellate cells
Hsp70	Heat shock protein 70
HUB	Bellvitge university hospital
IEB	Isotonic Extraction Buffer
IF	Immunofluorescence
I-SMAD	Inhibitory SMAD
KC	Kupffer cells
KD	Knock-down
KO	Knock-out
MEB	Membrane extraction buffer

MFB	Myofibroblast
MIF	Migration inhibitory factor
MMP	Matrix metalloprotease
MOMP	Mitochondrial outer membrane permeabilization
NADPH	Nicotinamide adenine dinucleotide phosphate hydrogen
NAFLD	Non-alcoholic fatty liver disease
NASH	Non-alcoholic steatohepatitis
NEB	Nuclear extraction buffer
NOX	NADPH oxidase
NOXA1	NOX activator 1
NOXO1	NOX organizer 1
NT	Non-tumour
O_2	Molecular oxygen
$O_2^{\cdot-}$	Superoxide anion
OS	Overall survival
PBS	Phosphate-buffered saline
PBS-T	PBS-tween
PEB	Pellet extraction buffer
PFA	Paraformaldehyde
PI	Propidium iodide
PI3K	Phosphatidylinositol-3-kinasa
PMF	Post Mitochondrial fraction
Rb	Retinoblastoma protein
RNS	Reactive nitrogen species
ROS	Reactive oxygen species
R-SMAD	Receptor-associated SMAD
RT	Room temperature

RTCA	Real-time cell analyser
RT-qPCR	Real Time Quantitative Polymerase Chain Reaction
SBE	SMAD-binding elements
SD	Standard deviation
SDS	Sodium dodecyl sulfate
shRNA	Short hairpin RNA
siRNA	Small interference RNA
T	Tumour
TACE	TNFα-converting enzyme
tBID	Truncated BID
TCGA	The cancer genome atlas
TCGA-LIHC	TCGA liver hepatocellular carcinoma
TF	Transcription factor
TGF-β	Transforming Growth Factor-beta
TGF-β R	Transforming growth factor-beta Receptor
TME	Tumour microenvironment
TNFα	Tumour necrosis factor-α
TRAIL	TNF-related apoptosis-inducing ligand
VSMC	Vascular smooth muscle cells
WB	Western blot
WT	Wild type
ID	Inhibitor of DNA-binding
PP2A	Protein phosphatase 2A
APAF1	Apoptotic protease activating factor 1
BH3	BCL-2 homology domain 3
FADD	FAS-associated death domain protein
SMAC	Second mitochondria-derived activator of caspases

MCL1	Myeloid cell leukaemia 1
ERK	Extracellular signal-regulated kinase
MEK	Mitogen-activated protein kinase (MAPK)/ERK kinase
SOD	Superoxide dismutase
UPR	Unfolded Protein Response
CTGF	Connective tissue growth factor
CXCL	C-X-C Motif Chemokine Ligand
IHQ	Immunohistochemistry
PMSF	Phenylmethylsulfonyl fluoride
CNAG	Centro Nacional de Análisis Genómico
FoxP3	Forkhead box 3
Treg	Regulatory T cell
Th	T helper
TAM	Tumour Associated Macrophage
NES	Normalized Enrichment Score
PC	Principal Component
TIMER	Tumor Immune Estimation Resource
TPM	Transcripts per million
PCA	Principal Component Analysis
FAK	Focal Adhesion Kinase

TABLE OF CONTENTS

INTRODUCTION

1. Hepatocellular carcinoma

Nowadays, hepatocellular carcinoma (HCC) is the fourth leading cause of cancer-related deaths worldwide, since it accounts for most primary hepatic cancers (80-90%)[1,2,3]. Patients present a low overall survival rate and limited therapeutic options, thus making HCC a global health challenge, even in developed countries[3,4].

HCC is the ultimate consequence of having an underlying liver disfunction for a long period of time. Chronic inflammatory insults can potentially lead to cirrhosis, which is the last step to unresolved hepatic fibrosis and the biggest risk factor for HCC[3,5]. Geographical differences are found in the aetiology of HCC depending on the global distribution of the genetic and environmental risk factors. These include chronic viral infection, mainly Hepatitis B and Hepatitis C[6], chronic alcohol consumption, non-alcoholic steatohepatitis (NASH) or non-alcoholic fatty liver disease (NAFLD), mainly from diabetes or obesity, age and gender[2,3,4,5].

Fortunately, oncological treatments for HCC have improved during the last years. Early-stage tumour patients can be cured surgically, by liver resection, local ablation or organ transplantation. Those patients in an intermediate stage diagnosis usually are candidates for radiotherapy or transarterial chemo/radioembolization[7,8]. Nevertheless, advanced-stage HCC patients are potential candidates for systemic therapies, such as immunotherapy (atezolizumab), tyrosine kinase inhibitors (sorafenib, lenvatinib) or a combination of both[3,7,8]. Unfortunately, patients are often diagnosed in advanced stages, when HCC is already unresectable, and the liver failure symptoms are present. This overall health situation makes the treatment by systemic therapies more complex and fail-prompt. In consequence, further investigating the altered molecular and cellular mechanisms and pathways in HCC is of outmost importance for the development of future personalized therapies that will treat the disease with efficiency.

Molecular mechanisms involved in hepatocarcinogenesis are not completely elucidated yet. However, the identification of some genetic alterations has been possible due to great effort made. HCC onset is a multistep process that involves several subsequent mutations in genes

that control cellular proliferation and/or apoptosis, among others. For instance, some gene mutations affect the cell cycle, such as *TP53* in about 30% of HCC patients; others affect the Wnt-β-catenin signalling (*CTNNB1* activating alteration, or *AXIN1* or *APC* inactivating mutations); others the chromatin remodelling (*ARID1A* or *ARID2*)[9]. Besides, almost 60% of HCC patients present mutations in *TERT* promoter, which affect the telomere maintenance[10,11,9]. Additionally, oxidative stress response pathways can be constitutively active by activating alterations in *NFE2L2* (gene for Nuclear Factor Erythroid 1-related Factor (NRF2)) or inactivating alterations in *KEAP1*[12], its inhibitor. Finally, in approximately 10% of HCC cases a chromosomal amplification of c-MYC is also found, resulting in overexpression of the oncogene (*see section 1.1*)[13,14].

2. Transforming Growth Factor-Beta in the liver

Transforming Growth Factor-beta (TGF-β) is a superfamily of pleiotropic cytokines that has an enormous number of roles in embryogenesis and adult tissue homeostasis. Besides, they are often implicated in pathophysiological mechanisms that cause a wide range of diseases under a malfunction[15,16]. The family consists of thirty-three multifunctional genes that include the TGF-β subfamily, activins, inhibins, bone morphogenetic proteins (BMP) and growth and differentiation factors (GDFs)[16, 17].

The most relevant members of the TGF-β family are comprised of three isoforms (TGF-β1, TGF-β2 and TGF-β3) which are synthesized as a latent pro-form. After this, they are secreted and anchored to the extracellular matrix (ECM) in excess, so the bioavailability limiting step is its activation[17, 18]. In the liver, several cell types produce and secrete TGF-β. Specifically, Hepatic Stellate Cells (HSCs), Kupffer Cells (KCs) and platelets do, but is also expressed by regenerating hepatocytes or tumoral cells[19, 20, 21].

2.1 TGF-β signalling pathway

TGF-β signalling has important roles in the regulation of several cellular processes, such as differentiation, proliferation, migration, cell death... all of them essential for tissue homeostasis[17], particularly in the liver, on which our group has focused its research. TGF-β can contribute to homeostasis by its tumour suppressor role in healthy tissues but can also drive cancer progression in neoplastic tissues[22,23].

Specifically in hepatocytes, TGF-β can have a tumour suppressive effect, partially due to Nicotinamide adenine dinucleotide phosphate hydrogen (NADPH) oxidase (NOX) NOX4 upregulation. This pleiotropic cytokine induces growth inhibition by cell cycle arrest and by counteracting the proliferative signals such as Epidermal growth factor (EGF) or Hepatocyte growth factor (HGF). It also can promote the downregulation of c-Myc, a well-known oncogenic transcription factor involved in cellular proliferation[24]. Furthermore, TGF-β induces apoptosis through the production of Reactive oxygen species (ROS), by inducing NOX4 expression. All these processes will be further revised in greater detail in the following sections.

As TGF-β has pleiotropic effects that are utterly important for homeostasis maintenance, its activity is strictly controlled. Different mechanisms account for this tight regulation:

- Prevention of the binding of the ligands to the receptors
- TGF-β Receptor (TGF-βR)III, acts as a coreceptor that regulates the presentation of the ligands to the tetrameric TGF-β receptors
- Inhibitory SMADs, such as SMAD7
- Cell surface distribution of the receptors to control of the TGF-β response
- Post-translational modification of the SMADs and the TGF-βR

2.2 SMAD-dependent signals

The canonical pathway of TGF-β is a membrane-to-nucleus signalling pathway that involves SMAD family. Humans express eight SMAD proteins, that are classified in: Receptor-associated SMADs (R-SMADs), like SMAD2 and SMAD3; Cooperating SMADs (Co-SMADs), such as SMAD4; and Inhibitory SMADs (I-SMADs), like SMAD6 and SMAD7[16, 25].

Activated dimeric TGF-β ligands bind to transmembrane homodimeric TGF-βRII, which is constitutively active and acts as a high-affinity receptor (**Figure III**). This interaction generates a conformational adaptation, and a new binding site is created for TGF-βRI. Then, TGF-βRII phosphorylates serine residues of TGF-βRI in the juxtamembrane domain, thus forming an heterotetrameric transmembrane serine/threonine kinase membrane receptor. Thereafter, activated TGF-βRI phosphorylates, in turn, SMAD2 and SMAD3 (R-SMADs) in the carboxy-terminal, that associate with SMAD4 (Co-SMAD). This trimeric complex translocates into the nucleus, where it will enhance the expression of the target genes, either by binding to SMAD-binding elements (SBEs) or by pairing up with other co-activators and transcription factors (TF). Initiation and propagation of TGF-β signalling can be counteracted by the I-SMADs, such as SMAD7[26, 27, 16, 28, 25].

Besides transcriptional regulation, interaction of SMADs with specific transcription factors and co-regulators enables them to regulate gene expression by alternative mechanisms including epigenetic remodeling, RNA splicing and miRNA processing[29].

2.2.1 TGF-β in growth inhibition

TGF-β is a cytokine that has a dual inhibitory effect on growth, as it acts in two different approaches. On one hand, the cytokine induces the inhibition of the cell cycle progression of G_1 phase. This is done by the regulation of cyclin-dependent kinase (CDK) inhibitors through the canonical Smad-signalling pathway, which depend on the cell type (**Figure I**). In epithelial cells, TGF-β induces the expression of $p21^{cip1}$, an inhibitor of Cyclin E/B-Cdk2 complex, and of $p15^{ink4b}$, an inhibitor of Cyclin D-cdk4/6 complex[30], by increase in transcriptional activation

when the SMAD3/4 complex targets the respective promoters. Therefore, TGF-β antagonizes CDKs activation in early G_1 phase, that brings to an inhibition of the phosphorylation of retinoblastoma protein (pRb) and cell cycle arrest. On the other hand, it regulates the TGF-β-induced downregulation of Myc by co-repressors recruitment in the *MYC* promoter, a transcription factor involved in cellular proliferation, and Inhibitor of DNA-binding (ID) protein 1-3, involved in inhibition of cell differentiation[31,22,32].

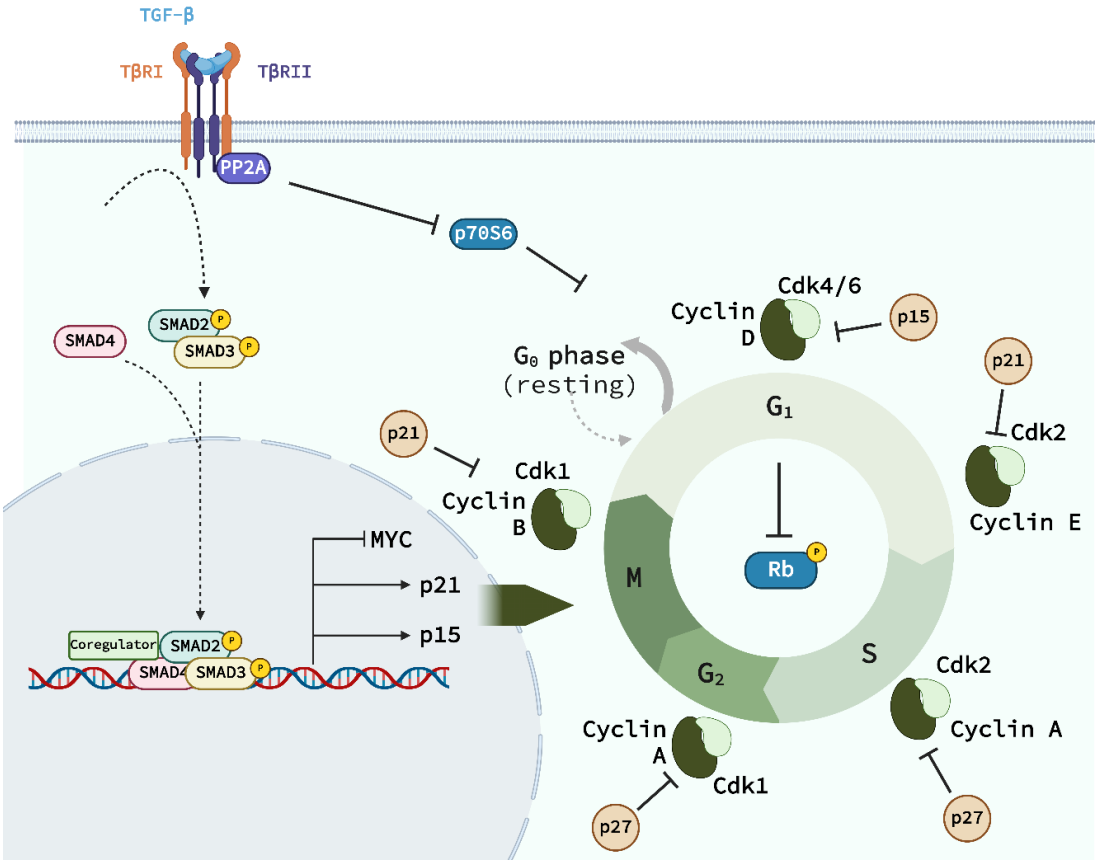

Figure I. TGF-β-mediated growth inhibition. After the trimeric complex SMAD2/3-SMAD4 binds to DNA promoters, transcription of p21 and p15 increases. This increases the inhibition of Cyclin/Cdk complexes, arresting the cell cycle. Besides, SMADs complex can recruit co-repressors to *MYC* promoter, inhibiting its expression. Image created with BioRender. Adapted from: Bai J, et al. Cancer Biol Med, 2017. Decker JT, et al. Cancers, 2021. Moustakas A, et al. J Cell Sci, 2005.

Apart from these regulatory pathways, TGF-β can also promote cell cycle arrest by SMAD-independent mechanisms. Indeed, the binding of the TGF-β-R complex to the regulatory subunit Protein phosphatase 2A (PP2A), induces p70S6 kinase dephosphorylation

and inhibition[33,34]. Cell cycle arrest has also been described in hepatocytes at low dosage of TGF-β[35].

The cytostatic effects are often lost in tumoral cells, that acquire resistance to the action of certain cytokines. In this case, mutations to components of the TGF-β pathway, such as SMAD2, SMAD4 or TGF-βRII, can cause dysregulation of the signalling[36]. Besides, some cancers overexpress c-Myc or Cyclin D1 to counteract the action of CDK inhibitors[22,27]. Additionally, our group described an alternative non-SMAD pathway, where TGF-β induces survival signals by transactivating EGF Receptor (EGFR) pathway, which will be further discussed in this thesis (*see section 2.3.1*).

2.2.2 TGF-β in apoptosis

Apoptosis is a major programmed cell death, crucial for maintaining tissue homeostasis, in which TGF-β also has a role. One of the hallmarks of the apoptosis process is the protease activity of caspases. In broad terms, caspases can be activated through one of two pathways — the extrinsic (or death receptor) pathway and the intrinsic (or mitochondrial) pathway (**Figure II**).

On one hand, extrinsic pathway starts by external stimulation, as the name indicates, via a death receptor (DR) family member, such as the Tumour necrosis factor (TNF)-related apoptosis-inducing ligand (TRAIL). After ligand binding, death receptors activate caspases, leading to widespread cleavage of caspase substrates and rapid cell death[37].

On the other hand, intrinsic apoptotic pathway engages several intracellular stimuli that act as stress or damage indicators. All of those converge to a key event that triggers the rest of the apoptotic cascade, the mitochondrial outer membrane permeabilization (MOMP)[38]. After the mitochondrial permeabilization, cytochrome c is released from the intermembrane space. This situation triggers the caspase activation via the apoptosome, a cytoplasmic complex formed by apoptotic protease activating factor 1 (APAF1)[39,40,41]. However, once MOMP is activated, it is hardly irreversible. That is the reason why MOMP is strictly regulated by the

BCL-2 family members[42]. There are three subfamilies of BCL-2 proteins: anti-apoptotic (BCL-2, BCL-xL and Myeloid cell leukaemia 1 (MCL1)), pro-apoptotic BCL-2 homology domain 3 (BH3)-only proteins (PUMA, BID and BIM) and pro-apoptotic effector proteins (BAX and BAK). BH3-only proteins give different signals that activate BAX and BAK at the mitochondrial outer membrane, where they trigger MOMP[43]. On the contrary, anti-apoptotic BCL-2 proteins inhibit cell death by binding directly to activated BAX and BAK, or to BH3-only proteins[44]. Both pathways also can crosstalk through caspase-8 cleavage of the BH3-only protein BH3-interacting domain death agonist (BID), which generates the active, truncated form of BID (tBID) that triggers MOMP[45,42]. It is worth remarking that intrinsic pathway is often deregulated in cancer.

In hepatocytes, TGF-β has been described to modulate the expression of different members of the BCL-2 family. On one hand, it can induce the downregulation of anti-apoptotic proteins, like Bcl-xL in rat foetal hepatocytes[46]. On the other hand, TGF-β can also induce upregulation of pro-apoptotic proteins in liver cells, specifically BIM and BAX[47,48]. Importantly, TGF-β-induced apoptosis has been linked with its induced ROS production in hepatocytes[35], as it is necessary for the efficient mitochondrial-dependent apoptosis[49,50]. The levels of ROS depend on different mechanisms. Among others, one mechanism is the decrease of antioxidant proteins[51], and the other one the induction of NOXs, in specific, the induction of NOX4, to increase extra-mitochondrial ROS[52,51]. Consequently, TGF-β-NOX4 axis shows to be an important pathway in regulating this potential tumour suppressor function, which will be further explored in this thesis.

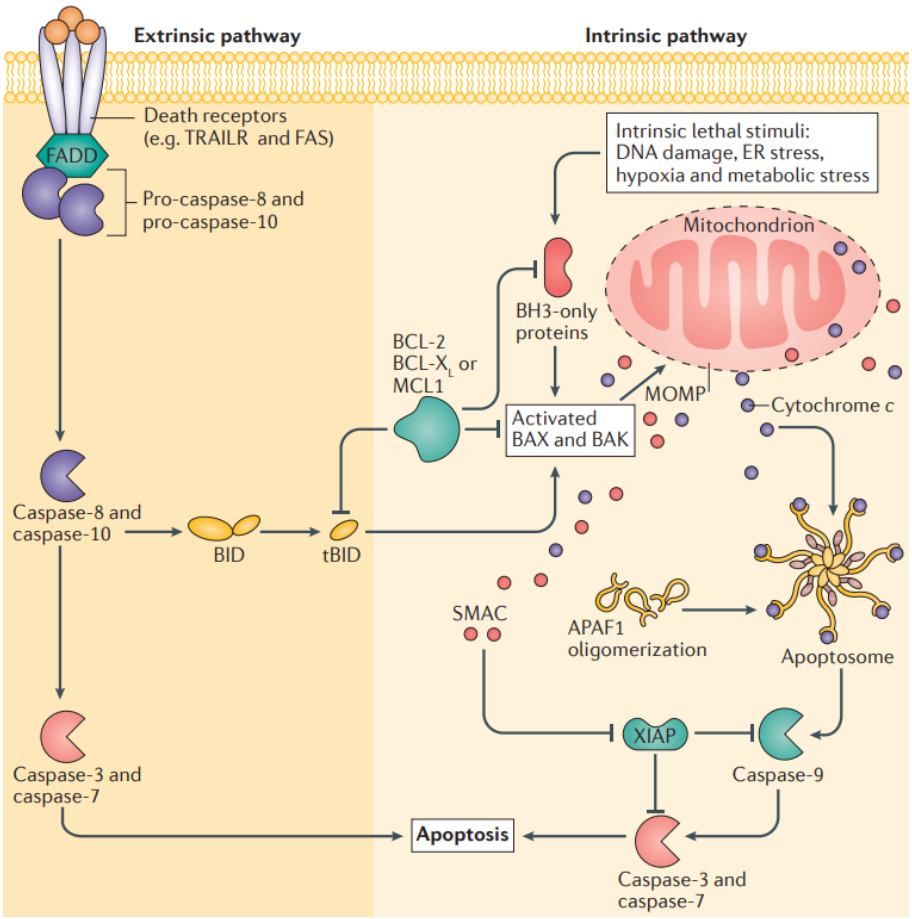

Figure II. Extrinsic and intrinsic apoptotic signalling pathways. In the extrinsic apoptotic pathway, upon binding to their cognate ligand, death receptors such as TRAIL receptor and FAS can activate initiator caspases (caspase-8 and caspase-10) through dimerization mediated by adaptor proteins such as FAS-associated death domain protein (FADD). Active caspase-8 and caspase-10 then cleave and activate the effector caspase-3 and caspase-7, leading to apoptosis. The intrinsic pathway of apoptosis requires MOMP. Cell stresses engage BH3-only protein activation, leading to BAX and BAK activity that triggers MOMP. Anti-apoptotic BCL-2 family proteins counteract this. Following MOMP, mitochondrial intermembrane space proteins such as second mitochondria-derived activator of caspases (SMAC) and cytochrome c are released into the cytosol. Cytochrome c interacts with APAF1, triggering apoptosome assembly, which activates caspase-9. Active caspase-9, in turn, activates caspase-3 and caspase-7, leading to apoptosis. Mitochondrial release of SMAC facilitates apoptosis by blocking the caspase inhibitor X-linked inhibitor of apoptosis protein (XIAP). Caspase-8 cleavage of the BH3-only protein BID enables crosstalk between the extrinsic and intrinsic apoptotic pathways. Extracted from: Ichim, G. Nat Rev Cancer, 2016.

2.3 SMAD-independent signals

Apart from the canonical pathway, TGF-β can also activate several non-SMAD or non-canonical signalling pathways[29, 53]. One of the most important ones, though, is the crosstalk with EGFR pathway, that involves Phosphatidylinositol-3-kinasa (PI3K)/AKT signalling (**Figure III**). Due to its relevance for this thesis, this pathway will be further explained in the next section. Nevertheless, as mentioned before, TGF-β not only can activate EGFR signalling pathway, but others, too. For instance, RHO small GTPases can also be activated, which leads to an actin cytoskeleton remodelling[29].

2.3.1 Crosstalk with EGFR pathway

TGF-β can induce survival signals, which correlates with the fact that *TGFB1* is overexpressed in several types of cancer that correlate with a poor prognosis. In the liver, TGF-β acts at first as a tumour suppressor in early stages of tumour development. However, once the cells become resistant to its cytostatic effects, TGF-β favours the tumour progression[21]. This shift can be explained by the activation of the EGFR in HCC late stages, where NOX1 also plays a role in transactivating the receptor, via upregulation of TGF-β[54,55]. EGFR pathway activation by EGF ligand binding, activates PI3K/AKT signalling, which in the end counteracts the TGF-β-induced NOX4 upregulation and mitochondrial-dependent apoptosis[52,56]. Besides, overactivation of survival signals, like the Mitogen-activated protein kinase/ERK kinase (MEK)/Extracellular signal-regulated kinase (ERK) pathway, impairs the upregulation of NOX4, conferring resistance to cell death[57]. Therefore, EGF impairs TGF-β-induced cell death effects in hepatocytes[56,35]. Indeed, when EGFR signalling was blocked, the apoptotic response to TGF-β was increased[58,55], and correlated with higher NOX4 levels[59]. In fact, TGF-β was found to be a mediator of EGFR ligands production, where the activity of metalloprotease TNFα-converting enzyme (TACE)/ADAM17 is needed to shed the ligands[58,60]. Caveolin-1 is needed for the activation of TACE/ADAM17 by TGF-β in hepatocytes, which require the activation of SRC and NOX1[61,62]. And last, Clathrin expression is also required for TGF-β-

induced anti-apoptotic signals in liver tumour cells[63]. Overall, NOX1 and NOX4 exert contrary roles in the control of liver growth and apoptosis and their balance may dictate cell fate[64].

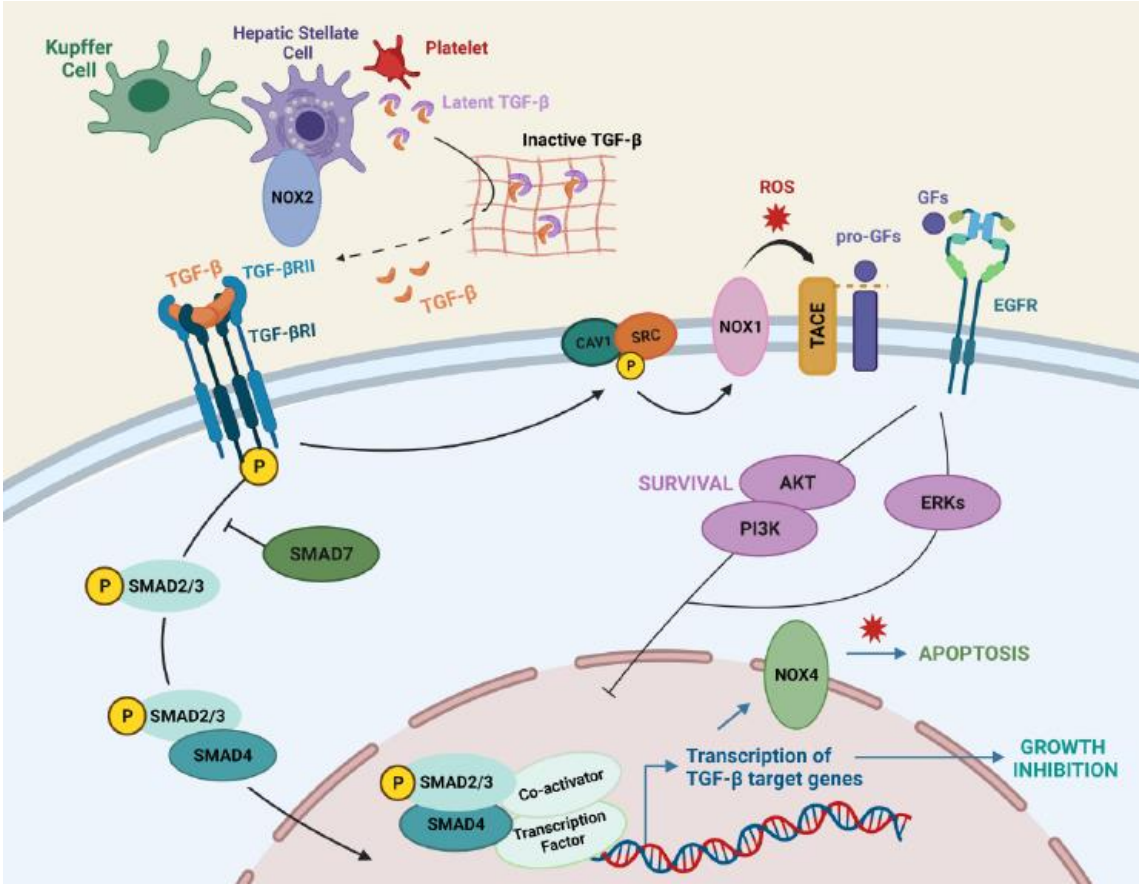

Figure III. TGF-β signaling in liver cells. TGF-β is synthesized by hepatic stellate cells, kupffer cells and platelets, and anchored to the ECM in a latent form. Once active, TGF-β binds TGFβRII, which recruits TGFβRI, inducing Smad phosphorylation and nuclear translocation, where transcription of target genes occurs. TGF-β-induced shedding of the EGF family of growth factors requires the activation of TACE/ADAM17 in a Caveolin-1/Src/NOX1 dependent manner. Extracted from: Herranz-Itúrbide M, Cells, 2021.

Paradoxically, depending on the cell-type and the environmental factors, TGF-β can simultaneously induce both pro-survival and pro-apoptotic signals.

2.4 TGF-β signalling in migration

As revised in these last sections, TGF-β in liver carcinogenesis is known to play a dual role. At early stages, TGF-β may induce apoptosis and inhibit cell growth. Nevertheless, once the cells become resistant to TGF-β-induced suppressor actions, tumour cells respond to this

cytokine by promoting migration and invasion[21]. In fact, in HCC cell lines, a high autocrine TGF-β expression has been found to correlate with a more mesenchymal and migratory phenotype[65].

Migration and invasion are strictly regulated by several mechanisms, like the Epithelial-to-Mesenchymal Transition (EMT) program. EMT consists of a process in which epithelial cells acquire mesenchymal cell characteristics, often accompanied with an increased stem-like and tumour-initiating actions, resistance to apoptotic stimuli, increased invasive and metastatic phenotypes[66]... Classically, epithelial cells are characterized by being positioned in a basement membrane, have an apical-basal polarity and intercellular junctions. EMT programme is, generally, really conserved, although some variability can be found depending on the cell type or context[67]. In the end, cell-to-cell contacts and their polarity are lost.

Moreover, gene expression of junction proteins such as E-Cadherin, ZO-1 and occluding is downregulated, whereas the expression of N-Cadherin is increased, as a mesenchymal adhesion protein. Several transcription factors regulate EMT gene programme, like SNAIL/SLUG, ZEB1/2 and TWIST, in response to TGF-β. Those will, in turn, repress the expression of epithelial markers, but promote the expression of mesenchymal ones[68,69,70]. Apart from the EMT-related genes, another mechanism to regulate migration is to modify the cytoskeleton. Phenotypical changes induced by actin cytoskeleton, microfilaments, microtubules and intermediate filaments remodelling lead to an increased motility. Additionally, cells typically gain invasive properties through increased expression and secretion of metalloprotease proteins (MMP)[66,67,71].

In the liver, in foetal hepatocytes, TGF-β was seen to induce EMT in those cells that survived its apoptotic effects[72]. In an hepatocarcinogenic environment, epithelial cells might undergo EMT, favouring intravasation of cells to blood or lymph vessels to disseminate and metastasize. Interestingly, cancer cells can undergo EMT in different extents, retaining epithelial features while gaining some mesenchymal ones. In this sense, TGF-β may induce a partial EMT, increasing the expression of mesenchymal genes while maintaining epithelial

gene expression[73,69]. For instance, the epithelial HCC cell line PLC/PRF/5 responds to the cytokine by inducing migration but maintaining epithelial characteristics without induction of the transcriptomic EMT program[65]. Importantly, in the absence of the cytokine, cells that had undergone TGF-β-induced EMT, revert to an epithelial phenotype again, process known as mesenchymal-to-epithelial transition (MET)[74].

Of note is that both SMAD-dependent and -independent signalling play a role in TGF-β-induced EMT reprogramming. On one hand, SMAD3 and SMAD4 act as promoters of the EMT program, while SMAD2 acts as a negative regulator, by transcriptionally regulating gene expression[75]. On the other hand, activation of PI3K-AKT pathway and small GTPases like RhoA, RhoC or cdc42, TGF-β increases motility and actin reorganization[71,66,70]. There is a connection between apoptosis and EMT by TGF-β, not only because EMT depends on cells overcoming apoptotic effects of TGF-β, but also because EMT induces survival signals that can rescue from apoptosis[74,76]. Indeed, SNAIL overexpression confers resistance to TGF-β-induced pro-apoptotic actions[77,78]. To further emphasize the crosstalk between EGF and TGF-β, it has been seen that EMT confers resistance to the suppressor arm by increasing the expressions of EGFR ligands, activating this pathway[79].

NOX4 had been found to be localized in focal adhesions, as will be explained in *section 3.3.2* and plays a critical role in cytoskeleton remodelling. Focal adhesions are specialized structures that link the extracellular matrix to the cytoskeleton, important for signal transduction and cellular responses to the external environment. NOX4 is involved in the production of ROS, which regulate the dynamics of focal adhesions. The localization of NOX4 to focal adhesions is essential for its function in modulating the activity of various focal adhesion proteins, such as paxillin and focal adhesion kinase (FAK), which are critical for cell migration and adhesion[80]. Additionally, NOX4-mediated ROS production influences the reorganization of the actin cytoskeleton, promoting changes in cell shape and motility. This interplay between NOX4 activity and cytoskeletal dynamics is crucial for various physiological processes, including wound healing and tissue regeneration[81,82]. One of the proposed

mechanisms by which TGF-β - NOX4 axis regulates focal adhesions is through the increase of Hic-5 expression and localization in the focal adhesions, as demonstrated in Vascular Smooth Muscle Cells (VSMC). NOX4 mediated the TGF-β-induced increase in the chaperone Hsp27, which is a target of NOX4-mediated gene transcription required for correct subcellular localization of Hic-5 within focal adhesions. This process is crucial for the TGF-β-mediated promotion of focal adhesions number, maturation and migration[83].

3. NADPH oxidases

The NOX family has emerged in the last years as an important source of ROS in signal transduction[84]. The NOX family consists of seven isoforms: NOX1-5 and two dual oxidases DUOX1-2. All members are characterized by the reduction of molecular oxygen (O_2) using NADPH as an electron donor as their enzymatic activity, producing ROS. Although they share analogies in structure and catalytic action, NOX enzymes differ in their activity and the ROS type generated. On one hand, NOX1, NOX2, NOX3 and NOX5 primarily produce superoxide anion ($O_2^{\cdot-}$), which is then converted to hydrogen peroxide (H_2O_2), either spontaneously or by enzymatic action[85]. On the other hand, NOX4, DUOX1 and DUOX2 directly produce H_2O_2[84, 86, 87].

3.1 Reactive oxygen species

ROS are a heterogeneous group of short-lived molecules that derive from a partial reduction of O_2. O_2 contains two unpaired electrons in parallel spins, so its reduction comprises the transfer of single electrons, provoking the formation of free radicals. Consequently, free radicals are characterized for having an unpaired electron in the outer orbital, which is an unstable configuration, making them highly reactive molecules with the ability to change proteins and nuclei acids[88, 89]. Oxygen reduction products can be classified into those that have a free electron, like $O_2^{\cdot-}$, and the two-electron reduction product, such as H_2O_2, which are more stable molecules and not considered of a free radical nature[88, 90, 91].

Although there are alternative ROS sources, the two fundamental endogenous ones are NADPH oxidases and mitochondrial electron transport chain (ETC)[92, 90,93].

NOX-derived ROS may modulate gene expression, cytoskeleton remodelling, migration, differentiation, as well as cell proliferation and death[84, 94]. In consequence, NOXs are key for maintaining homeostasis and their dysregulation can cause oxidative stress or altered cellular responses, leading to pathological consequences, such as cancer and metabolic, cardiovascular or neurodegenerative diseases[88,95, 96].

Hydrogen peroxide

Even though H_2O_2 is quite stable and uncharged, its intracellular concentration needs to be tightly controlled, as ROS have been seen to act as signalling molecules[95, 88]. Oxidative eustress is a concept that refers to a physiological oxidative stress, which is maintained by constant monitoring of the redox regulations[91, 97, 98]. Homeostatic concentration of H_2O_2 is considered of low levels, at <10nM. On the contrary, when concentration of H_2O_2 is supraphysiological (>100nM), adaptative stress responses are activated, thus inciting the oxidative distress (**Figure IV**)[98, 91].

Apart from being a product of NOXs, H_2O_2 can also be produced by other oxidases in the endoplasmic reticulum (ER), peroxisomes and superoxide dismutases (SOD1-3) from $O_2^{\cdot-}$ [90]. Some argue that under certain condition, ROS can freely diffuse through the cellular membranes and subcellular compartments[99], while others show that specific aquaporins (peroxiporins) facilitate H_2O_2 to cross membranes[100, 95]. In opposition to this, $O_2^{\cdot-}$ radical has a shorter lifespan as it is less stable. Despite it is usually spontaneously dismutated or catalysed by SODs, that produce O_2 and H_2O_2, it is highly reactive and can efficiently react with other radicals[85,91,90]. Overall, differential ROS production will have functional significance in terms of molecular signalling or compartment-specific oxidation[90].

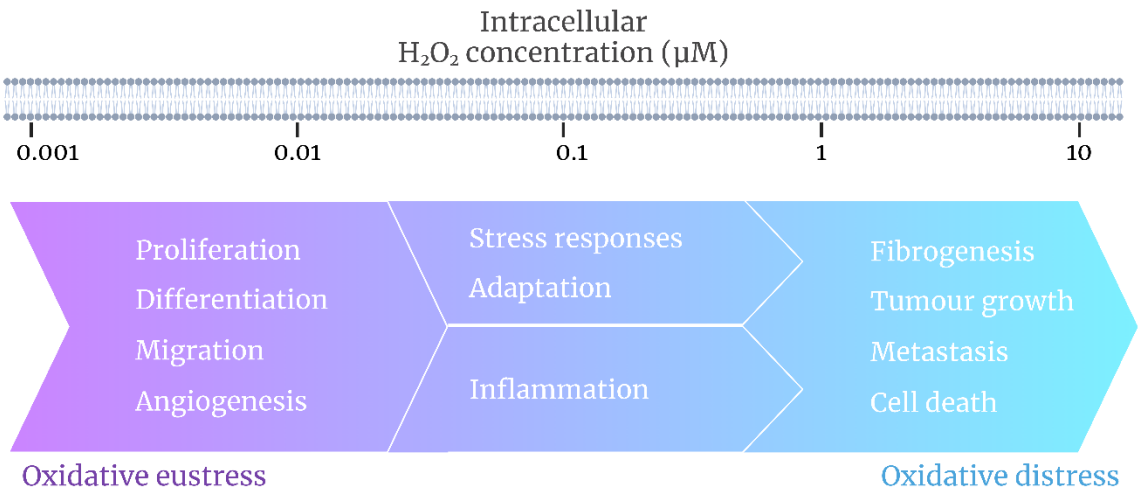

Figure IV. Oxidative eustress and distress: estimated ranges and their correspondent cellular responses. Adapted from: Sies&Jones, 2020.

3.2 Structure and activation

NOXs are transmembrane flavoproteins that transport electrons across cellular membranes to reduce oxygen. Structurally, all NOX family members share a conserved catalytic core that consists of six transmembrane alpha helix, two heme-binding sites coordinated by four histidine residues (in the third and fifth transmembrane domains) and a cytosolic C-terminal dehydrogenase domain that contains binding sites for NADPH and Flavine adenine dinucleotide (FAD)[86,84]. Although these regions are conserved, there are differences in their NH2-terminal structure, subunits, and regulatory proteins (**Figure V**). In the NH2-terminal region, NOX5 and DUOX1-2 feature a calmodulin-like domain with calcium-binding EF-hand motifs. Moreover, DUOX isoforms have an additional NH2-terminal transmembrane segment and an extracellular peroxidase-like domain. It is commonly believed that this peroxidase domain enables DUOX enzymes to produce H_2O_2 directly, as happens with NOX4, too[84,86,87].

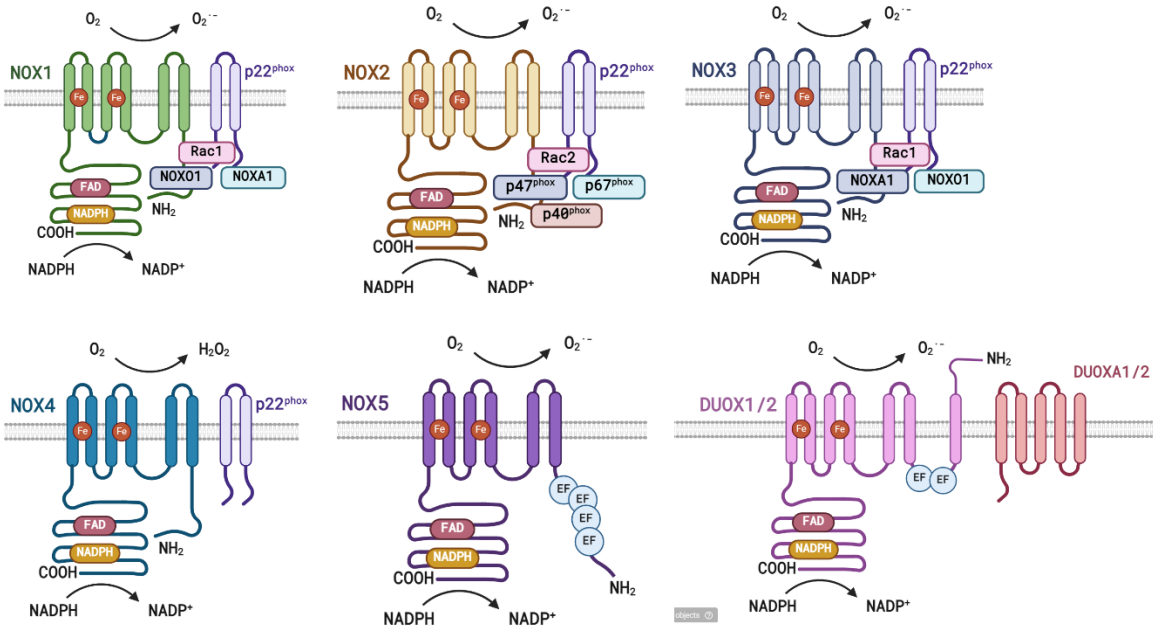

Figure V. Schematic illustration of the NADPH oxidase family members and their associated subunits. Adapted from: Vermot et. al., 2021.

NOX2 has gp91^{phox} as a catalytic core and it requires the heterodimerization with p22phox in the cell membrane., that acts as a maturation factor. Full activation takes place when the four cytosolic regulatory subunits bind: p47^{phox}, p67^{phox}, p40^{phox} and small GTPase Rac2. In short, p22^{phox} stabilizes the catalytic core and once p47^{phox} is phosphorylated, it facilitates the assembly of the other subunits to form the full complex. After the complex forms, Rac initially interacts with NOX2 and then with p67^{phox}. This interaction leads to the creation of an activated complex that produces $O_2^{\cdot-}$ by transferring electrons from cytosolic NADPH to O_2 in the luminal or extracellular region[84, 86, 87, 101]. In a similar way to the previous one, NOX1 and NOX3 activities are also dependent on dimerization with p22^{phox} and to the posterior binding to some regulatory subunits: to NOX organizer 1 (NOXO1), as a p47^{phox} homologue, to NOX activator 1 (NOXA1), as a p67^{phox} homologue, and to Rac1. Like NOX1-3, NOX4 needs p22^{phox} to be stabilized, although it does not need further cytosolic subunits to be activated[84,86,87, 102]. However, NOX5 activity is independent of any subunits. Even so, activation of NOX5 and DUOX enzymes is calcium-dependent, as they contain a calcium

binding EF-hand structure. Moreover, DUOX1 and DUOX2 also need to associate with DUOXA1 and DUOXA2, respectively, to be a fully functional complex.

As can be expected, the regulation of the activity of NOXs and DUOXs can be by their own protein expression, calcium availability and expression of the regulatory subunits. NOX family expression is ubiquitous in mammals, despite each individual member can have different distribution among species and tissues[84,101].

3.3 NADPH oxidase NOX4

The human NOX4 gene is located on chromosome 11q14.2–q21 and consists of 25 exons[103]. Its primary sequence includes 578 amino acids and has a predicted molecular weight of 66.5kDa. Initially identified in the kidney[104,105], NOX4 has since been found in various cell types, including osteoclasts, vascular smooth muscle cells, endothelial cells, fibroblasts, keratinocytes, neurons, and notably in hepatocytes, which are of particular interest in this study.

3.3.1 Particular structure and activation

As some other family members, NOX4 consists of six transmembrane domains, which are connected by five loops, named from A to E, and NADPH and FAD domains in the cytosolic domain (**Figure VI**)[106,107].

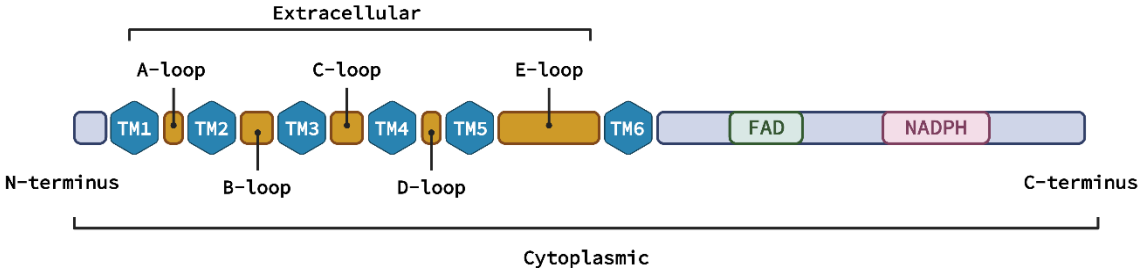

Figure VI. NOX4 protein domain map. TM: transmembrane domain. Image created using BioRender software. Adapted from: Ogboo B.C., *et al*. Redox Biol 2022; Hecker L., *et al*. Nox4: From discovery to Pathophysiology, 2023.

Depending on the localization of the loops, each one has a specific role. For instance, B-loop is the most important one, along with FAD and NADPH domains, that are all located facing the cytoplasm[108], and are considered indispensable for the catalytic activity[109]. Moreover, D-loop enables proper NOX4-p22phox interaction. Additionally, NOX4 extracytosolic E-loop has been suggested to have superoxide dismutase-like activity, which would accelerate the spontaneous dismutation of $O2^{\bullet -}$, forming H2O2 and O2[110]. This is one of the interesting characteristics of NOX4 among the NADPH oxidases family. In fact, when NOX4 was purified, electron flux showed a 10% $O2^{\bullet -}$ and a 90% H2O2 production, demonstrating this specificity[102].

Of note, four splice variants for NOX4 have been described (NOX4 B-E). On one hand, some of the variants act as dominant negative molecules, as NOX4 B and C, which lack an NADPH binding site or all the FAD and NADPH binding sites, respectively. On the other hand, variants D and E are considered soluble variants as they lack the hydrophobic transmembrane domain, and are therefore, free. Among all them, NOX4 D presents all NADPH and FAD binding domains, having a ROS production activity almost like full length NOX4[111].

Another outstanding feature of NOX4 is that NOX4 activation only requires of $p22^{phox}$ dimerization, while the other members need different cofactors to form a complex and be activated (**Figure V**). This phenomenon implies that unlike other isoforms, NOX4 is constitutively active. Therefore, NOX4 activity is mainly regulated through gene transcription[112,113]. However, some studies show post-translational modifications that negatively regulates NOX4 activity, such as, the phosphorylation in Y566 residue by tyrosine kinase FYN[114114]. In addition, it can also be ubiquitinated by heat shock protein 70 (Hsp70)[115] or E3 ubiquitin-protein ligase or others, and thus degraded through the proteasomal system[116].

3.3.2 Subcellular localization

As previously stated, ROS may act as redox signalling mediators in processes such as cell growth, apoptosis, migration, among others[84,94]. As ROS are diffusible molecules that

usually have a short live, the subcellular compartment at which they are produced is key to grant different functionality. Unfortunately, the limited availability of well-characterized and sensitive antibodies for NOX4 has impeded the advancement in assessing the endogenous expression, localization, and tissue distribution. In summary, all these issues have led to controversy and discussion among the scientists in the field about which may be the actual locations of NADPH oxidase (**Figure VII**).

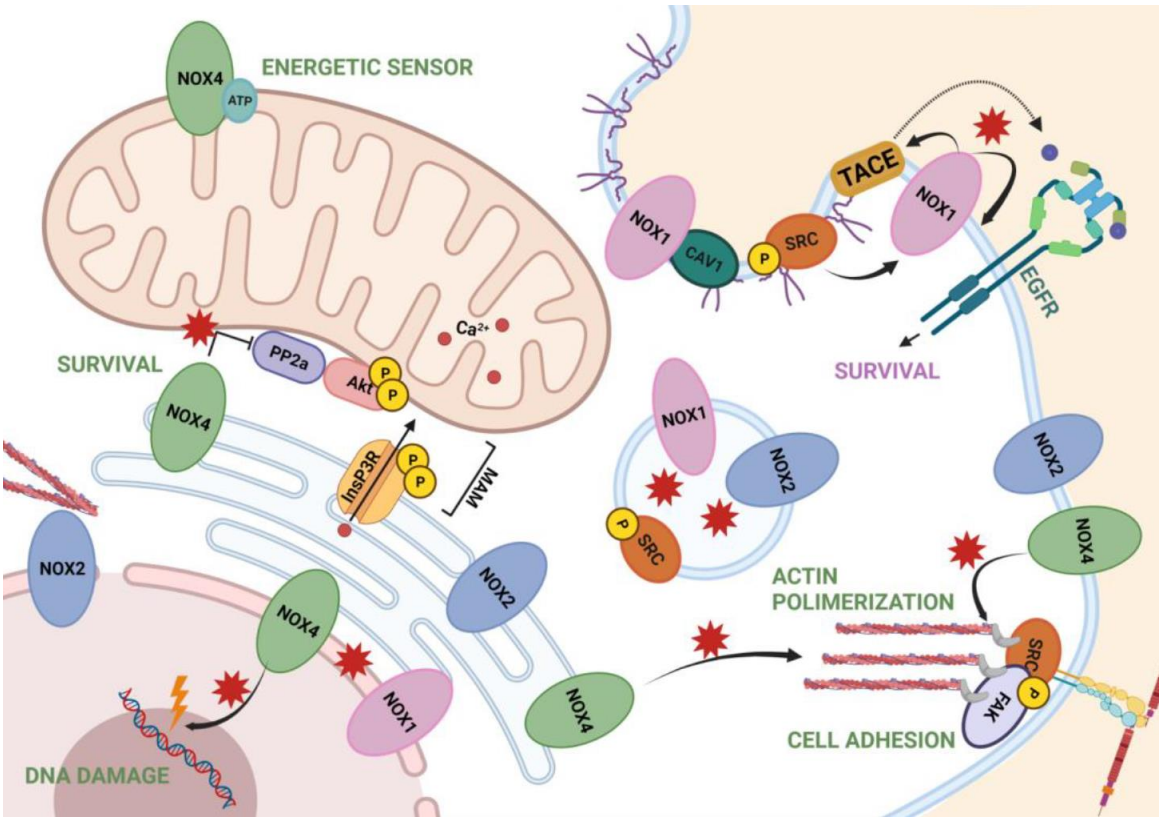

Figure VII. Summary of NOXs localization and NOX-dependent redox signaling through ROS. NOX1 is involved in survival pathways by EGFR and found in endosomes and nuclear membrane. NOX2 is found in the endoplasmic reticulum, endosomes and nuclear membrane, associated with the cytoskeleton. NOX2 is also associated, along with NOX4, to the plasma membrane and near the focal adhesions, regulating cell adhesion. Finally, NOX4 also mediates actin polymerization from the ER, as well as survival signaling when located in MAMs. In the mitochondria, it acts as an energetic sensor, and in the nuclei, is known to produce ROS in the perinuclear and nuclear space. Extracted from: Herranz-Itúrbide M, Cells, 2021.

Nevertheless, NOX4 has been reported in different intracellular compartments. For instance, NOX4 in the mitochondrial membrane has been observed to function as an energetic

sensor or metabolic checkpoint, being regulated by Adenosine triphosphate (ATP) levels[117,118]. Also, NOX4 has been found in the ER, where its ROS would oxidise proteins and act as oxidative signalling in the Unfolded Protein Response (UPR)[119,120,121]. In some cases, NOX4 has been described in the nuclei of some cellular types, such as endothelial cells, fibroblasts and hepatocytes[122,123]. There are other reports of subcellular compartments where NOX4 can be found, but for this project, I want to highlight a specific location: the focal adhesions. NOX4 has been reported to play a role in actin cytoskeleton regulation, as this thesis will further explore. NOX4 is observed along the fibrillar actin fibres and co-localizing with vinculin and $p22^{phox}$, suggesting being active next to the focal adhesions[124,125]. In other cell types, like neutrophiles, NOX4-derived ROS activate SRC kinases in the focal adhesions to promote their cell attachment[126]. And last, F-actin oxidation by NOX4 promotes the maturation of focal adhesion by binding actin and vinculin[127].

4. TGF-β – NOX4 axis role in hepatocarcinogenesis

TGF-β cytokine also plays a role in progression of stages from a noncancerous disease, such as liver fibrosis, to cancer[128]. Chronic liver injuries can increase TGF-β ligands expression, which contribute to the different stages of HCC progression both altering the signalling in malignant cells and the tumour microenvironment (TME). In this section we will revise the role of this TGF-β-NOX4 contribution in each situation.

4.1 Role of the TGF-β – NOX4 in HCC

In previous sections we have already revised the role of TGF-β in some cell functions that usually get dysregulated in HCC, such as cell growth or apoptosis. Moreover, during hepatic carcinogenesis, ROS are overwhelmingly produced creating an oxidative microenvironment that may generate different and various types of cellular stress, which is one of the reasons why NOXs are linked to HCC[129]. Although the specific role of NOX family in hepatocarcinogenesis is yet to be completely unravelled, it is clear that they contribute to liver cancer progression.

As previously explained, NOX4 upregulation by TGF-β is needed for its pro-apoptotic activity in HCC cells[52], thus being one of the reasons why NOX4 had been proposed as a potential tumour suppressor in the liver. Moreover, NOX4 has also been shown to mediate TGF-β-induced senescence in liver tumour cells, contributing again to preventing hepatocarcinogenesis[130]. There are different molecular mechanisms in HCC that impair TGF-β-mediated NOX4 upregulation, which confers an advantage in HCC cells, as they are counteracting its tumour-suppressor action[131,57,59,63].

For all these reasons, in the last years, deepening in the role of NOX4 as a potential tumour suppressor in the liver has become important. Stably knocking down NOX4 expression in HCC cells, *in vitro*, increases the cell proliferative capacity. Besides, when those cells were injected in xenograft experiments in athymic mice, NOX4-silenced cells had an advantage for tumour progression[132]. Our group has recently demonstrated that loss of NOX4 in HCC tumour cells induces metabolic reprogramming in a Nrf2/MYC-dependent manner to promote HCC progression[133]. Additionally, it was seen that low levels of NOX4 with high levels of MYC were concomitant with an increase in the relapse[133]. Interestingly, *NOX4* expression has been proposed as a prognostic factor in patients of HCC after hepatectomy, where low *NOX4* expression reflected shorter relapse-free and overall survival[134]. In the same line of evidence, increased *NOX4* expression has been associated with genes that inhibit tumour progression in HCC patients[135]. However, no such significant trend regarding NOX4 predictive value in survival was seen in univariate analysis in another cohort of HCC patients after partial hepatectomy[136].

Nevertheless, it is very relevant to consider that in most of solid tumours, like head and neck, oesophagus, bladder, ovary, prostate or melanoma, expression of *NOX4* is high when compared to histologically uninvolved specimens from the same organs[137] and NOX4 is being considered as a promising therapeutic target of malignancy[138].

4.2 Role of the TGF-β – NOX4 in Tumour Microenvironment

The concept of TME refers to a wide variety of resident and infiltrating cells, secreted cytokines and growth factors, and ECM proteins. All of these factors provide for help and scaffolding to the tumour, assisting in the infiltration, migration and overall tumoral progression. Interactions among the malignant and stromal cells lead to the accumulation of ECM, inflammation, metastasis, anti-tumorigenic immune response suppression... TGF-β is produced by most cell types in the liver, also during hepatocarcinogenesis, which places this cytokine in a key position for the regulation of these cancer hallmarks. In this section, we will revise the elemental points of the TGF-β – NOX4 axis that control Cancer Associated Fibroblasts (CAF) and the immune system.

During these last years, studies have been focused mainly on the role of NOX4, independently of TGF-β, in the biology and progression of liver tumours. However, TGF-β is the main inducer of NOX4 in the context of liver inflammation and fibrosis[1391] and, therefore, it is utterly important to further study this axis.

4.2.1 TGF-β – NOX4 in Hepatic Stellate Cells

HCC typically arises from a background of chronic liver disease, which often progresses through stages of fibrosis and eventually cirrhosis. These premalignant conditions create a proper environment to the malignant transformation of hepatocytes[140]. A key feature of liver fibrosis is the activation of HSCs into myofibroblasts (MFBs). This activation alters the microenvironment by generating ECM deposits and releasing pro-fibrotic and pro-inflammatory factors, thereby promoting the progression of chronic liver disease[140]. Most studies agree that HSCs are the primary source of MFBs in experimental models of liver fibrosis[141].

Physiological levels of ROS stimulate HSC activation, proliferation and production of Collagen I[142], towards an MFB[143]. In the liver, TGF-β-induced NOX4 is known to regulate oxidative stress. When looking into the levels of NOX4 and TGF-β ligands, they seem to be

increased in fibrotic patients, either of viral or NASH ethiology[144]. NOX4 is needed for TGF-β-induced activation of HSCs to a MFBs as it was shown that NOX4 downregulation significantly attenuated it[144]. NOX4 is not the only NOXs family member implicated, but NOX1 has also been seen to induce proliferation and activation of HSCs, thus playing a role in liver fibrosis (**Figure VIII**)[145,146]. Indeed, studies showed that NOX1/NOX4-defficient mice had less liver inflammation and fibrosis, and that, on the contrary, cirrhotic patients had increased NOX1 and NOX4 levels[147]. Furthermore, activation of HSC by TGF-β is mediated by activation of canonical (SMAD3)[21,148] and non-canonical (ERK, JNK, p38 and STAT3)[149,150] signalling pathways. These induce the expression of pro-fibrotic genes, such as *COL1A1* (Collagen1) or *CCN2* (Connective tissue growth factor (CTGF)), which can also stimulate the production of ECM components[143].

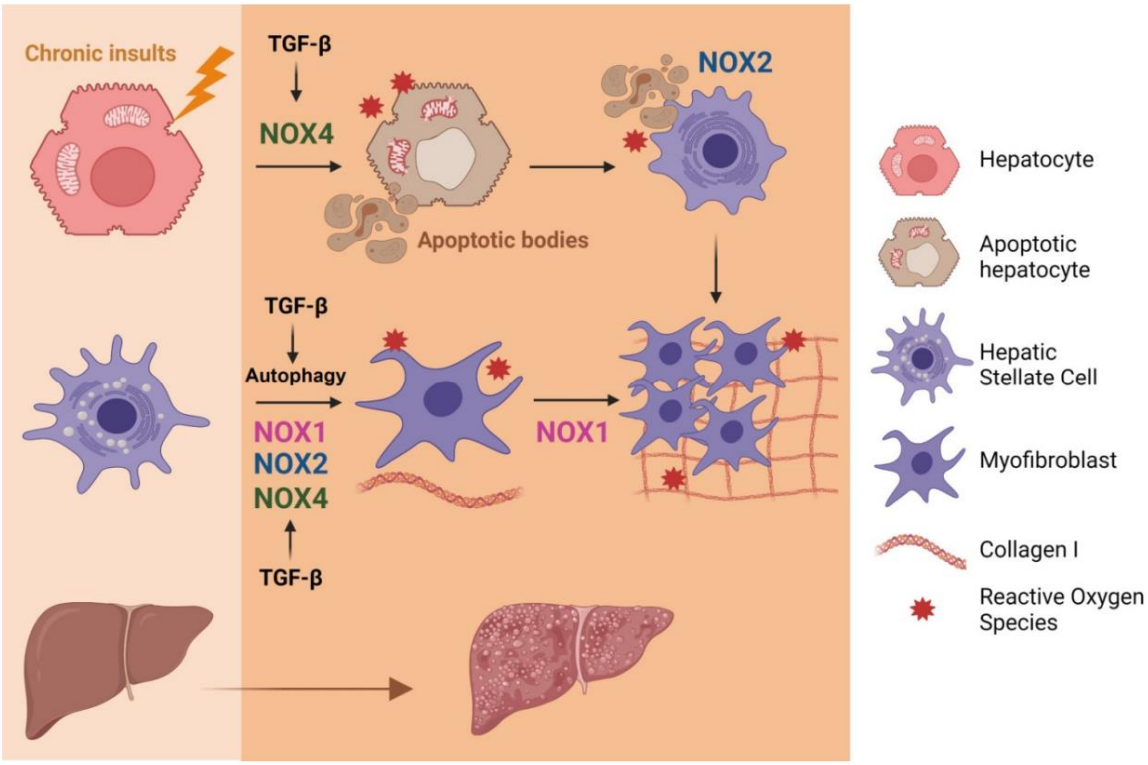

Figure VIII. TGF-β-NOX4 axis in liver fibrosis. Implication of different NOXs and TGF-β effect on HSC towards MFB. Besides, TGF-β-induced NOX4 mediates hepatocyte apoptosis, which contributes to the transdifferentiation, too. Adapted from: Herranz-Itúrbide M, Cells, 2021.

Cell death in hepatocytes is an indirect, but relevant, event that also participates in fibrogenesis, as apoptotic bodies that come from chronically damaged hepatocytes have the

capacity of inducing transdifferentiation of HSCs to MFBs[151]. Therefore, apoptosis and phagocytosis of hepatocytes directly induce HSC activation and initiation of fibrosis. As explained in *section 2.1.1*, TGF-β promotes apoptosis through NOX4 upregulation in hepatocytes[52]. Furthermore, dying hepatocytes secrete damage-associated molecular patterns (DAMPs) that can bind to pattern recognition receptors in the innate immune cells to activate inflammatory responses[152]. Being NOX2 the phagocytic NOX, it has been demonstrated to be required for phagocytosis of said apoptotic bodies by HSCs[153].

Cancer Associated Fibroblasts

CAFs are key components of the TME and, in the liver, are described to come from several cell types: HSCs, which account for most of them, portal fibroblasts, mesenchymal stromal cells, among others[154,155,156]. The activation of CAFs support tumour progression as they produce cytokines and ECM, which can promote immune evasion and angiogenesis[157]. In fact, in public databases, analysis point to a worse overall survival in HCC patients when CAF population is high, compared to that of patients with low CAF content[158]. That is because this cell type contributes to tumour progression in several ways: vascularization promotion[159], ECM stiffness and remodelling[160] and cancer cell stemness[161], by secreting paracrine factors such as HGF[162]. Additionally, CAFs have been linked to the creation of an immunosuppressive microenvironment in HCC, by secretion of macrophage migration inhibitory factor (MIF)[163].

TGF-β on CAFs is known to induce a pro-fibrotic phenotype, through activation of SMAD3 that promotes *ACTA2* expression[164]. This activated situation leads to a higher secretion of TGF-β per se, but also of several chemokines, contributing altogether to a crosstalk between tumour and stromal cells. Some studies show that HCC cells can respond to CAF-secreted TGF-β, or other cytokines, by undergoing EMT[165], migrating and invading[166]. Moreover, CAF-derived cardiotrophin-like cytokine factor 1 (CLCF1) increases the secretion of TGF-β and C-X-C Motif Chemokine Ligand (CXCL)6 by HCC cells[167].

Despite the advances, studies of the specific action of TGF-β on CAFs in the liver are lacking, as opposed to in other organs[168].

4.2.2 TGF-β – NOX4 in immune system

Immune landscapes in tumours are highly heterogeneous. In the case of HCC, approximately 25% of the patients have a high degree of immune infiltration, which are called Immune class. This correlates with a high expression of PD-1/PD-L1, being suited for a PD-1 blocking immunotherapy[169,170]. Importantly, intratumoral CD3+ and CD8+ cells correlate with recurrence and relapse free survival[171]. Moreover, the HCC immune class is further subdivided into active immune response subtype, that accounts for a 65% of the immune class samples and is characterized by overexpression of adaptive immune response genes. The other 35% is the immune exhaustion subtype, characterized by the presence of immunosuppressive markers, such as TGF-β and M2 macrophages[8]. A strong association between the TGF-β signature and the exhausted immune signature in HCC was identified, suggesting that the TGF-β pathway is an important immune regulator and biomarker for HCC[169,170].

A balanced immunity is elemental for homeostasis and health, where cytokines play crucial roles in balancing tolerance and immunity following the productive immune response. TGF-β has been found to be a key cytokine that controls both tolerance and immune responses, either adaptative or innate, in the liver. This equilibrium can be altered by TGF-β released within the TME, which may promote cancer progression through differential effects on multiple key cell types. On one hand, TGF-β's action on adaptative immunity relies on the direct promotion of the expansion of regulatory T cells (Treg) and the inhibition of dendritic and effector T cells. On the other hand, it controls the innate immune system by inhibiting NK cells and regulating macrophages and neutrophils.

TGF-β regulates T-cell-mediated tolerance and immunity through both Treg and Th17 cells in a context-dependent manner[172]. TGF-β has been seen to be indispensable for the suppressive function of Treg cell-mediated suppression, particularly in inflammatory conditions[173]. Indeed, TGF-β Smad-dependent signalling promotes Forkhead box 3 (*FoxP3*) expression, which is a marker of exhausted Treg[174]. Moreover, deletion of TGFβRI in Treg cells results in decreased control of Th17 cells and reduced Treg cell accumulation in the intestines,

which indicates a context-dependent regulation for TGF-β in Treg cell recruitment and retention in specific tissues[175,172]. Regarding the development of Th17, it has been found that TGF-β promotes it by inhibiting SOCS3 but activating Smad2[176]. Additionally, it is known that Th17 cells induced by TGF-β can have both regulatory and pathogenic functions. The presence of TGF-β with other cytokines, such as IL-6, is essential for the proinflammatory functions of Th17 cells[177,178]. This highlights the complex regulatory networks governing Th17 differentiation and function and the dual role that TGF-β has in the immune response. Also, TGF-β can directly inhibit the cytotoxic functions of CD8+ cytotoxic T cell[179]. In these cells, TGF-β cooperates with the transcription factor ATF1 to suppress the expression of IFN-γ to inhibit its antitumor activity, too[180].

Liver macrophages are found in the lumen of liver sinusoids. They can be formed by tissue-resident KC, which under physiological conditions comprise the major proportion, and by monocyte-derived macrophages [181,182], which come from circulating monocytes when they are recruited via inflammatory signals such as CCL2[183,184]. Under NAFLD, NASH or cirrhosis, the number of recruited monocytes increases, while the resident KCs are depleted[185]. CD68+ macrophages have been characterized in HCC tumours, as a general marker for macrophages. Indeed, increased CD68 expression in adjacent tissues from patients, conferred an increased overall survival (OS)[186].

Macrophages have distinct phenotypes depending on their functionality towards an inflammatory situation. On one hand, they can behave as a pro-inflammatory or anti-tumoral macrophage, named the M1-like macrophage. They usually have iNOS expression and secrete IL-6, IL-12, CCL2 or IFNγ[187,188]. On the other hand, they can be a M2-like macrophage, characterized by expression of CD163, MRC1 or PDL-1 on the cell membrane, and secretion of IL-10 and TGF-β. Overall, they contribute to create a more pro-tumoral and anti-inflammatory environment[189,190]. However, macrophage markers are often ambiguous as they are shared among several of the different phenotypes[191,192].

TGF-β signalling is also a critical mediator in tumour invasion and metastasis through the action of tumour associated macrophages (TAM) that secrete growth factors, including TGF-β, which promote migration of endothelial cells and angiogenesis[193,194]. All these data point to TGF-β as one of the master immunosuppressive molecules in HCC and imply that targeting the TGF-β pathway might enhance antitumor immunity in HCC patients. It is worthy to mention that in a TCGA cohort of HCC, TAMs presence has been associated with poor prognosis[195].

Nevertheless, NOXs study in the immune landscape has also demonstrated that they may play a relevant role. Recent evidence indicates that NOX1 expression in macrophages mediates tumour promoting activity, through activating a ROS/MEK mechanism responsible of inflammatory cytokines production, thereby promoting the survival and proliferation of oncogene-carrying mutant hepatocytes, which ultimately accelerate HCC development[196]. In fact, when NOX1 was inhibited by GKT771 during HCC progression, the expression of inflammatory markers was reduced, which lead to an attenuated pro-tumorigenic environment[197].

NOX2-derived ROS are also involved in TLR2-dependent M2 macrophage polarization by triggering autophagy, supporting tumour growth[198]. Indeed, in KC, the resident macrophages in the liver, the generated O2·– by NOX2 activation during liver inflammation induces hepatocyte DNA damage, ultimately contributing to tumour initiation and promotion, an effect that was attenuated in p47phox-deficient mice[199]. This mice model also showed that NOX2-derived O2·- from KC, contributes to the progression of hepatocarcinogenesis rather than to its initiation.

NOX4 has been more studied in the recent years due to an increase found implication in macrophages and immune system. For instance, NOX4 has been found to be elevated in lung macrophages of patients. NOX4, in this case, is crucial for lung macrophage profibrotic polarization and fibrotic repair[200]. Also, NOX4 regulates apoptosis resistance in lung macrophages, which induces fibrotic progression[201]. Besides, NOX4 in HCC has been linked

to an increased recruitment and polarization of M2 TAMs via ROS/PI3K signalling production of several cytokines[202].

In summary, HCC represents a significant global health challenge, marked by its complex interplay with the immune system, particularly macrophages. TAMs are crucial in shaping the tumour microenvironment, often promoting immunosuppression and aiding tumour progression. They achieve this through various mechanisms, including the expression of immune checkpoints and recruitment of regulatory T cells, while diminishing the activity of cytotoxic T cells and NK cells. The dynamic and multifaceted roles of TAMs underscore the need for targeted therapeutic strategies that can modulate the immune response to effectively combat HCC. Understanding and manipulating these immune interactions hold promise for improving outcomes in HCC treatment and achieving better clinical success with immunotherapies.

HYPOTHESIS

Considering that TGF-β is the main regulator of NOX4 in hepatocytes and that its levels are low in an important percentage of HCC patients, we hypothesized that NOX4 could be relevant for the response to TGF-β as a tumour suppressor factor.

In addition, we hypothesized that the expression of NOX4, either in the tumour or in the stroma cell, could influence tumour progression, exerting actions on the tumour cell but also on the tumour microenvironment.

OBJECTIVES

Objective 1. Characterization of the role of NOX4 in HCC tumour cells.

1.1 Generation of loss (CRISPR-Cas9 technology) of NOX4 function in human HCC cells.

1.2 Response to TGF-β in terms of cell proliferation and apoptosis in the new generated HCC cell lines. Molecular mechanisms involved.

1.3 Collection of the HCC samples. Analysis of the translational relevance of the findings in biopsies from HCC patients in tumoral and non-tumoral areas. Gene expression analysis.

1.4 Is the TGF-β-NOX4 axis regulating TGF-β-induced pro-tumorigenic actions?

Objective 2. Role of NOX4 on liver tumorigenic progression in experimental animal models of HCC

2.1 Generation of DEN-induced hepatocarcinogenesis mice model. Design of new models of HCC induction in mice.

2.2 Macroscopic and microscopic analysis of the tumoral lesions: histologic analysis, immunohistochemistry. Detailed analysis of the effects on tumour and stromal cells. Gene and protein expression analysis.

Objective 3. Impact of NOX4 in the interactome between HCC cells and immune system cells.

3.1 Set up of 3D spheroid model with HCC cells, for monoculture and multicellular culture.

3.2 NOX4 role in the interactome between tumour and immune cells. Effect of Conditioned Media from HCC cells on recruitment and phenotype of immune cells.

MATERIAL AND METHODS

1. Human samples

Human samples were collected with the required informed consent in written from each patient and the approval of the Institutional Review Board (Comité Ético de Investigación Clínica (CEIC), Bellvitge University Hospital (HUB)). Patients' written consent form and the study protocol conformed to the ethical guidelines of the 1975 Declaration of Helsinki.

Tissues from non-tumour (NT) and tumour (T) areas were collected from patients during surgical procedures. Samples derived from a cohort of 124 patients with different aetiology came from liver explants at transplantation or resection and incorporated in the study, with most of them in histological grade 2–3. At **Table I**, different details about the clinic-pathological parameters can be seen.

Table I. Clinico-pathological characteristics of HCC patients used in this study.

Patient ID	Liver pathology	Etiology	Tumor size (cm)	Histological grade	Status	Follow-up (months)	Relapse Yes/No
1	Cirrhosis	Alcohol	2	2	Dead		No
2	Cirrhosis	Unknown	4.5	3	Dead	45	Yes
3	No Fibrosis	Unknown	6	2	Dead	45	No
4	No Fibrosis	Unknown	7	2	Dead	43	No
5	No Fibrosis	Unknown	20	2	Dead	12	Yes
6	Cirrhosis	VHC	4.5	4	Alive	98	No
7	No Fibrosis	Alcohol	2	2	Alive	86	No
8	Cirrhosis	VHC	5	3	Alive	81	Yes
9	Cirrhosis	VHC	2.1	3	Dead	42	Yes
10	No Fibrosis	VHB	5.5	3	Alive	77	Yes
11	Cirrhosis	VHC	2	3	Alive	74	No
12	Cirrhosis	VHC	3.2		Alive	72	No
13	No Fibrosis	VHC	9.5	2	Alive	71	No
14	Cirrhosis	VHB	4.9	2	Alive	71	No
15	Cirrhosis	Alcohol	2.5	2	Dead	57	Yes

16	No Fibrosis	VHC	2.9	2	Alive	70	No
17	Cirrhosis	VHC	1.2	2	Alive	65	Yes
18	Cirrhosis	Alcohol	26	2	Alive	61	Yes
19	No Fibrosis	Unknown	8	3	Alive	61	No
20	Cirrhosis	VHC	4.5	2	Alive	61	No
21	Cirrhosis	Alcohol	3.8	3	Alive	60	No
22	Mild Fibrosis	Unknown	4	2	Alive	59	No
23	Mild Fibrosis	VHC	1.2	3	Alive	59	No
24	Cirrhosis	VHC	1.8	1	Alive	59	No
25	Mild Fibrosis	Unknown	4.5	3	Alive	49	No
26	Cirrhosis	VHC	5.8	3	Alive	48	Yes
27	Cirrhosis	VHC	5.5	2	Alive	22	No
28	Cirrhosis	NASH	2.5	2	Alive	38	Yes
29	Cirrhosis	Alcohol	3	3	Dead	43	Yes
30	Cirrhosis	VHC	2.5	3	Alive	125	Yes
31	Mild Fibrosis	Alcohol	3	3	Alive	121	Yes
32	No Fibrosis	Unknown	27	3	Dead	13	Yes
33	Mild Fibrosis	Unknown	7.5	3	Dead	28	Yes
34	Cirrhosis	VHC	3	3	Dead	89	No
35	Cirrhosis	Unknown	6	2	Dead	109	No
36	Cirrhosis	VHC	2.5	2	Alive	111	No
37	Mild Fibrosis	VHC	3.8	2	Dead	81	No
38	Cirrhosis	VHC	3.3	3	Alive	51	Yes
39	Cirrhosis	VHC	4.5	3	Dead	66	Yes
40	No Fibrosis	Unknown	3	2	Alive	106	Yes
41	Mild Fibrosis	VHB	2.9	2	Alive	105	No
42	Cirrhosis	VHC	2.8	2	Alive	105	No
43	Mild Fibrosis	VHC	3.5	3	Alive	94	No
44	Cirrhosis	VHC	3.5	3	Dead	35	No
45	Cirrhosis	VHC	5	2	Alive	94	Yes
46	No Fibrosis	Unknown	6.5	2	Alive	92	No
47	No Fibrosis	Unknown	20	1	Alive	87	No

48	Cirrhosis	VHC	2.5	2	Dead	47	Yes
49	No Fibrosis	VHB	9	3	Dead	13	Yes
50	Mild Fibrosis	NASH	4.2	3	Dead	30	Yes
51	No Fibrosis	Unknown	8.3	3	Dead	8	Yes
52	Cirrhosis	Alcohol	2.6	2	Alive	77	No
53	Cirrhosis	Alcohol	2.3	2	Dead	60	No
54	Cirrhosis	VHC	2.3	2	Alive	29	Yes
55	Mild Fibrosis	Alcohol	1.9	2	Alive	67	No
56	No Fibrosis	VHC	4.7	2	Alive	64	No
57	Cirrhosis	VHC	2.5	4	Alive	64	Yes
58	Cirrhosis	VHC	3	2	Alive	64	Yes
59	Cirrhosis	Unknown	2.8	2	Alive	62	No
60	Cirrhosis	VHC	2.5	2	Dead	13	Yes
61	Cirrhosis	VHB	4.9	4	Dead	6	Yes
62	Cirrhosis	VHC	8.5	3	Dead	15	Yes
63	No Fibrosis	VHC	2.5	4	Alive	75	No
64	Cirrhosis	VHC	5.5	3	Alive	75	Yes
65	Cirrhosis	Alcohol	1.4	2	Alive	73	No
66	No Fibrosis	Alcohol	7	2	Alive	53	Yes
67	Cirrhosis	Alcohol	16	2	Alive	22	Yes
68	No Fibrosis	Unknown	3.5	1	Alive	45	No
69	Cirrhosis	VHC	1.5	3	Alive	44	No
70	Mild Fibrosis	VHC	9	3	Alive	41	No
71	No Fibrosis	Unknown	4.8	3	Dead	16	Yes
72	Cirrhosis	VHC	2.8	4	Dead	23	Yes
73	Cirrhosis	VHC	3.7	2	Alive		No
74	Cirrhosis	VHB	3.3	2	Dead	12	Yes
75	Cirrhosis	Alcohol	2.6	1	Alive	25	No
76	No Fibrosis	Unknown					
77	No Fibrosis	Unknown	12	2	Alive	35	No
78	Cirrhosis	Alcohol	2.8	2	Alive	20	Yes
79	No Fibrosis	Unknown	11	2	Alive	20	Yes

80	Cirrhosis	Unknown	4.5	2	Alive	18	No
81	No Fibrosis	Unknown	3.5	2	Alive	18	No
82	Mild Fibrosis	Unknown	7.5	3	Alive	17	Yes
83	Cirrhosis	Alcohol	4	2	Alive	16	No
84	No Fibrosis	Unknown	8.6	2	Alive	16	No
85	Cirrhosis	Alcohol	2	2	Alive	15	No
86	Mild Fibrosis	Alcohol	3	3	Alive	15	Yes
87	Cirrhosis	Alcohol	3.7	3	Alive	15	Yes
88	No Fibrosis	Unknown	5.5	2	Alive	13	No
89	Cirrhosis	VHC	2.5	2	Alive	9	No
90	Cirrhosis	Alcohol	1	2	Alive	80	Yes
91	No Fibrosis	VHC	3.5	2	Alive		Yes
92	Cirrhosis	VHC	2.5	1	Alive	45	No
93	Cirrhosis	VHC	3.8	2	Alive	44	No
94	Cirrhosis	VHC	2.2	2	Alive	42	No
95	Cirrhosis	VHC	1.2	2	Alive	38	No
96	Cirrhosis	Alcohol	1.7	2	Alive	37	No
97	Cirrhosis	VHB	3	3	Dead	7	Yes
98	Mild Fibrosis	VHC	5.2	3	Alive	35	Yes
99	Mild Fibrosis	Alcohol	6	4	Alive	35	No
100	Cirrhosis	VHB	3	4	Alive	29	Yes
101	Cirrhosis	VHC	1.8	2	Alive	27	Yes
102	Cirrhosis	VHC	3.5	3	Alive	24	Yes
103	Cirrhosis	Alcohol	2	2	Alive	21	No
104	No Fibrosis	Unknown	6.5	2	Alive	21	No
105	Cirrhosis	Alcohol	4.5	3	Alive	21	No
106	No Fibrosis	Unknown	6.7	2	Alive	20	No
107	Cirrhosis	VHB	4.7	3	Alive	19	Yes
108	Mild Fibrosis	Unknown	8	2	Alive	17	No
109	Mild Fibrosis	Unknown	9	2	Alive	17	Yes
110	Cirrhosis	VHC	1.5	2	Alive	15	No
111	No Fibrosis	Unknown	7.5	1	Alive	14	No

112	No Fibrosis	Unknown	5	1	Alive	13	No
113	Cirrhosis	NASH	2.5	2	Alive	13	No
114	No Fibrosis	Unknown	4.5	2	Alive	10	No
115	Cirrhosis	VHC	2.8	2	Alive	12	No
116	No Fibrosis	Unknown	9	2	Alive	9	No
117	No Fibrosis	VHB	3.8	2	Alive	9	No
118	Cirrhosis	VHC	1.3	2	Alive	10	No
119	No Fibrosis	Unknown	4	2	Alive	10	No
120	Cirrhosis	VHC	4.3	2	Alive	8	Yes
121	Cirrhosis	VHC	4	2	Alive	8	No

HBV: Hepatitis B virus; **HCV**: Hepatitis C virus; **NASH**: Non-Alcoholic Steatohepatitis

2. Animal models

All experiments complied with the EU Directive 2010/63/UE for animal experiments and the institution's guidelines (Ethical Committee for animal experimentation of IDIBELL) and were approved by the General Direction of Environment and Biodiversity, Government of Catalonia (experiments in NOX4-/- mice, #4589).

NOX4 -/- mice (B6.129-Nox4tm1Kkr/J) were generated by Dr. Krause's laboratory[203] and obtained from Jackson Laboratories, together with the corresponding C57BL/6J wild type (WT) mice. NOX4-/- mice were generated by replacement of exon 4 of *Nox4* gene with a neomycin cassette (**Figure IX**). The mice were housed at the animal facility of IDIBELL (L'Hospitalet de Llobregat, Spain). Male mice, hosted under 12h light/dark cycle with free access to food and water were used in the study.

In this thesis, WT and NOX4 -/- mice have been used to study NOX4 role in two different hepatocarcinogenic model, which will be next explained. Validation of the experimental model had been previously done in the laboratory.

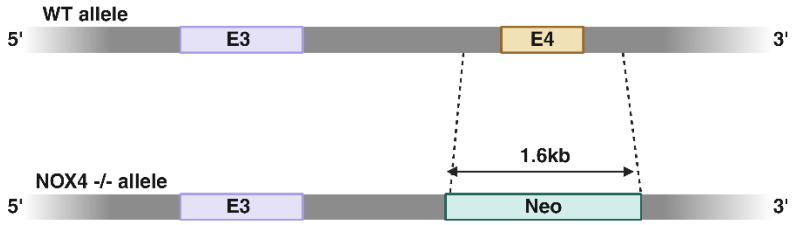

Figure IX. Diagram of the alleles. Vector is designed to replace the HindIII fragment containing exon 4 (E4 = 85pb) of the NOX4 gene in the WT (C57BL/6J) (**top**) with a pGK-neo cassette (Neo). The predicted mutant allele generated by homologous recombination is shown (**bottom**).

2.1 DEN-induced hepatocarcinogenesis mice model

To further study the role of NOX4 in the development of HCC, an experiment of hepatocarcinogenesis was performed in the WT and knock-out (KO) NOX4-/- mice. As previously done in the group, 14 days old male mice received intraperitoneal injections of diethylnitrosamine (DEN; 10mg/kg) diluted in saline buffer[204]. Interventions were done during the light cycle. At 11-months post-treatment, mice were sacrificed, and their livers collected.

Parts of each liver lobe were fixed in 4% paraformaldehyde (PFA) overnight and paraffin-embedded for immunohistochemical staining. Total RNA was isolated from frozen tissues for Real Time Quantitative Polymerase Chain Reaction (RT-qPCR) and RNA sequencing (*see section 10*). At least three animals per condition and three different tissue pieces were processed for RNA extraction (**Figure XA**). DEN-induced hepatocarcinogenesis experiments were performed by Macarena Herranz Itúrbide in IDIBELL (L'Hospitalet de Llobregat, Spain) prior to the beginning of the thesis.

2.2 Syngenic HCC mice model

As in our DEN-induced model in WT and NOX4 -/- mice none of the cells from KO mice have *NOX4* expression, we could not elucidate if the effects seen were coming from NOX4 expression from tumoral cells or from stromal cells. Therefore, we decided to perform a

syngeneic orthotopic model experiment, where mouse cells, which had Nox4, were directly injected in the liver of WT and NOX4 -/- mice.

The used mouse line was AL1099, which was isolated from liver tumours induced by hydrodynamic tail vein injection delivery of a transposon-based vector as described[205]. The hydrodynamic tail vein injection consists of injecting a plasmid mix with: 12μg of *pT3-EF1a-MYC-IRESluciferase-OS (MYC-lucOS*), 10 μg of *pT3-N90-CTNNB1 (CTNNB1*) and a 4:1 ratio of transposon to *SB13* transposase-encoding plasmid dissolved in 2 ml of 0.9% NaCl solution. 10% of the weight of each mouse in volume is injected into the lateral tail vein with a total volume corresponding to 10% of body weight in 5–7 seconds. All this work was performed by Dr. Amaia Lujambio's group in Icahn School of Medicine at Mount Sinai (New York, USA)[205].

For the syngeneic model experiment, $2{,}5\times10^5$ cells from AL1099 mouse cell lines were orthotopically injected directly into the left lobe of the liver of 8-week-old C57BL/6 male and female mice. 80% of success rates of tumour formation was achieved. Tumour progression was monitored once a week by bioluminescence using an IVIS Lumina (Perkin Elmer, Shelton, Connecticut, USA) after injecting intraperitoneally 150 mg/kg D-luciferin in Phosphate-buffered saline (PBS) injection during 3 weeks by IVIS imagining. Mice were sacrificed after 15-30 days, depending on the tumour area.

Parts of each liver lobe were fixed in 4% PFA overnight and paraffin-embedded for immunohistochemical staining. Total RNA was isolated from frozen tissues for RT-qPCR. At least seven animals per condition and three different tissue pieces were processed for RNA extraction (**Figure XA**). Syngeneic experiments were performed by Ana Cantos Cortés, Josep Amengual and myself in IDIBELL (L'Hospitalet de Llobregat, Spain).

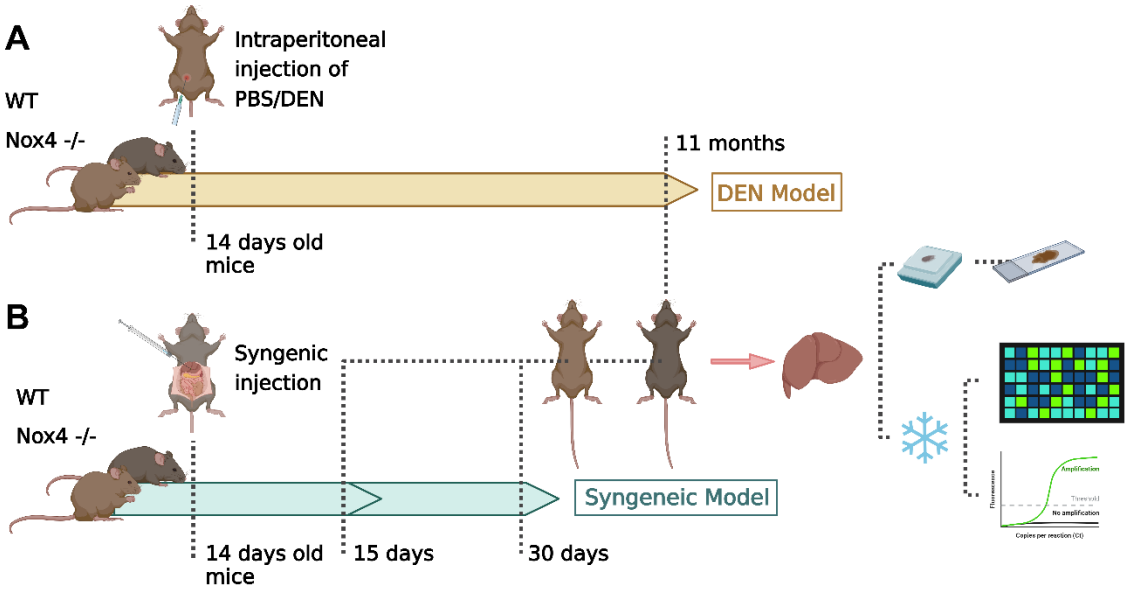

Figure X. Diagram of the alleles. Vector is designed to replace the HindIII fragment containing exon 4 (E4 = 85pb) of the NOX4 gene in the WT (C57BL/6J) (**top**) with a pGK-neo cassette (Neo). The predicted mutant allele generated by homologous recombination is shown (**bottom**).

For ethical reasons, number of animals used in the study was minimized. For the DEN-induced hepatocarcinogenesis, between 3-5 mice were used per condition. For the syngeneic model, between 7-9 mice were used (**Table II**).

Table II. Number of WT and NOX4 -/- mice used in each hepatocarcinogenesis experiment.

	Condition	WT	NOX4 -/-
DEN-induced hepatocarcinogenesis	PBS	5	4
	DEN	3	5
Syngeneic hepatocarcinogenesis		7	7

3. Cell culture

In this thesis, several cell lines have been used. On one side, commercial HCC cell lines have been used throughout all the years; and on the other side, THP-1 monocytic cell line has been used to further study the immune system.

3.1 Cellular models and culture conditions in 2D

PLC/PRF/5 and Hep3B human HCC cells were obtained from the European Collection of Cell Cultures. In 2023, the authenticity of the cell lines was corroborated successfully. PLC/PRF/5 cells were maintained in DMEM, Hep3B in MEM and THP-1 in RPMI, supplemented with non-essential amino acids (Lonza, Basel, Switzerland), 10% foetal bovine serum (FBS) (Sera Laboratories International Ltd, West Sussex, UK), Penicillin (100U/mL), Streptomycin (100µg/mL), Amphotericin (2.5µg/mL), and L-glutamine (2 mM). All of them were maintained in a humidified atmosphere of 37 ◦C, 5% CO2. Cell lines were never used in the laboratory for longer than 4 months after receipt or resuscitation.

3.2 Culture in 3D: spheroids

Traditional two-dimensional (2D) cell culture systems, where cells grow as a monolayer, are widely used among all the scientific community due to the easiness of maintenance and handling of them. Even though they have some obvious conveniences, they often display some limitations in displaying translational results. On the contrary, three-dimensional (3D) cell cultures are becoming every day more implemented in the research routine. That is because this method has shown a promising comparison with a physiological distribution and interaction.

There are several formation methods described, mainly stratified by the scaffolding technique chosen, which depends on the cell needs. The technique used in this project for the creation of the spheroids is the hanging drop, which allows cells to aggregate and form a spheroid in each droplet.

As summarized in **Figure XI**, first, 2D HCC cell cultures were cultured in basal conditions, trypsinized and counted. A low viscosity solution containing 800µl of complete medium and 200µl of methylcellulose was prepared per each condition. $5x10^4$cells/ml were incorporated in the mix and, when necessary, TGF-β treatment was also added in the usual concentration (**Table III**). After pipetting, drops of 25µl were put in the lid of a culture dish,

until all the mixture was finished. Carefully, the lids were placed on top of the culture plate, which contained 5-6ml of media to maintain a proper humidity in the environment. Plates were maintained in the incubator at 37ºC – 10% CO_2 for 72h to develop the spheroids. After this time, drops are slowly pulled down and transferred to a low attachment multiwell to maintain in culture. Depending on the experiment to perform, spheroids have been maintained in culture for 24h to 48h.

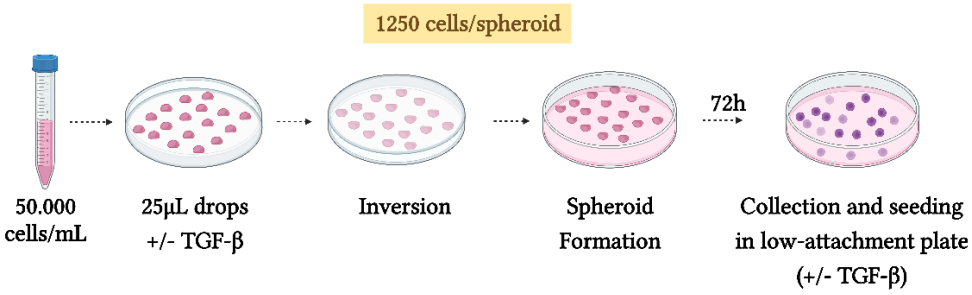

Figure XI. Schematic diagram of hanging drop method. Cells are collected and counted. A mix of 50.000 cells/mL is prepared in a dense media with methylcellulose. Then, 25µL-drops are placed on the lid of the dish, until all the mixture is finished. Next, the lid is inverted and placed on top of the dish, that contains a bit of media to keep the adequate humidity. Finally, after 72h, the spheroids are collected and cultured in a low-attachment plate.

3.3 Treatments used

HCC cells were treated with several compounds in this study. All of the stock solutions prepared according to the manufacturer's protocol. **Table III** illustrates the compound with their respective conditions.

Table III. Chemical compounds added to cell culture and culture conditions used in this study

Compound	Working concentration	Time of treatment	Reference
DPI	10µM	30 min	#D2926, Sigma
TGF-B	2ng/mL	3h-48h	#T7039, Sigma
Q-VD-OPH	20µM	1h	#OPH001, R&D
PI	5µL/100µL	15 min	#ab14085, Abcam
ANNEXIN V-FITC	6µL/100µL	15 min	#ab14085, Abcam

DPI: diphenyleneiodonium; **PI**: Propidium Iodide

3.4 Stable silencing

In this thesis, two different methods have been used to stable silence NOX4 expression in PLC/PRF/5 and Hep3B cells.

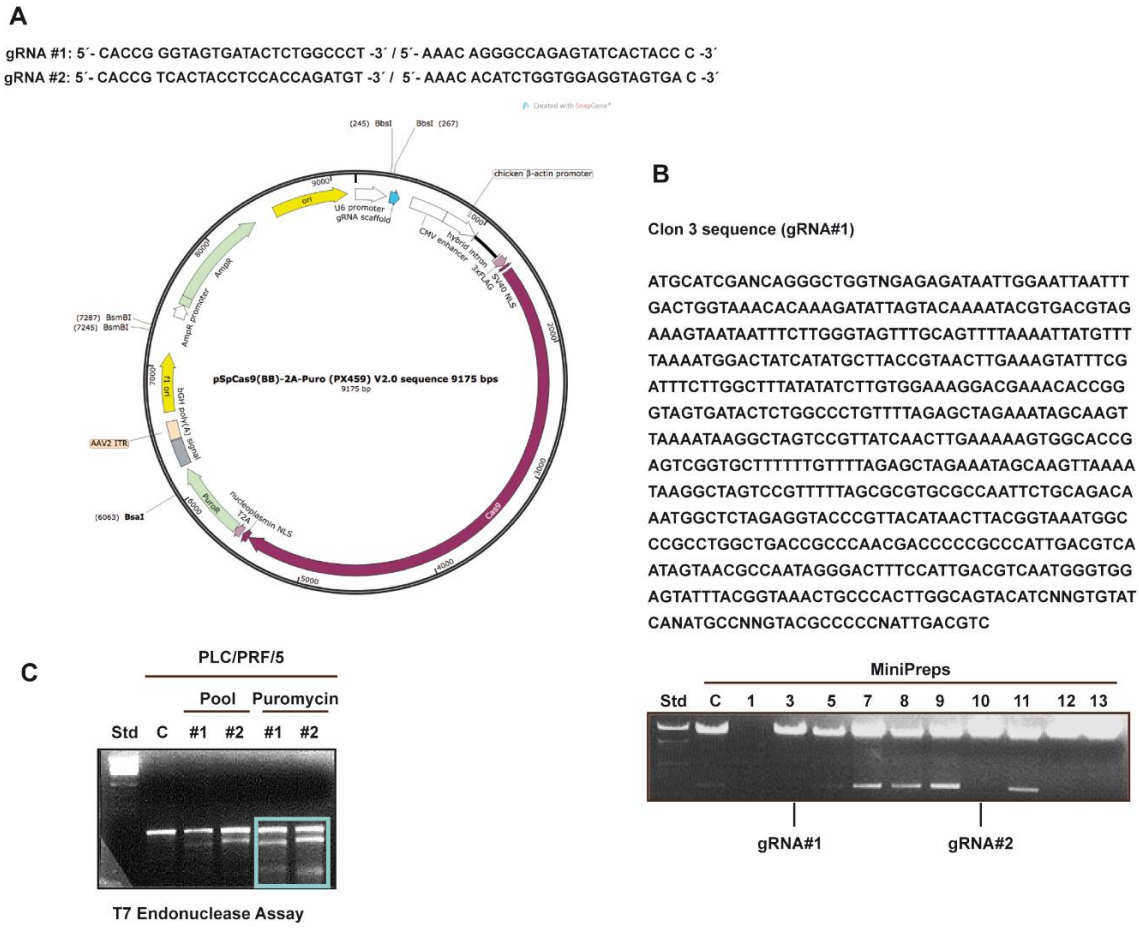

Figure XII. Strategy to silence NOX4 with CRISPR/Cas9 technology in HCC cells. **A** Design of RNA target guides (by bioinformatics tools) and cloning in the Cas9 vector (PX459) that contains resistance to puromycin. **B** Selection of several clones after transformation with the different target guides: analysis of the insertion of the guide in the Cas9 vector by DNA sequencing (**top**) and restriction enzymes (**bottom**). **C** Transfection of the HCC cell line with the different RNA target guides #1 (gRNA#1) or #2 (gRNA#2) and, after puromycin selection, T7 Endonuclease Assay to reveal if the Cas9 vector had worked correctly on the genomic DNA.

Firstly, CRISPR-Cas9 system was optimized by Dr. Noel P. Fusté4 to generate a pool of PLC/PRF/5 and Hep3B cells lacking NOX4 protein. Short-guide RNAs (gRNA) were designed to target the gene (**Table IV**) and then cloned into the pSpCas9(BB)- 2A-puro vector (supplied by Addgene, Watertown, MA, USA), which encodes an RNA polymerase III promotor for the transcription of the guide, the Cas9 endonuclease, and a gene providing

resistance to puromycin. Both cell lines were transfected 12-16h with Lipofectamine® LTX Reagent (Thermo Fisher Scientific, Waltham, Massachusetts, USA). An empty vector without gRNA was used as negative control. Puromycin was added for 24h at 2μg/mL for selection. The selected cells were tested for gene deletion by endonuclease assay and checked for protein knockdown by immunoblot (**Figure XII**).

Secondly, stable transfection with a short hairpin RNA (shRNA) was also used for this thesis' research, as it is a well-characterized model in our group. Cells were transfected with MAtra-A reagent (IBA GmbH, Goettingen, Germany) at a dilution of 1:600 in complete media, 15 minutes on the magnet plate, using 2μg/ml of shRNA plasmid. Two different shRNA plasmids were transfected separately and combined, as well as a control unspecific shRNA (**Table IV**). After 24 hours, media was changed to complete media, and selection of transfected cells was done with puromycin (InvivoGen Therapeutics, France), for at least 30 days prior to experiments. At the beginning, selection was done at a dose of 0.5μg/ml of puromycin, and this dose was gradually increased until reaching 2μg/ml, which is the one used for maintaining the silenced clones. The generation of these cells lines was previously done by Dr. Esther Bertran and Dr. Eva Crosas-Molist[132, 133].

Table IV. Plasmids sequences used in this study

Plasmid		Sequence (5'-3')
CRISPR-Cas9 Silencing	gRNA #1	CACCGGGTAGTGATACTCTGGCCT AAACAGGGCCAGAGTATCACTACCC
	gRNA #2	CACCGTCACTACCTCCACCAGATGT AAACACATCTGGTGGAGGTAGTGAC
ShRNA Silencing	shRNA NOX4 #1	CCGGGAGCCTCAGCATCTGTTCTTACTCGAGTAAGAACAGAT GCTGAGGCTCTTTTTG
	shRNA NOX4 #2	CCGGCAGAGTTTACCCAGCACAAATCTCGAGATTTGTGCTGG GTAAACTCTGTTTTTG

3.5 Transient silencing

For small interference RNA (siRNA) transient silencing, cells were transfected by TransIT-Quest reagent (Mirus, Madison, WI, USA) at 1:300 dilution and a siRNA concentration of 50nM, in complete media. After 8h, cell plates were washed, and fresh media was added. CCND1#1 and #2 siRNA mix was used in all the experiments in a 1:1 ratio. siRNAs were obtained from Sigma-Genosys (Suffold, UK) and their sequences can be checked at **Table V**.

Table V. siRNA sequences used in this study

siRNA	Sequence (5′-3′)
Control	GUAAGACACGACUUAUCGC
CCND1 #1	UGAACAAGCUCAAGUGGAA
CCND1 #2	CCGAGGAGCUGCUGCAAAU

4. Measurement of reactive oxygen species

4.1 NADPH oxidase activity

NADPH oxidase activity can be quantified by exposing the cells to NADPH, which is oxidized to $NADP^+$. NADPH consumption is calculated as the decrease of its concentration, that is, the decrease of the absorbance at λ=340 nm.

So, pelleted cells were incubated with NADPH and the absorbance was measured for 10 minutes in a 96-well plate in duplicate. For analysis of specific NADPH oxidase activity, cells were previously incubated with diphenyleneiodonium (DPI) for 30 minutes (**Table III**). Values are represented as the slopes of the NADPH consumption curves in absence of DPI subtracting the ones in presence of DPI. Results were normalized to protein content and are expressed as picomoles per minute per μg of protein.

4.2 Mitochondrial superoxide

MitoSOX™ Red reagent (#M36008, Invitrogen, UK) was used to determine mitochondrial ROS production. It permeates live cells and is quickly oxidized by $O_{2^{\cdot}}^{-}$ but supposedly not by other ROS or Reactive Nitrogen Species (RNS), becoming highly fluorescent.

24h after seeding the cells in 12-well plates, they were trypsinized and the pellet resuspended in a solution of 5μM MitoSOX™ Red reagent in Hank's Balanced Salt Solution (HBSS, Gibco #14175-053) and incubated for 15 min. After washing with HBSS, the pellet was again resuspended with 300μL HBSS in the flow cytometry tubes. Flow cytometry was performed by using a BD FACS Canto II Cytometer and analysed by BD FACSDiva ™ v9.0 Software (BD Biosciences, San Jose, CA, USA). BD FlowJo™ v10.8.1 Software (BD Biosciences, San Jose, CA, USA) was used for the generation of graphs. All was performed at the Scientific and Technological Centers of the University of Barcelona (CCiTUB).

4.3 Intracellular ROS

To measure the intracellular content of ROS, the 2′,7′-dichlorodihydrofluorescein diacetate (CM-H2DCFDA, Thermo Fisher, #C6827) kit was used. 24 h after seeding the cells in a 12-well plate, they were starved (≥4 h at 0% FBS). 1 h prior to the TGF-β activation (for 3 and 24 h), cells were treated with DPI. Then, a wash with PBS is done and incubated with 2.5 μM H2DCFDA in HBSS for 30 min at 37 ◦C in the dark. Finally, images were taken at the Olympus IX70 microscope.

5. Analysis of apoptosis by Annexin V/PI flow cytometry assay

Apoptosis assessment was done by Annexin V-FITC apoptosis staining (#ab14085, Abcam, Cambridge, UK) with the optimal working concentration optimized prior to the experiments. First, Hep3B Control and CRISPR NOX4 cells were seeded in a 6-well plate. Once the optimal confluence was reached, they were starved at 0% FBS and then treated (or not)

with TGF-β for 48h or 72h. As a control of caspase inhibition, a condition with Q-VD-OPH was added, where cells were incubated with this compound 1 hour before the TGF-β treatment. At the target timepoint, cells, both in the culture medium and attached to the plate, were collected. Next, they are transferred to a flow cytometry tube that contains 1mL of Annexin Binding Buffer (ABB) and centrifuged at 480g for 5 minutes. The supernatant is discarded, and the pellet resuspended in 100µL of ABB containing 6µL of Annexin V-APC and 5µl of Propidium Iodide (PI). After 15 minutes at room temperature (RT) in the dark, 100µl of ABB are added and the reading done.

In **Figure XIII**, the reading of the result in this situation is explained. Q4 shows the population that is negative for both PI and Annexin V, therefore it represents the cells that are alive in those conditions. Next, cells would undergo early apoptosis, being positive for Annexin V, but negative for PI, remaining in the Q3. Finally, that population that continue the apoptotic process and arrive to late apoptosis, would be found in the Q2 quadrant, being positive for both markers.

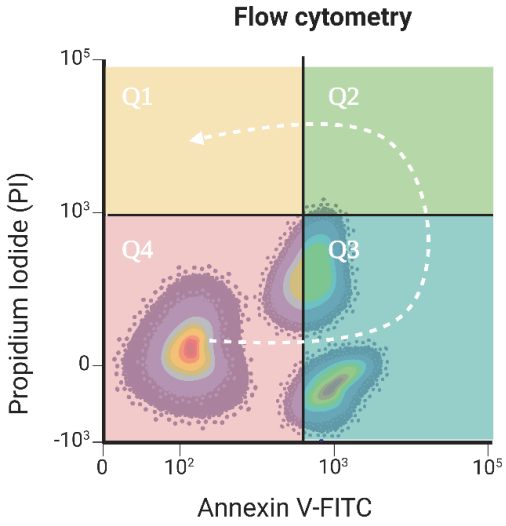

Figure XIII. Flow cytometry graph diagram. Each quadrant (Q1-4) represented. Q1: yellow, Q2: green, Q3: blue, Q4: red. Cell population move following the white arrow as they advance in the apoptosis process.

Flow cytometry was performed by using a BD FACS Canto II Cytometer and analysed by BD FACSDiva ™ v9.0 Software (BD Biosciences, San Jose, CA, USA). BD FlowJo™ v10.8.1 Software (BD Biosciences, San Jose, CA, USA) was used for the generation of graphs. All was performed at the Scientific and Technological Centres of the University of Barcelona (CCiTUB).

6. Analysis of migratory and invasive capacity

6.1 Real-time cell migration analysis

Cell migration was real-time examined through the xCELLigence System (Agilent, Santa Clara, CA, USA). This technique measures electrical impedance through microelectrodes placed in the underside of the membrane which provide quantitative information about the cell attachment. CIM plates were used, as they have an upper chamber with 8µm pores in a polyethylene terephthalate membrane (**Figure XIV**).

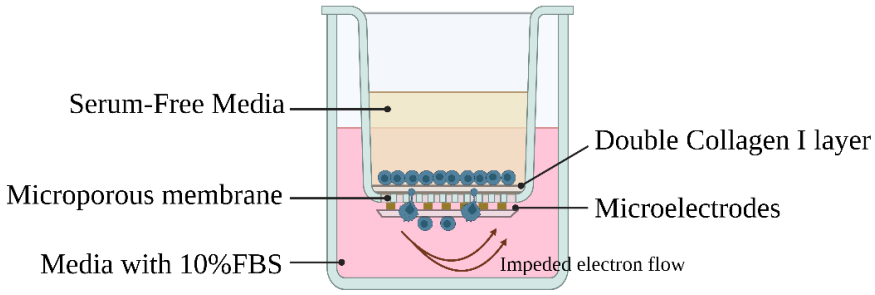

Figure XIV. Schematic diagram of xCELLigence method. Cells are placed in the upper chamber of the CIM-Plate-16, directly on top of a basement membrane matrix previously deposited on the membrane. The impedance sensors on the porous membrane automatically detects cells as they migrate and attach to the impedance microelectrodes in the lower chamber.

To start with, both sides of the upper chamber are coated for 30 minutes with a Collagen IV solution (Sigma-Aldrich, St. Louis, MO, USA) at 25.5µg/cm^2. Then, cells cultured under basal conditions (or after the desired treatment) were pelleted and counted. 3x10^{4}cells were seeded on the top chamber in a volume of 100µl per well. The lower chamber contains media with 10% FBS that works as a chemoattractant. CIM plates are placed onto the Real-time cell analyser (RTCA) station (Agilent, Santa Clara, CA, USA) and cell migration is continuously monitored by the measurement of electrical impedance at the electrode for several hours. Continuous values were represented as normalized cell index, which reflects a relative change in measured electrical impedance, and quantified as a slope (hours^{-1}) of the first 16h of cell migration.

6.2 Invasion analysis

For assays of invasion, first 3D spheroids were created as explained in *section 3.5*. In summary, 5 x10^5 cells/mL were resuspended in low viscosity media at 37◦C-10%CO_2 for 72 h to create the spheroids, with or without TGF-β treatment. Then, they were embedded in Pure Collagen Type I Bovine collagen solution (3 mg/mL) in DMEM media. They were incubated with or without the presence of TGF-β, continuing the treatment and monitorization for 96h. After this time, phase contrast pictures were taken at 4 days at the Leica DMIRD in Scientific and Technological Centers of the University of Barcelona (CCiTUB).

7. Cell viability analysis

7.1 Crystal violet staining

Number of viable cells was determined by crystal violet staining, which allows the quantification of surviving attached cells. Cells were seeded in 24-well plates and cultured under basal conditions or under the desired treatment. Once the target timing is reached, culture media is removed, and cells are washed twice with PBS. The remaining cells are stained with 300µl of crystal violet (0.2% (w/v) in 2% ethanol solution) for 30 min. Then, the solution is removed, and the plate is washed several times with distilled water until de dye excess is gone. Once dried, the stained cells are dissolved in 10% Sodium Dodecyl Sulfate (SDS) on a shaker for 30 min. This step leads to a release of the incorporated dye when the cells are lysed and the SDS is proportionally stained to the number of remaining cells. Absorbance is measured by spectrophotometry, on a plate reader at λ=595 nm, and results are calculated as the difference in percentage of viable cells at the desired times relative to time 0h. Overall, this technique was considered to be a proliferation analysis.

7.2 MTS assay

Cell viability in spheroids was determined by an MTS assay, CellTiter 96® AQueous One solution Cell Proliferation Assay (#G3580A, Promega, Promega Biotech Ibérica S.L.). This assay allows to assess cell viability in a colorimetric method that can be read in a spectrophotometer. At the desired time (0h or 48h), spheroids were collected and incubated in the working solution, as the manufacturer protocol stablished. For every 100µL of media or PBS, 20µL of reagent were added, and spheroids incubated for 2-3h at 37ºC 5% CO_2. The absorbance was recorded at 490nm in a 96-well plate.

8. Protein localization analysis

8.1 Immunohistochemistry

8.1.1 Paraffin embedding

Fresh tissue was cleaned with PBS and included in a cassette for paraffin embedding. Then, they were fixed with PFA (4%) for 12-16h and washed with PBS for 3-4 times.

Table VI. Samples dehydration for paraffin-embedding.

Step	Time
Tap water	30 minutes
Ethanol 70%	60 minutes
Ethanol 96%	60 minutes
Ethanol 96%	60 minutes
Ethanol 96%	Overnight
Ethanol 100%	60 minutes
Ethanol 100%	90 minutes
Ethanol 100%	90 minutes
Xylene	90 minutes
Xylene-Paraffin (50%, 65ºc)	90 minutes
Paraffin (65ºc)	Overnight

After, they were sequentially immersed in PBS-30% saccharose, PBS-20% saccharose and PBS-10% saccharose. Finally, tissue samples were dehydrated in alcohols (Table VI) and embedded in paraffin at 65ºC. For 3D spheroids paraffin inclusion, the protocol followed was the same, except for the timing of the dehydration's steps (**Table VI**), which was approximately reduced to half the minutes.

Once the samples were embedded in paraffin, they were cut into 4µm-thick sections with a microtome and placed in poly-lysinated slides. To poly-lysinate, the slides are incubated for 20 minutes with poly-L-lysine at 4ºC, and air-dryed overnight at 37ºC.

8.1.2 Immunohistochemistry staining in tissue samples

Once the slides are ready, the paraffin needs to be removed and the samples rehydrated. To do so, slides are placed at 50ºC for at least 30 minutes, and next, immersed in the subsequent alcohols, detailed in **Table VII**.

Table VII. Samples rehydration for immunohistochemistry

Step	Time
Xylene	10 minutes
Xylene	10 minutes
Xylene	10 minutes
Ethanol 100%	5 minutes
Ethanol 100%	5 minutes
Ethanol 100%	5 minutes
Ethanol 96%	5 minutes
Ethanol 96%	5 minutes
Ethanol 96%	5 minutes
Ethanol 70%	5 minutes
Distilled water	5 minutes

After rinsing the samples in distilled water, they are immersed in a mixture of citric acid (0.38mg/mL) and sodium citrate (2.45mg/mL), where they are taken to boiling temperature

and boiled for 2 minutes. This process allows the methylene bridges to break and the antigenic sites to expose, so the antibodies can better bind. Next, boiled samples are left to rest so the temperature can decrease under 40ºC, for approximately 20 minutes, and rinsed for 5 minutes with distilled water. After this, the endogenous peroxidases are inactivated, to minimize the background signal, by incubating the slides in 3% hydrogen peroxide for 10 minutes and next washing them in distilled water for 5 minutes. Then, a 10-minute wash with PBS-T (0.1%) is made. The next step is to block the samples at RT in Blocking solution (2% Bovine serum albumin (BSA) and 20% FBS in PBS-Tween (PBS-T)) during 2h in a wet chamber. Finally, the slides are incubated 16h in a wet chamber at 4ºC with the corresponding primary antibody (**Table XV**) diluted in the blocking solution.

Next day, slides are first washed thrice in PBS-T (0.1%) for 10 minutes and incubated during 1h with the secondary peroxidase-conjugated antibody (α-Rabbit (#PK4001) or α-Mouse (#PK4002), Vectastain ABC KIT, Vector Laboratories Inc., Burlingame, CA, USA) following the manufacturer's protocol. Then, slides are washed three times again with PBS-T (0.1%) for 10 minutes. Afterwards, they were incubated in ABC (Vectastain ABC KIT, Vector Laboratories Inc., Burlingame, CA, USA) for 30 minutes. Finally, the peroxidase staining with diluted Diaminobenzidine (DAB) (#K3468, DAKO, Inc., Carpinteria, CA, USA) was performed. The duration of this step depends on the antibody and samples used, but it was always taken care of not saturating the signal. The reaction was stopped by immersing the slides in tap water for 5 minutes once the optimal staining was obtained.

Final steps consist of doing a counterstaining with Mayer's Haematoxylin (#HHS32, Sigma Aldrich, St. Louis, MO, USA) and the subsequent dehydration as detailed in Table VIII. Finally, slides were mounted in DPX (#360294H, BDH Prolabo, Germany) with their coverslips for a correct preservation.

Table VIII. Samples dehydration after immunohistochemistry

Step	Time
Ethanol 70%	5 minutes
Ethanol 96%	5 minutes
Ethanol 96%	5 minutes
Ethanol 96%	5 minutes
Ethanol 100%	5 minutes
Ethanol 100%	5 minutes
Ethanol 100%	5 minutes
Xylene	10 minutes
Xylene	10 minutes
Xylene	10 minutes

8.1.3 Haematoxylin and Eosin staining

Haematoxylin and Eosin staining (H&E) of mice livers was performed in the histological service in IDIBELL. However, the H&E staining for 3D spheroids slides was performed in the laboratory. Once the slides are ready, the paraffin needs to be removed and the samples rehydrated. To do so, slides are placed at 50ºC for at least 30 minutes, and next, immersed in the subsequent alcohols (**Table IX**).

Table IX. Samples rehydration for immunohistochemistry in 3D

Step	Time
Xylene	5 minutes
Xylene	5 minutes
Xylene	5 minutes
Ethanol 95%	5 minutes
Ethanol 70%	5 minutes
Distilled water	5 minutes

After the rehydration, samples were stained for 10 seconds with Harris Haematoxylin solution (#HHS32, Sigma Aldrich, St. Louis, MO, USA). Once slides were washed with tap water for 1-2 minutes, they were submerged in chlorohydric acid for 1 second, and washed

twice again in tap water for 2 minutes each. Next, the samples are stained with Eosin Y solution (#115935.0100, Merck) for 5 seconds. Finally, samples are dehydrated by immersing them in the alcohols, as specified in **Table X**, and mounted with DPX as explained in the previous section.

Table X. Samples dehydration for immunohistochemistry in 3D

Step	Time
Ethanol 70%	5 minutes
Ethanol 90%	5 minutes
Ethanol 100%	5 minutes
Xylene	5 minutes
Xylene	5 minutes
Xylene	5 minutes

8.2 Immunofluorescence

Confocal and epifluorescence microscopic analyses were performed on two-dimensional and three-dimensional cell cultures.

8.2.1 Immunofluorescence staining n 2D culture

For monolayer cell cultures, cells were seeded under basal or treated conditions on gelatine-coated glass coverslips in 24-well plates. In the desired endpoint, cells were washed with PBS and fixed with 4% PFA in PBS for 20 minutes. When needed, cells were permeabilized with 0.1% Triton-X-100 in PBS for 2 exact minutes and washed with PBS at least thrice. Then, they were incubated in blocking solution, which consists of 10% FBS and 1% Bovine Serum Albumin (BSA) in PBS, at RT for 1h. In this case, primary antibodies (**Table XV**) are prepared in 1% PBS-BSA in a 1:50 dilution, and incubated for 1h at RT, too. After three washes of 5 minutes in PBS, the glasses are incubated with fluorescent-conjugated secondary antibodies, anti-mouse Alexa Fluor-488 (#A11001, Invitrogen, ThermoFisher Scientific, OS, USA) or anti-rabbit Alexa Fluor-488 (#A11008, Invitrogen, ThermoFisher Scientific, OS, USA), in a 1:200 dilution in 1% PBS-BSA for 1h at RT. Following, cells are washed again for 5

minutes three times with PBS. Finally, glasses are embedded with Mowiol (#P36935, Invitrogen, ThermoFisher Scientific, OS, USA), which is a reagent that contains 4',6-diamidino-2-phenylindole (DAPI) to stain nuclear DNA.

8.2.2 Immunofluorescence in 3D spheroids

Immunofluorescence in 3D spheroids was performed in paraffin-embedded slides, as explained in *section 8.1.1*. Once the slides are ready, the paraffin needs to be removed and the samples rehydrated. To do so, slides are placed at 50ºC for at least 30 minutes, and next, immersed in the subsequent alcohols, detailed in **Table VII**. After the deparaffination, the antigen unmasking is made in a mixture of citric acid (0.38mg/mL) and sodium citrate (2.45mg/mL), where they are taken to boiling temperature and boiled for 2 minutes. Next, boiled samples are left to rest so the temperature can decrease under 40ºC, for approximately 20 minutes, and rinsed for 5 minutes with distilled water.

After a 5 minutes wash in PBS in agitation, the blocking is done at RT in Blocking solution (1% BSA and 10% FBS in PBS) during 1h in a wet chamber. Then, the slides are incubated for 1h in a wet chamber at RT with the corresponding primary antibody (**Table XV**) diluted 1:100 in 1% BSA in PBS. Once this step is done, the slides are washed three times in PBS, and then incubated with fluorescent-conjugated secondary antibodies, anti-mouse Alexa Fluor-488 (#A11001, Invitrogen, ThermoFisher Scientific, OS, USA), anti-mouse Alexa Fluor-555 (#A21424, Invitrogen, ThermoFisher Scientific, OS, USA) or anti-rabbit Alexa Fluor-488 (#A11008, Invitrogen, ThermoFisher Scientific, OS, USA), in a 1:200 dilution in 1% PBS-BSA for 1h at RT. Finally, slides are washed three times with PBS, adding DAPI in the last wash for nuclear staining. Slides are then mounted in DPX with their coverslips for a correct preservation.

8.3 Image acquisition

Representative images from immunohistochemistry (IHQ) staining were taken in Nikon eclipse 80i microscope with a Nikon DS-Ri1 digital camera and using NIS-Elements BR

3.2 (64-bit) software. Images from immunofluorescences have been taken either with a Nikon eclipse 80i microscope, with a Nikon DS-Ri1 digital camera and using NIS-Elements BR 3.2 (64-bit) software, or in a Carl Zeiss LSM880 Confocal Microscope at the Scientific and Technological Centre of the University of Barcelona (CCiTUB). Representative images were taken and edited in Adobe Photoshop (Adobe, San José, CA, USA). Image J software and Fiji software (National Institute of Health (NIH), Bethesda, MD, USA) were used for managing and quantifying images from images with the same exposure conditions.

9. Protein expression analysis

9.1 Cell lysis

Cells were cultured in the desired conditions and at final timepoint, placed on ice. Media was removed, or collected when specifically studying apoptotic processes, and a double wash with PBS was carried out. Then, cells were scrapped with 2ml of PBS and collected in a tube, repeating this process again.

Table XI. RIPA lysis buffer composition

Compound	Working concentration
Sodium deoxycolate	5mm
Tris-HCl – pH 7.4	20mm
SDS	0.1%
Triton-X-100	0.5%
NaCl	150mm
EDTA	2mm
PMSF	1mm
Leupeptin	5µg/ml
Sodium orthovanadate	0.1mm
DTT	0.5mm
B-glycerolphsophate	20mm

EDTA: Ethylenediaminetetraacetic acid; **PMSF**: phenylmethylsulfonyl fluoride

Cells were centrifuged at 1250rpm for 8 minutes at 4ºC and resuspended with RIPA lysis buffer (**Table XI**) for 1h in rotation at 4ºC. Finally, the eppendorfs were centrifuged at 13000rpm for 10 minutes at 4ºC and the supernatants collected and stored at -80ºC.

9.2 Protein quantification

Protein concentration was determined by using Bio-Rad Protein Assay Dye Reagent Concentrate (Bio-Rad Laboratories, Hercules, CA, USA). The reagent is prepared by diluting it in distilled water at a 1:5 ratio. After, 200µl of the mix is added to 10µl of the diluted sample in each well of a 96-well plate in duplicate. For each time, a standard curve of known protein concentration was prepared with BSA from 0 to 2µg/ml. Absorbance is then measured by spectrophotometric analysis at λ=595 nm and normalized to the standard curve.

9.3 Biochemical analysis by fractionation kits

As explained in the introduction (*section 3.3.2*), subcellular localization of NOX4 protein is very controversial. To try to elucidate this, biochemical analysis was performed by several fractionation kits.

9.3.1 Subcellular localization

Subcellular Protein Fractionation Kit (Thermo Scientific, #78840) was used to isolate the whole cell extract into: total, cytoplasm, membrane, soluble nucleus, and chromatin fractions.

Cells were cultured under basal conditions and harvested with trypsin, then centrifuged to acquire a cell pellet. They were washed with cold PBS and at least 10^6 cells were transferred to an Eppendorf and pelleted again. Then, the supernatant was discarded, and the remaining pellet resuspended with the adequate volume of the first buffer, the Cytoplasmic Extraction Buffer (CEB). After 10 minutes of incubation at 4ºC, the tube was centrifuged at 500x *g* for 5 minutes. The supernatant obtained from this is the cytoplasmic fraction, which was kept in ice. Then, cold Membrane Extraction Buffer (MEB) was added to the pellet and the tube vortexed

for at least 5 seconds to ensure a good mixing. Following another incubation at 4ºC for 10 minutes, the tube was again centrifuged for 5 minutes at 3000x *g*. The supernatant obtained from this is the membrane fraction, which was kept in ice, too. After, cold Nuclear Extraction Buffer (NEB) was added to the pellet and the tube vortexed for 15 seconds. Once the incubation at 4ºC for 30 minutes was finished, a centrifuge at 5000x *g* for 5 minutes is done. The supernatant obtained from this is the soluble nuclear fraction, which was kept in ice, too.

The chromatin-bound extraction buffer was prepared by mixing 5µl of 100mM $CaCl_2$ with 3µl of Micrococcal Nuclease in 100µl of RT NEB. This mixture is then added to the remaining pellet and vortexed for 15 seconds. Then, it was incubated at RT for 15 minutes and, after another vortex of 15 seconds, centrifuged at 16000x *g* for 5 minutes. The supernatant obtained from this is the chromatin-bound nuclear fraction, which was kept in ice. Finally, RT Pellet Extraction Buffer (PEB) was added and vortexed for 15 seconds. Once the incubation at RT for 10 minutes was done, the tube was centrifuged for 5 minutes at 16000x *g*. The supernatant obtained from this is the cytoskeletal fraction, which was kept in ice. All the tubes were kept at -80ºC for long-term storage and when analysed, it was proceeded as a Western Blot (WB) analysis.

9.3.2 Endoplasmic Reticulum Isolation Kit

Endoplasmic Reticulum Isolation Kit (#ER0100, Sigma-Aldrich, St. Louis, MO, USA) was used to separate the organelle from the total fraction, following manufacturer's protocol.

Cells were cultured under basal conditions and harvested with trypsin, then centrifuged to acquire a cell pellet. Then, pellet is suspended in a volume of Hypotonic Extraction Buffer three times the pellet volume and incubated for 20 minutes at 4ºC. After a centrifugation at 600g for 5 minutes, supernatant is removed. Pellet is resuspended in a volume of Isotonic Extraction Buffer two times the pellet volume and transferred to a Dounce homogenizer. Cells are broken and then proceed to differential centrifugation steps.

Centrifugation is done at 1000g for 10 minutes at 4ºC. Once the thin lipid layer is aspirated, the supernatant is transferred to another centrifuge, and the pellet discarded. The supernatant is centrifuged at 12000g for 15 minutes at 4ºC. Again, the thin lipid layer is discarded, and the remaining supernatant transferred to a new tube. This is the Post Mitochondrial fraction (PMF), which is next ultracentrifuged at 100000g for 60 minutes at 4ºC. The supernatant is discarded, and the pellet washed with Isotonic Extraction Buffer (IEB) to homogenize again. From now on, the procedure needs to be performed at 4ºC. The microsomal sample that we have just obtained is diluted in OptiPrep Density Gradient Medium and mixed well. Then, some more OptiPrep solution is layered on top of the sample. Then, an ultracentrifuge at 150000g for 3 hours is done. After carefully removing the supernatant, the remaining pellet is resuspended in 200µl of IEB. This will be the ER fraction. All the tubes were kept at -80ºC for long-term storage and when analysed, it was proceeded as a WB analysis.

9.3.3 Mitochondrial Isolation Kit

Finally, the Mitochondria Isolation Kit (#MITOISO2, Sigma-Aldrich, St. Louis, MO, USA) was the kit used to divide the cytosol and the mitochondria.

Cells were cultured under basal conditions and harvested with trypsin, then centrifuged to acquire a cell pellet. Cells are washed twice with ice-cold PBS and counted. Per every $2{,}5 \cdot 10^7$ cells, add approximately1.5mL of Lysis Buffer, and incubate in ice for 5 minutes maximum. Then, 2 volumes are added of Extraction Buffer and all the mix is centrifuged at 600g for 10 minutes. Carefully, transfer the supernatant to another tube. Centrifuge again at 11000g for 10 minutes at 4ºC and discard the supernatant. Finally, the pellet is resuspended in 200-400 µL of Protein Extraction Reagent Type 4. All the tubes were kept at -80ºC for long-term storage and when analysed, it was proceeded as a WB analysis.

9.4 Protein immunodetection by Western Blot

Denaturalizing SDS-polyacrylamide gel electrophoresis (SDS-PAGE) was performed to separate proteins in their molecular weight. Samples were prepared by mixing LaemmLi Buffer (**Table XII**) with the desire μg of protein and denaturalizing them at 95ºC for 5 minutes.

Doing this procedure, the proteins are denatured and acquire a negative charge, so they will move through the gel towards the positive charge proportionally to the size of the polypeptide. Acrylamide gels consist of the stacking and the resolving gel. On one side, the first is always prepared at 5% acrylamide concentration to stack all the proteins together. But on the other side, the latter can be prepared at different acrylamide concentrations, ranging from 6% to 15%, depending on the size of the protein of interest. The higher the concentration in the gel, the smaller the polypeptides that can be discriminated. For instance, to study the proteins involved in apoptosis, the polyacrylamide concentration of choice was 15%, as they tend to weigh between 15-25kDa.

Table XII. LaemmLi buffer composition

Compound	Working concentration
Tris-HCl Ph 6.8	40mM
SDS	1%
Glycerol	5%
DTT	2.5mM
NaCl	150mM
Bromophenol blue	0.02%
β-Mercaptoethanol	5%

The prepared gels were assembled in the electrophoresis tank and filled with the running buffer detailed in **Table XIII**. Then, protein samples were loaded in the gel wells with a molecular weight standard, and electrophoresis was carried out at constant voltage.

Table XIII. SDS-PAGE running buffer composition

Compound	Working concentration
Tris-HCl pH 8.3	25mM
Glycine	192mM
SDS	0.1%

After the completion, proteins are transferred to a nitrocellulose membrane (GE Healthcare, Life Sciences, Germany) using wet transfer technique. Before starting, the nitrocellulose membrane needs to be immersed in distilled water until hydrated. Then, the equipment is put together, from top to bottom: 3 wattman papers – acrylamide gel – nitrocellulose membrane – 3 wattman papers. The assemble is submerged in Towbin transfer buffer (**Table XIV**) inside the tank. Electrical current of 300mA was applied for 30min to 75min, depending on the size of the protein of interest. Following this, the membrane was stained with 0.5% red Ponceau solution in 1% acetic acid, to confirm the efficiency of the transfer, and carefully washed off with PBS-T 0.05%.

Table XIV. Towbin transfer buffer composition

Compound	Working concentration
Tris-HCl pH 8.3	25mM
Glycine	192mM
Methanol	20%

To mask the unspecific antibodies, the membrane was incubated in 5% non-fat dry milk in PBS-T for 1h at RT. Then, it was incubated with the primary antibody in 0.5% of that solution at 4ºC overnight, in motion. Primary antibodies used in this thesis are detailed in **Table XV**.

Once finished, the membrane is washed with PBS-T thrice for 10 minutes each and incubated 1h at RT in motion with the secondary antibody diluted in 1:3000 in 0.5% milk in PBS-T. Secondary antibody, conjugated with peroxidase, was anti-mouse (GE Healthcare,

#NA931V) or anti-rabbit (GE Healthcare, #NA934V) depending on the host of the primary antibody used. After, the membrane is washed with PBS-T three times.

For the visualization of the protein, the membrane was incubated with ECL™ Western blotting detection reagent (GE Healthcare, Life Science, UK), a chemiluminescent solution, and exposed in a ChemiDoc™ Touch Imaging System from Bio-Rad (Bio-Rad Laboratories, Hercules, CA, USA). Densitometric analysis of protein bands intensity and size was performed with Image J software (National Institute of Health (NIH), Bethesda, MD, USA).

Table XV. Antibodies and conditions used in this study

Primary antibody	Secondary antibody	Working dilution	Application	Reference
AKT	Rabbit	1:1000	WB	Cell Signaling #9272
ATPb	Mouse	1:1000	WB	Abcam #ab556467
Bcl-xL	Mouse	1:1000	WB	BD Biosciences #610746
Calreticulin	Mouse	1:1000	WB	Abcam #ab22683
CD163	Rabbit	1:1000 / 1:50 /1:100	IHC, IF	Abcam #ab182422
CD68	Rabbit	1:1000 / 1:50 /1:100	IHC, IF	Abcam #ab125212
Collagen 1	Mouse	1:1000	IHC	Abcam #ab6308
Cyclin D1	Mouse	1:500	WB	BD Biosciences #55647
E-cadherin	Mouse	1:50	IF	BD Biosciences #610182
EGFR	Rabbit	1:1000	WB	Cell Signaling #2232
GAPDH	Mouse	1:1000	WB	Milipore #MAB374
Hic-5	Mouse	1:1000 / 1:50	WB, IF	BD Biosciences #611165
Histone 3	Rabbit	1:1000	WB	Abcam #ab1791
Hsp27	Mouse	1:1000	WB	Cell Signaling #2402
Ki67	Rabbit	1:1000 / 1:50 /1:100	IHC, IF	Abcam #ab16667
MCL1	Mouse	1:1000	WB	Santa Cruz #sc-12756

MYC	Rabbit	1:1000	WB	Abcam #ab32072
N-cadherin	Mouse	1:50	IF	BD Biosciences #610920
NOX4	Rabbit	1:1000	WB	Prosci #7927
NOX4	Rabbit	1:1000 / 1:50	WB, IF	Abcam #ab62352
pAKT (Ser473)	Rabbit	1:1000	WB	Cell Signaling #4060
pEGFR (Tyr1068)	Rabbit	1:1000	WB	Cell Signaling #3777
Phalloidin	-	1:500	IF	Sigma #P1951
pSMAD2 (Ser465/467)	Rabbit	1:1000	WB	Cell Signaling #3108
pSMAD3 (Ser423/425)	Rabbit	1:1000	WB	Milipore #07-1389
SMAD2	Mouse	1:1000	WB	Cell Signaling #3103
SMAD3	Rabbit	1:1000	WB	Abcam #ab40854
Vinculin	Mouse	1:50	IF	Sigma #V9131
α-SMA	Rabbit	1:1000	IHC	Abcam #ab5694
β-ACTIN	Mouse	1:3000	WB	Sigma #A5441

WB: Western blot; **IF**: Immunofluorescence; **IHC**: Immunohistochemistry

10. Gene expression analysis

10.1 RNA isolation and reverse transcription

E.Z.N.A.® Total RNA Kit II (Omega bio-tek, Norcross, GA, USA) was used for total RNA isolation following manufacturer's instructions. Culture plates pellets were washed with PBS and scrapped or pipetted with RLT lysis buffer containing 20µl/mL of β-mercaptoethanol. 1000ng of total RNA isolated from each sample was reverse transcribed with random primers

for complementary DNA synthesis, using a High Capacity RNA to cDNA Master Mix Kit (Applied Biosystems, Foster City, CA, USA), according to the manufacturer's protocol.

10.2 Quantitative Real Time PCR

RNA expression levels were determined in duplicate in a LightCycler® 480 Real-time PCR system, using the LightCycler® 480 SYBR Green I Master Mix (Roche Diagnostics GmbH, Mannheim, Germany) in 384-well plate. For each well, 5µl of SYBR Green Master Mix, 3 µl of RNAse Free Water, 1 µl of specific primers and 1 µl of diluted cDNA were mixed. Gene expression levels were normalized to housekeeping gene/s suitable in each condition. Primer sequences can be found at **Table XVI** (human) or **Table XVII** (mouse).

Table XVI. Human primer sequences used in LightCycler 480 SYBR Green System quantitative PCR

Gene	Forward (5'-3')	Reverse (3'-5')
BCL2L1	CCTGCCTGCCTTTGCCTAA	CCCGGTTGCTCTGAGACATT
BCL2L11	TAAGTTCTGAGTGTGACCGAGA	GCTCTGTCTGTAGGGAGGTAGG
BMF	CAAATCTGAACAAGCCCAAGTCTTCCAG	CACACAGCTTAGTGAGCAGAACACAA
CCND1	AGCTGTGCATCTACACCGAC	GAAATCGTGCGGGGTCATTG
CDC42	CAGGGCAAGAGGATTATGACAG	GTTATCTCAGGCACCCACTT
HPRT1	CCTGGCGTCGTGATTAGTGA	CGAGCAAGACGTTCAGTCCT
L32	AACGTCAAGGAGCTGGAAG	GGGTTGGTGACTCTGATGG
MCL1	TGCTTCGGAAACTGGACATCA	TAGCCACAAAGGCACCAAAAG
MMP9	ACCTCGAACTTTGACAGCGACA	GATGCCATTCACGTCGTCCTTA
MYC	CCCGCTTCTCTGAAAGGCTCTC	CTCTGCTGCTGCTGCTGGTAG
NOX4	GCAGGAGAACCAGGAGATTG	CACTGAGAAGTTGAGGGCATT
RAC1	GCTTTTCCCTTGTGAGTCCTG	CCTTCAGTTTCTCGATCGTGTC
RHOA	AGCTGGGCAGGAAGATTATG	CGTTGGGACAGAAATGCTTG
RHOC	CAAGACGAGCACACCAGG	AGCACTCAAGGTAGCCAAAG
SERPINE1	TCTGCCCTCACCAACATTC	GGTCATTCCCAGGTTCTCTAG
SMAD7	CGGACAACAAGAGTCAGCTGGT	GTCCTGGAGTCCGGGTTGTC
SNAI1	GCTGCAGGACTCTAATCCAGAGTT	GACAGAGTCCCAGATGAGCATTG
SNAI2	ACACATTAGAACTCACACGGG	TGGAGAAGGTTTTGGAGCAG

TBP	CCGCCGGCTGTTTAACTTC	AGAAACAGTGATGCTGGGTCA
VIM	CGTGAATACCAAGACCTGCTC	GGAAAAGTTTGGAAGAGGCAG

Table XVII. Mouse primer sequences used in LightCycler 480 SYBR Green System quantitative PCR.

Gene	Forward (5'-3')	Reverse (3'-5')
Arp	CGACCTGGAAGTCCAACTAC	ATCTGCTGCATCTGCTTG
Nox4	TCCAAGCTCATTTCCCACAG	CGGAGTTCCATTACATCAGAGG
Acta2	TCACCATTGGAAACGAACGC	CCCCTGACAGGACGTTGTTA
Col1a1	GAGAGGTGAACAAGGTCCCG	AAACCTCTCTCGCCTCTTGC
CD68	CCTGACAAGGGACACTTCGG	GAGGACCAGGCCAATGATGA
CD163	TGCTGTCACTAACGCTCCTG	TCATTCATGCTCCAGCCGTT

10.3 RNA sequencing analysis

This experiment was carried out at the Centro Nacional de Análisis Genómico (CNAG). Samples were prepared by creating a pool of the three extractions made in each animal. RNA from *Mus musculus* was quantified by Qubit® RNA BR Assay kit (Thermo Fisher Scientific) and the RNA integrity was estimated by using RNA 6000 Nano Bioanalyzer 2100 Assay (Agilent). The RNAseq libraries were prepared with KAPA Stranded mRNA-Seq Illumina® Platforms Kit (Roche) following the manufacturer´s recommendations. Briefly, 500ng of total RNA was used for the poly-A fraction enrichment with oligo-dT magnetic beads, following the mRNA fragmentation. The strand specificity was achieved during the second strand synthesis performed in the presence of dUTP instead of dTTP. The blunt-ended double stranded cDNA was 3´adenylated and Illumina platform compatible adaptors with unique dual indexes and unique molecular identifiers (Integrated DNA Technologies) were ligated. The ligation product was enriched with 15 PCR cycles and the final library was validated on an Agilent 2100 Bioanalyzer with the DNA 7500 assay. The libraries were sequenced on HiSeq 4000 (Illumina) with a read length of 2x51bp+17bp+8bp using HiSeq 4000 SBS kit (Illumina) and HiSeq 4000

PE Cluster kit (Illumina), following the manufacturer's protocol for dual indexing. Image analysis, base calling and quality scoring of the run were processed using the manufacturer's software Real Time Analysis (RTA 2.7.7).

RNA-seq reads were processed using fastp v0.21[206], including adapter removal, trimming of low-quality reads (Q<30) and removal of reads with undetermined bases. Afterwards, processed reads were aligned against Mus musculus reference genome using GENCODE release M32 (GRCm39) using STAR v2.7.9[207] and quantification of aligned reads to transcripts per million (TPM) was done with RSEM v1.3.1[208].

Differential gene expression analysis was performed with DESeq2 for the conditions of interest, after performing an initial exploratory analysis using Principal Component Analysis (PCA). All analyses were performed using R v4.0.4 (https://www.R-project.org/).

A collection of gene signatures was obtained from MSigDB v2023.1[209] and gene set variation analysis (GSVA)[210] was used with log2-normalized TPMs to assess the relative activation of the signatures in the samples. Additionally, ComplexHeatmap package was used to plot the relative log2TPM gene expression between the samples.

For immune deconvolution, immunedeconv package[211] and the tool Tumor Immune Estimation Resource (TIMER) 2.0[212] were used. Two methods were selected: SeqImmuCC, which outputs the relative abundance of 10 immune cell types and mMCP-counter, that reports cell type scores for different immune subpopulations. SeqImmuCC deconvolution was represented as barplots of relative abundance for each immune cell type. Additionally, mMCP-counter results from TIMER2.0 were used to assess differences between samples for specific immune subpopulations with Mann-Whitney U test, adjusting for multiple comparisons.

11. Data analysis

11.1 Statistical analyses

Overall, experiments were performed at least 3 independent times and data is represented as mean ± standard deviation (SD). All statistical tests were calculated with GraphPad Prism software (GraphPad for Science Inc., San Diego, CA, USA). Differences between two groups were compared using parametric analysis (Student's t-test, with Welch correction if needed) or unparametric analysis if suited. If different conditions were being compared, a two-way ANOVA test was used with multiple comparison post-hoc test. Differences were considered statistically significant at $p<0.05$ (*), $p<0.01$ (**) and $p<0.001$ (***).

11.2 TCGA database

The Cancer Genome Atlas (TCGA) gene expression profiles (log2TPM) from 327 hepatocellular carcinoma cases from TCGA Liver Hepatocellular Carcinoma (TCGA-LIHC)[213] were downloaded from TCGA2BED[214] FTP repository. Clinical data for these cases was downloaded from Genomics Data Commons data portal[215]. Samples were categorized as low stroma when the percentage of stromal cells was below <15%. Correlation was assessed using Pearson correlation tests and corrected for multiple testing. Gene expression levels were stratified using the median of each gene. For survival analyses, Kaplan-Meier curves were plotted, and statistical assessment was performed with Log-rank test. In the case of gene expression signatures (**Table XVIII**), GSVA[210] was used to assess the relative activation of the signature in the samples. Differences in mean MMP9 or TGFB1I1 expression between NOX4 low and NOX4 high were tested using a Mann-Whitney U test. P-values were corrected for multiple testing with Bonferroni. All analyses were performed using R 4.0.4[216].

Table XVIII. TGF-β signalling from Hallmarks of Cancer Signature gene members*:*

ACVR1	CDK9	HIPK2	LTBP2	RAB31	SMAD6	THBS1
APC	CDKN1C	ID1	MAP3K7	RHOA	SMAD7	TJP1
ARID4B	CTNNB1	ID2	NCOR2	SERPINE1	SMURF1	TRIM33
BCAR3	ENG	ID3	NOG	SKI	SMURF2	UBE2D3
BMP2	FKBP1A	IFNGR2	PMEPA1	SKIL	SPTBN1	WWTR1
BMPR1A	FNTA	JUNB	PPM1A	SLC20A1	TGFB1	XIAP
BMPR2	FURIN	KLF10	PPP1CA	SMAD1	TGFBR1	
CDH1	HDAC1	LEFTY2	PPP1R15A	SMAD3	TGIF1	

RESULTS

Dissecting the role of NOX4 in TGF-β signalling in HCC

1. Generation and characterization of the cellular models

As previously described by our group and others, some HCC cells can respond to TGF-β, through the canonical pathway, in terms of inhibition of proliferation and apoptosis. However, HCC cells may also respond to it undergoing EMT, increasing their invasive and migratory capacity, through the non-canonical TGF-β signalling[65]. Additionally, NOXs are important mediators of TGF-β actions on hepatocytes, macrophages, and stellate cells. Particularly, NOX4 has emerged the last years as a potential tumour suppressor in the liver, due to its role as a mediator for TGF-β's pro-apoptotic activity in hepatocytes and HCC[52], [132], but its potential role in TGF-β's protumorigenic actions had not been studied. To further elucidate the molecular mechanisms that are regulated by this axis and how NOX4 expression impacts to the different responses to TGF-β, cellular models of loss of NOX4 expression were used in this thesis.

In this first part, we have used CRISPR Cas9 technology to stably attenuate NOX4 expression in PLC/PRF/5 and Hep3B HCC cell lines (*see section 3.4*). Previous results from our group had shown that PLC/PRF/5 cells are a good model to analyse the response to TGF-β in terms of proliferative inhibition, while Hep3B cell line offers a great tool to analyse the response to TGF-β in terms of EMT and apoptosis.

Both these cell lines express elevated levels of NOX4 mRNA and protein, so they were stably silenced by CRISPR Cas9 technique, as shown in **Figure 1A**. In both cell lines a good downregulation, though not a total knock-out (KO) was achieved. To further confirm NOX4 silencing, a functional assay was performed. Being NOX4 a NADPH oxidase, which oxidizes NADPH to NADP+, its enzymatic activity can be analysed with that goal. First, cells were

incubated with or without DPI, an inhibitor of NOX family members. In this way, NOXs specific NADPH consumption was measured when cells were incubated in the presence of NADPH and its reduction measured at λ=340nm (**Figure 1B**). Importantly, a reduction in NADPH oxidase activity was observed after silencing NOX4 in both PLC/PRF/5 and Hep3B cell lines.

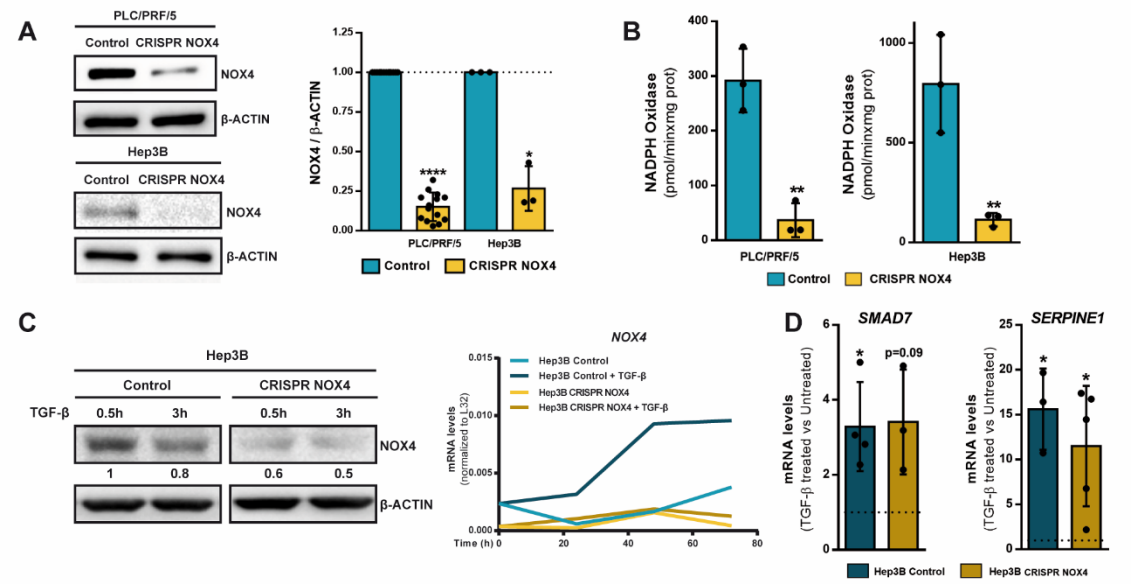

Figure 1. Characterization of the cellular models used in this study. PLC/PRF/5 and Hep3B cells were stably transfected with either with Control or CRISPR NOX4. **A** NOX4 protein levels analysed by western blot. β-Actin was used as loading control. Representative experiment (**left**) and densitometric quantification of NOX4 levels relative to β-Actin (**right**). Data are Mean ± SD, n≥3). **B** Analysis of NADPH oxidase activity by the decrease in NADPH with and without the addition of DPI (10μM). Results expressed as picomoles per minute per μg of protein. Data are Mean ± SD (n=3). **C** NOX4 protein levels analysed by western blot after TGF-β treatment at 0.5 and 3h. β-Actin was used as loading control (**left**). *NOX4* mRNA expression analysed by RT-qPCR, normalized to housekeeping gene *L32*, after TGF-β treatment at 24, 48 and 72 hours (**right**). Representative experiments are shown. **D** *SMAD7* and *SERPINE1* mRNA expression analysed by RT-qPCR, normalized to housekeeping gene *L32*, after 48h TGF-β treatment, represented as fold induction (TGF-β-treated versus untreated cells). Data are mean ± SD (n=6). Statistical analysis, where indicated: *p<0.05 **p<0.01, ***p<0.001, comparing CRISPR NOX4 cells versus Control in A and B and TGF-β-treated versus untreated condition in D.

These results demonstrate a good efficiency of NOX4 silencing. As previously mentioned, NOX4 is upregulated in response to TGF-β[52] in hepatocytes and HCC cells. Response to TGF-β was impaired in terms of NOX4 upregulation, either at the protein and at

the RNA level, both at short (0.5-3h) and long (24-72h) treatment (**Figure 1C**). Moreover, other targets of this cytokine were analysed to check if the whole pathway was affected by NOX4 silencing. However, the increase in the expression of different TGF-β target genes, such as *SMAD7* and *SERPINE1*, was not affected, meaning that TGF-β signalling was functional (**Figure 1D**). Altogether, we can say that these are good models to study TGF-β-NOX4 axis.

Another important point to assess when working with NOX4, is the ROS production, as another functional proof that the downregulation is efficient. Firstly, an intracellular ROS analysis was performed by using H_2DCFDA, a molecule that has an adduct that turns fluorescent when oxidized (*see Section 4.3*). Hep3B cells were treated for 3h and 24h with TGF-β and then incubated with H_2DCFDA. Microscopy images (**Figure 2A**) revealed an attenuation of the intracellular ROS production after TGF-β treatment in Hep3B CRISPR NOX4 cells, compared with the increase seen in Hep3B Control after the same treatment.

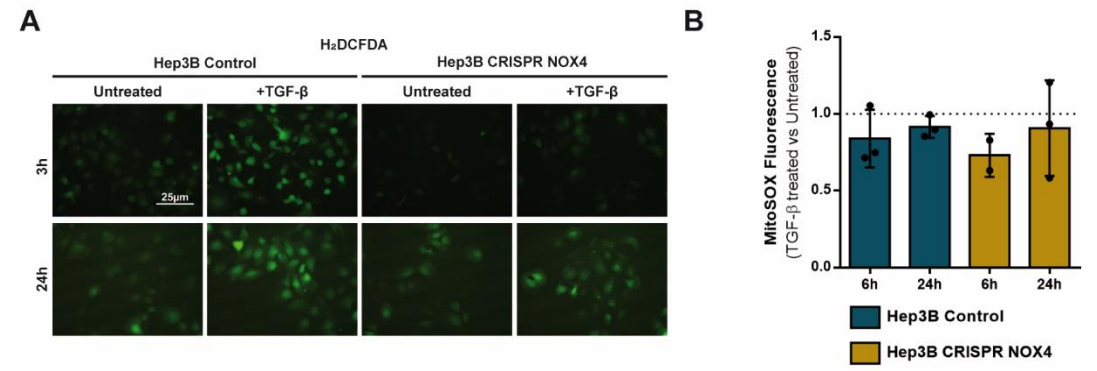

Figure 2. Analysis of ROS in the cellular models used in this study. Analysis made in Hep3B Control and CRISPR NOX4 cells. **A** Analysis of intracellular ROS content by H_2DCFDA (green) after TGF-β treatment. Scale bar, 25μm. **B** Mitochondrial O_2- analysed fluorometrically using MitSOX™. Results are expressed as fold induction (TGF-β-treated versus untreated cells). Data are mean ± SD (n≥3).

Another important source of ROS in cells is the mitochondria, considered one of the major contributors of $O_2^{\cdot-}$ in cells[90]. Therefore, mitochondrial superoxide was checked by MitoSOX™ (*see Section 4.2*). Hep3B cells were analysed after 6h and 24h of TGF-β treatment by flow cytometry. Results showed no changes in mitochondrial ROS after treatment, nor in

Hep3B Control or Hep3B CRISPR NOX4 cells (**Figure 2B**). This result was consistent with previous results from the group in another model[133].

Overall, these results demonstrate that these cell lines confer a good model to analyse the crosstalk between TGF-β and NOX4, and that the silencing of NOX4 is performed correctly and is enough.

2. NOX4 role in TGF-beta antitumorigenic actions

2.1 In terms of canonical and non-canonical signalling

TGF-β's canonical pathway involves the phosphorylation of SMADs, that translocate to the nucleus to upregulate several target genes, *NOX4* being one of them[217]. Besides, the non-canonical pathway involves EGFR and phosphorylation of AKT and can counteract the suppressor arm[218]. We knew then, that TGF-β was regulating NOX4 levels, but whether NOX4 silencing had any retrospective effect on TGF-β signalling, was not completely clear. So, once these cellular models were validated, the response to TGF-β when NOX4 is silenced was analysed.

PLC/PRF/5 was the chosen cell line and to do so, phosphorylation of different proteins that conform the TGF-β signalling pathways was checked by western blot. Firstly, the canonical pathway was analysed, which is composed of several SMAD-family proteins. A decrease in the phosphorylation of SMAD2 and SMAD3 was found after TGF-β treatment in NOX4 silenced PLC/PRF/5 cells. The results of several western blot analysis were quantified by densitometry and expressed as the ratio between phospho-SMAD2/3 and their corresponding total SMAD (**Figure 3A-B**). In PLC/PRF/5 CRISPR NOX4, the attenuation of the response to TGF-β in terms of SMAD phosphorylation was observed, which was almost significant in the case of SMAD3 (**Figure 3B**).

To analyse the relevance of the attenuation of SMAD signalling on the TGF-β-mediated transcriptional activity, we analysed the expression of *SERPINE1* and *SMAD7* (**Figure 1D**), as two important genes regulated by this cytokine. In this case, their expression was upregulated by TGF-β in both cases, whether in Hep3B Control or Hep3B CRISPR N4 cell line, meaning that the pathway was not affected.

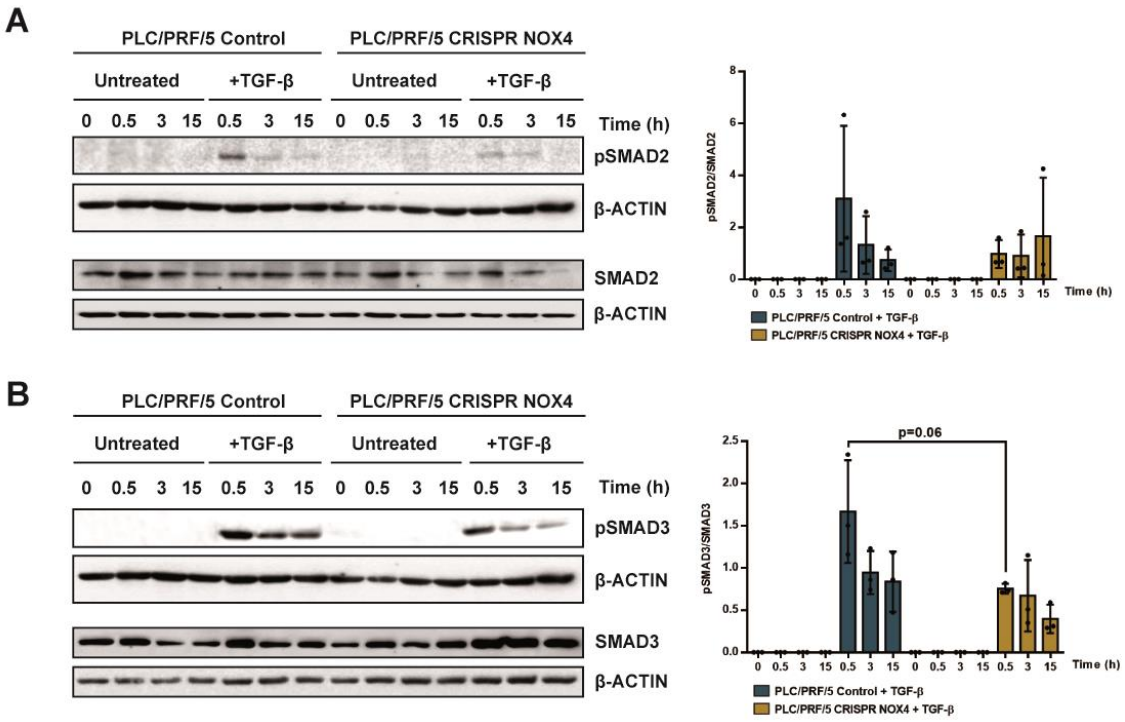

Figure 3. Role of NOX4 on TGF-β-mediated canonical signals. Analysis made in PLC/PRF/5 (Control and CRISPR NOX4) cells, untreated or TGF-β-treated. **A** Phospho-SMAD2 and total SMAD2; **B** Phospho-SMAD3 and total SMAD3. In both cases, Western blot (**left**), β-Actin was used as loading control. Representative experiments. Quantification of the Phospho/Total ratio in each case (**right**), after densitometric analysis of the levels taking into account the specific loading control [(Phospho)/(phospho loading)]/[(Total)/(total loading)]. Data are Mean ± SD (n = 3).

These results indicate that, although an attenuation of SMAD phosphorylation is observed in CRISPR NOX4 cells, the consequence on their transcriptional effects is weak or not significant. The next step was to check for the non-canonical TGF-β pathway as the transactivation of EGFR pathway often mediates this attenuation (*see section 2.3.1*). As previously explained, it is known that AKT, downstream of EGFR, can inhibit the upregulation

of NOX4 by TGF-β[59]. Therefore, the levels of phosphorylation of AKT and EGFR were analysed by western blot. We observed that silencing NOX4 led to an increase in AKT phosphorylation compared to the PLC/PRF/5 Control (**Figure 4**), while its total protein levels remained unchanged. All these translates in an increased tendency, almost significant, of the ratio pAKT/AKT, as expressed in **Figure 4**. However, EGFR phosphorylation was increased when in CRISPR NOX4 cells, both at untreated and treated conditions. Moreover, total levels of EGFR showed a decrease during the culture, independently of the treatment status. As the high levels of EGFR accompanied the increase in its phosphorylation in NOX4-silenced cells, even at basal levels, the differences in the ratio pEGFR/EGFR were unsignificant.

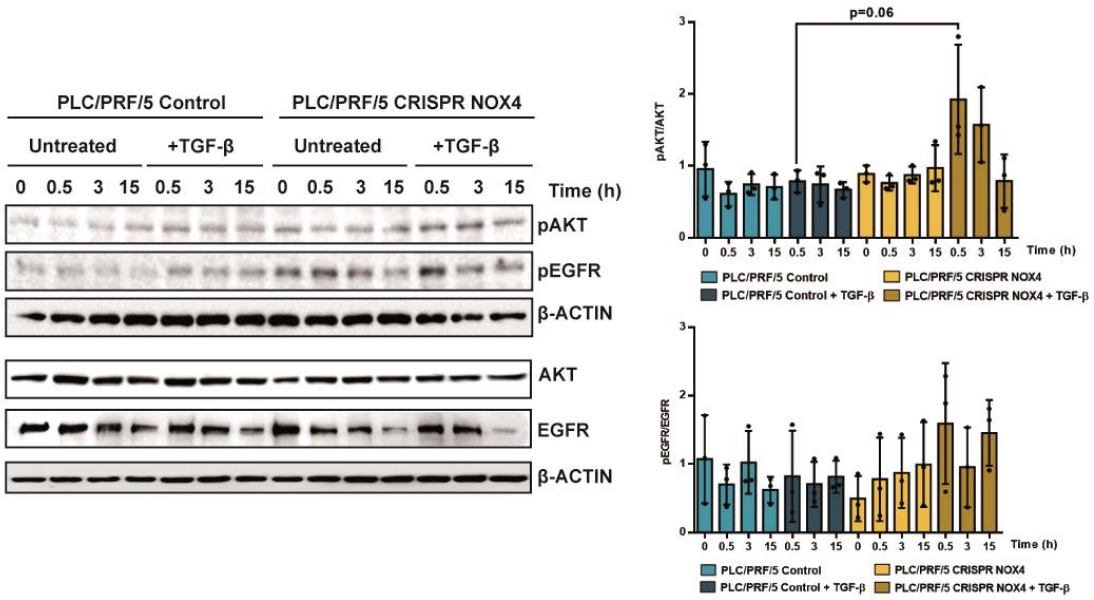

Figure 4. Role of NOX4 on TGF-β-mediated non-canonical signals. Analysis made in PLC/PRF/5 (Control and CRISPR NOX4) cells, untreated or TGF-β-treated. Phospho-AKT, phospho-EGFR and their corresponding total protein levels (**left**). In both cases, Western blot, β-Actin was used as loading control. Representative experiments. Quantification of the Phospho/Total ratio in each case (**right**), after densitometric analysis of the levels taking into account the specific loading control [(Phospho)/(phospho loading)]/[(Total)/(total loading)]. Data are Mean ± SD (n = 3).

These results evidence that stable silencing of NOX4 leads to a shift from the TGF-β-induced canonical tumour-suppressor pathway (SMADs) to an activation of the TGF-β non-

canonical pro-tumorigenic signalling (EGFR/AKT). All in all, these could contribute to decrease the response to TGF-β in terms of growth inhibition and apoptosis.

2.2 In terms of growth inhibition

Previous results from the group showed that stably knocking down NOX4 in human liver tumour cells increased cell proliferation, being found in a higher proportion of S/G2/M phases of the cell cycle[219]. Moreover, an increase in c-Myc protein and RNA levels correlated with NOX4 silencing[133], corroborating this last part.

As a way of checking the cell model of silencing *NOX4* by CRISPR-Cas9, we analysed c-Myc levels at basal conditions. On one hand, *MYC* RNA expression was significantly increased in PLC/PRF/5 when NOX4 was silenced (**Figure 5A**). On the other hand, c-Myc protein levels were also found to be upregulated in absence of NOX4, both in PLC/PRF/5 or Hep3B cell lines. As shown in **Figure 5B-C**, the western blot analyses and their respective densitometric quantification can be seen. Besides, Cyclin D1 (*CCND1*) is one of the most described cell-cycle-related gene that acts as a regulator of CDK and of cell cycle G1/S transition. As a c-Myc regulated gene[220], we decided to explore it further. In parallel to the results observed at basal conditions, expression of Cyclin D1 was really high both at mRNA and protein levels in PLC/PRF/5 and Hep3B CRISPR NOX4 cells (**Figure 5A-C**).

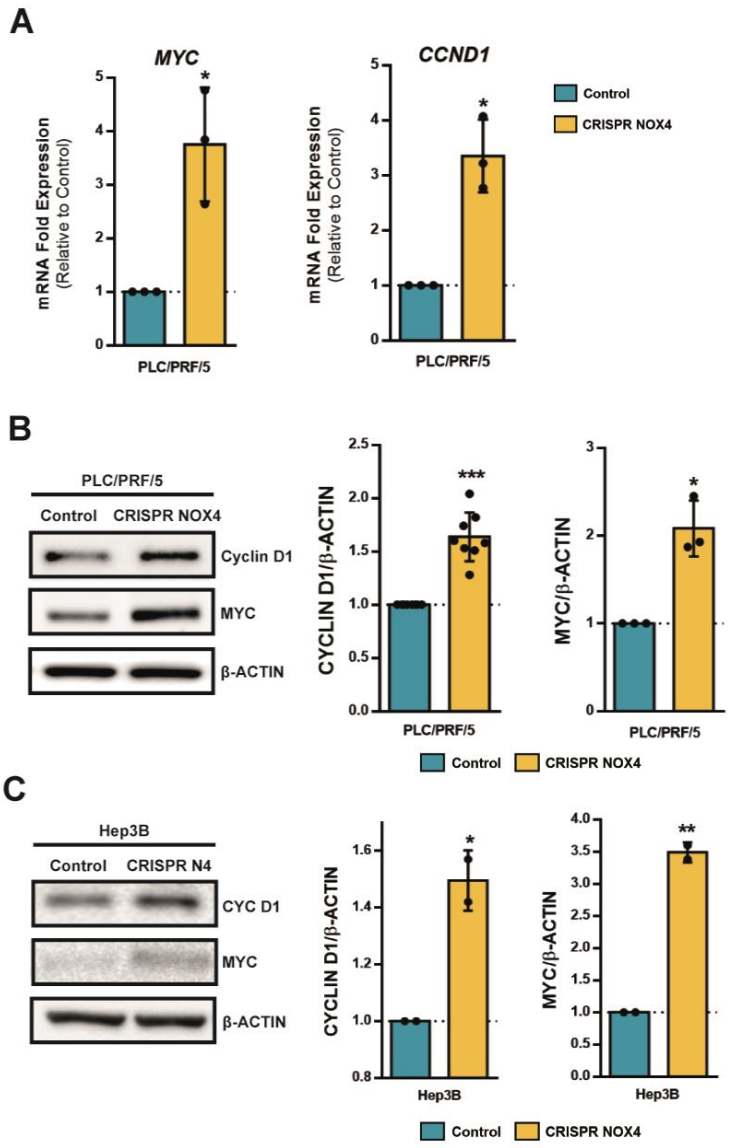

Figure 5. ***MYC*** **and** ***CCND1*** **(Cyclin D1) expression levels in HCC (Control and CRISPR NOX4) cells. A** *MYC* and *CCND1* mRNA expression analysed by RT-qPCR, normalized to housekeeping gene *L32*, in PLC/PRF/5 cells. **B-C** c-MYC and Cyclin D1 protein levels analysed by Western blot in both PLC/PRF/5 (**B**) and Hep3B (**C**) cells. β-Actin was used as loading control. Representative experiment (**left**) and densitometric quantification of protein levels expressed as relative to β-Actin (**right**). Results are expressed as fold induction relative to control. Data are Mean ± SD (n≥ 3). *p<0.05 **p<0.01, ***p<0.001

Repressing mitogen-induced MYC expression is known to be an important mechanism to inhibit proliferation by TGF-β[221], even in hepatocytes[222]. Taking this into account, the response to TGF-β in terms of cell proliferation in HCC cells was analysed when NOX4 was silenced. To do so, a crystal violet staining was analysed after 72h of TGF-β-treatment in PLC/PRF/5 cells, where the bigger proliferative capacity of NOX4-silenced cells can be seen (**Figure 6A**). Also, while Control cells show a significant reduction in their proliferative capacity when treated with TGF-β, CRISPR NOX4 cells did just show a slight tendency. This fact is accompanied by the result that *MYC* mRNA levels were not downregulated by TGF-β

treatment in PLC/PRF/5 CRISPR NOX4 cells, while the inhibition was clearly seen in Control ones (**Figure 6B**).

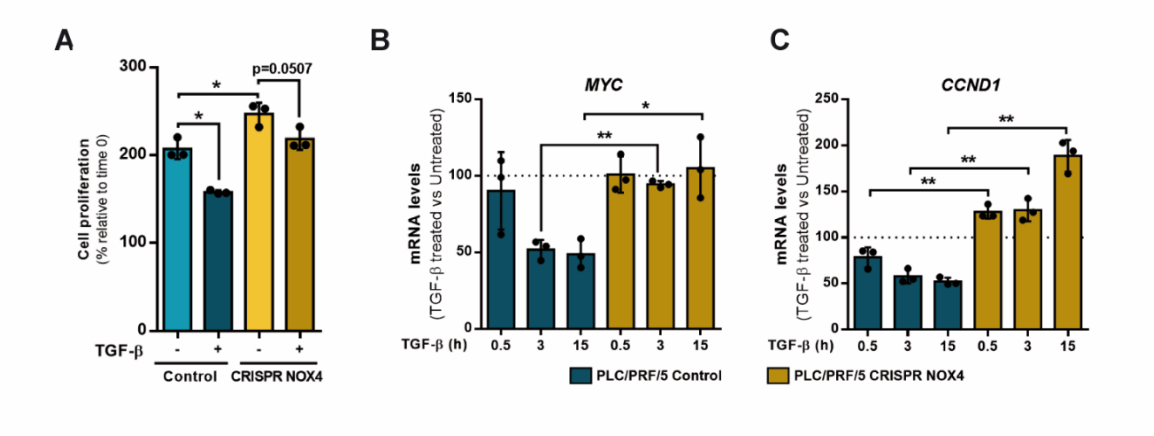

Figure 6. Role of NOX4 in the response to TGF-β in terms of cell proliferation. Analysis made in PLC/ PRF/5 Control and CRISPR NOX4 cells. **A** Cell viability assay analysed by crystal violet staining after 72h of TGF-β treatment, normalized to initial time (time 0h). Data represents mean ± SD of triplicates from one representative experiment. **B** Relative *MYC* and **C** *CCND1* mRNA expression analysed by RT-qPCR, normalized to housekeeping gene *L32*, after TGF-β treatment at 0, 0.5, 3 and 15 h. Represented as percentage of TGF-β treated versus untreated cells in each time. Data are Mean ± SD (n≥ 3). *p<0.05 **p<0.01

Interestingly, PLC/PRF/5 CRISPR NOX4 cells did not show the TGF-β mediated down-regulation of Cyclin D1 by RNA expression as the PLC/PRF/5 Control did. In fact, *CCND1* expression even increased in time in PLC/PRF/5 CRISPR NOX4 (**Figure 6C**). Consequently, in order to analyse the crosstalk of NOX4 and Cyclin D1 in terms of HCC cell proliferation, a transient silencing of Cyclin D1 with a specific siRNA was performed (*see section 3.5*) (**Figure 7A**). Expectedly, knocking down Cyclin D1 strongly inhibited proliferation, as it is crucial for cells to grow. In the analysis by crystal violet (**Figure 7B**), both PLC/PRF/5 Control and CRISPR NOX4 cells had a significant reduction in proliferative capacity, minimizing their differences in cell growth.

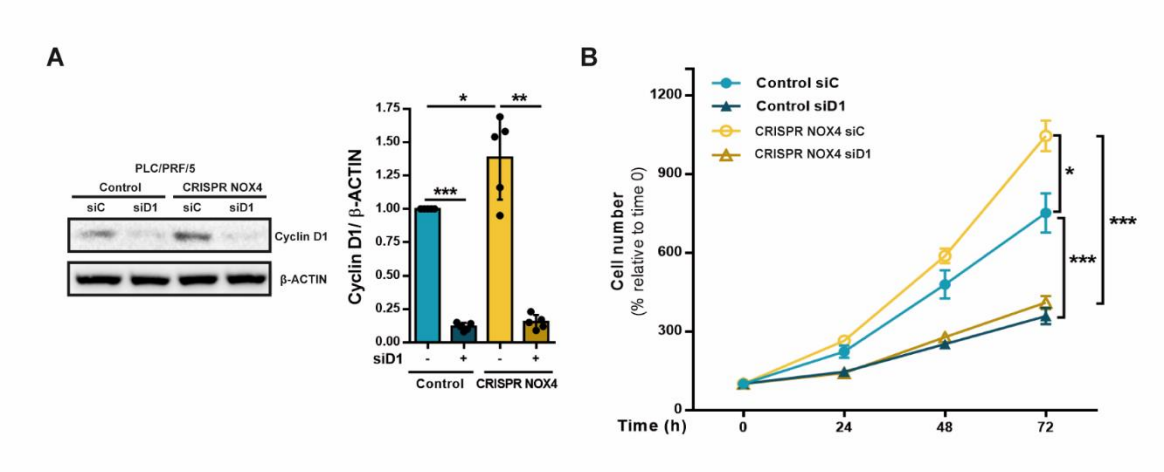

Figure 7. Role of Cyclin D1 in cell proliferation. Analysis made in PLC/ PRF/5 Control and CRISPR NOX4 cells **A** Cyclin D1 protein levels analysed by Western blot after transiently transfecting either with control or Cyclin D1 specific siRNA sequences. β-Actin was used as loading control. Representative experiment (**left**) and densitometric analysis of Cyclin D1 levels relative to β-Actin (**right**). **B** Cell proliferation assay analysed by crystal violet staining after transiently transfecting with either control or Cyclin D1 specific siRNA sequences, normalized to initial time (time 0h). Data are Mean ± SD (n = 3). *p<0.05 **p<0.01 ***p<0.001. (siC: Control siRNA; siD1: Cyclin D1 siRNA).

Next, we wondered whether Cyclin D1 could be upstream or downstream of this axis. Not only silencing Cyclin D1 did not affect the upregulation of NOX4 (**Figure 8A**), but also it did not affect the downregulation of MYC by TGF-β treatment (**Figure 8B**), showing that it acts downstream of these signals regulating cell cycle. The basal overexpression of Cyclin D1 and MYC and their impossibility of being downregulated by TGF-β, may explain the lack of response to the cytokine in terms of growth inhibition in CRISPR NOX4 cells.

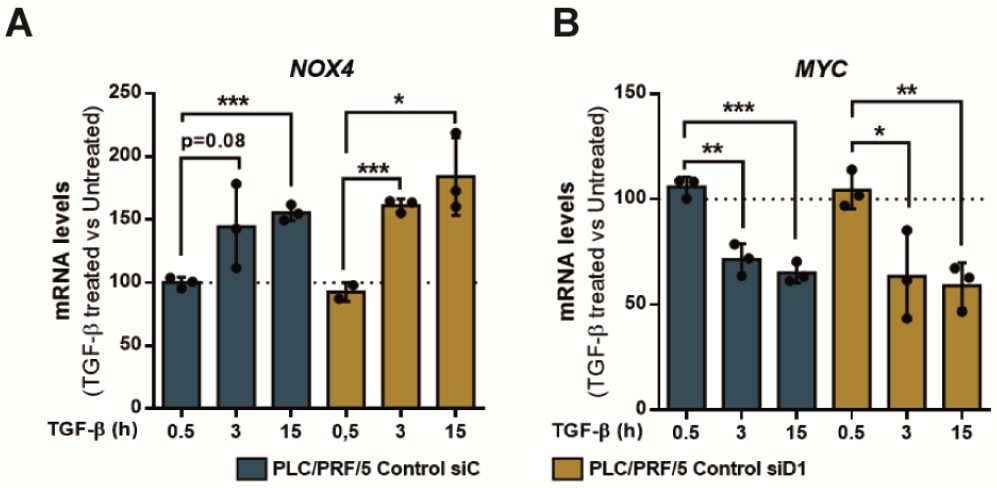

Figure 8. Role of NOX4 in the response to TGF-β in terms of cell proliferation. Analysis made in PLC/ PRF/5 Control cells after transiently transfecting either with control or Cyclin D1 specific siRNA sequences **A** Relative *NOX4* and **B** *MYC* mRNA expression analysed by RT-qPCR, normalized to housekeeping gene *L32*, in Control CRISPR PLC/PRF/ 5 cells transiently transfecting with either control or Cyclin D1 specific siRNA sequences: effect of TGF-β treatment at 0, 0.5, 3 and 15 h. Data are represented as percentage of TGF-β treated versus untreated cells in each time. Data are Mean ± SD (n = 3). *p<0.05 **p<0.01 ***p<0.001. (siC: Control siRNA; siD1: Cyclin D1 siRNA).

2.3 In terms of apoptosis

Previous published results from the group had pointed at NOX4 as a mediator of apoptotic activity from TGF-β[223,59] (*see section 2.1.1*). With the objective of further investigating this axis, Hep3B cell line was chosen as it induces an apoptotic response with the treatment.

Apoptotic or pycnotic nuclei, which appear as fragmented nuclei, are one of the hallmarks of Caspase 3 activation. Therefore, a first step to assess this cascade was to stain the cells, untreated or treated with TGF-β for 48 hours, with DAPI. In **Figure 9**, it is seen that silencing NOX4 leads to a decrease in the fragmented nuclei (marked with white arrows) found after treatment. These results brought us to further investigate apoptosis in a deeper manner.

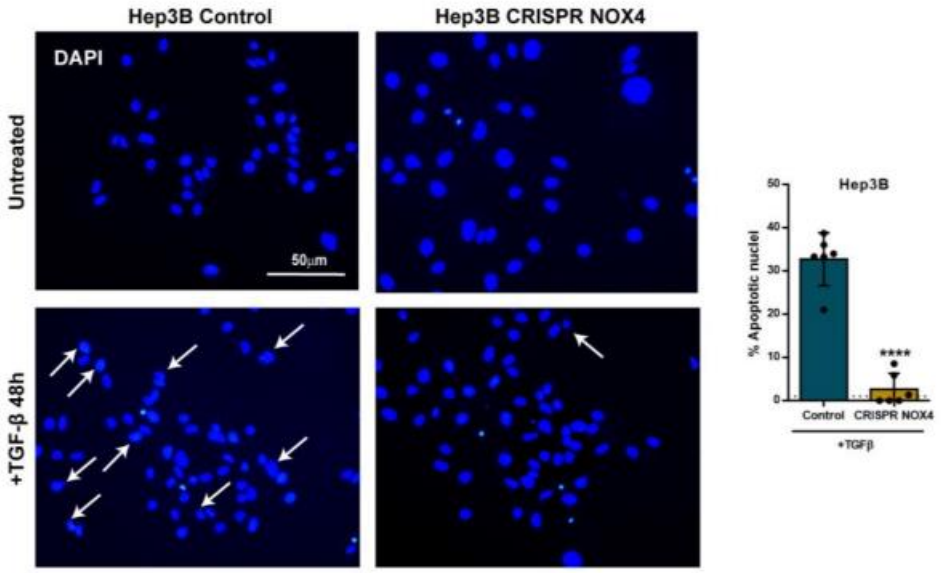

Figure 9. Role of NOX4 on TGF-β-induced apoptosis in terms of pyknotic nuclei. Analysis of fragmented nuclei (arrows) after DAPI (blue) staining in cells untreated or treated during 48 h with TGF-β. Representative images (**left**) and quantitative analysis (using ImageJ software), each dot representing one field (**right**).

To continue, apoptosis was analysed by Annexin V/PI staining by flow cytometry at 48h and 72h (*see section 5*). Q-VD-OPH was used as a caspase-3 inhibitor. After TGF-β treatment, Hep3B Control cells showed a higher percentage of cells in Q3 quadrant, meaning early apoptosis as they are Annexin V+, but PI-; and in Q2 quadrant, showing late apoptosis accumulation, as they are positive for both markers (**Figure 10A**). However, in the case of Hep3B CRISPR NOX4, cells showed less apoptosis, either at Q3 or Q4, when activated with TGF-β for 48h and 72h (**Figure 10A-B**).

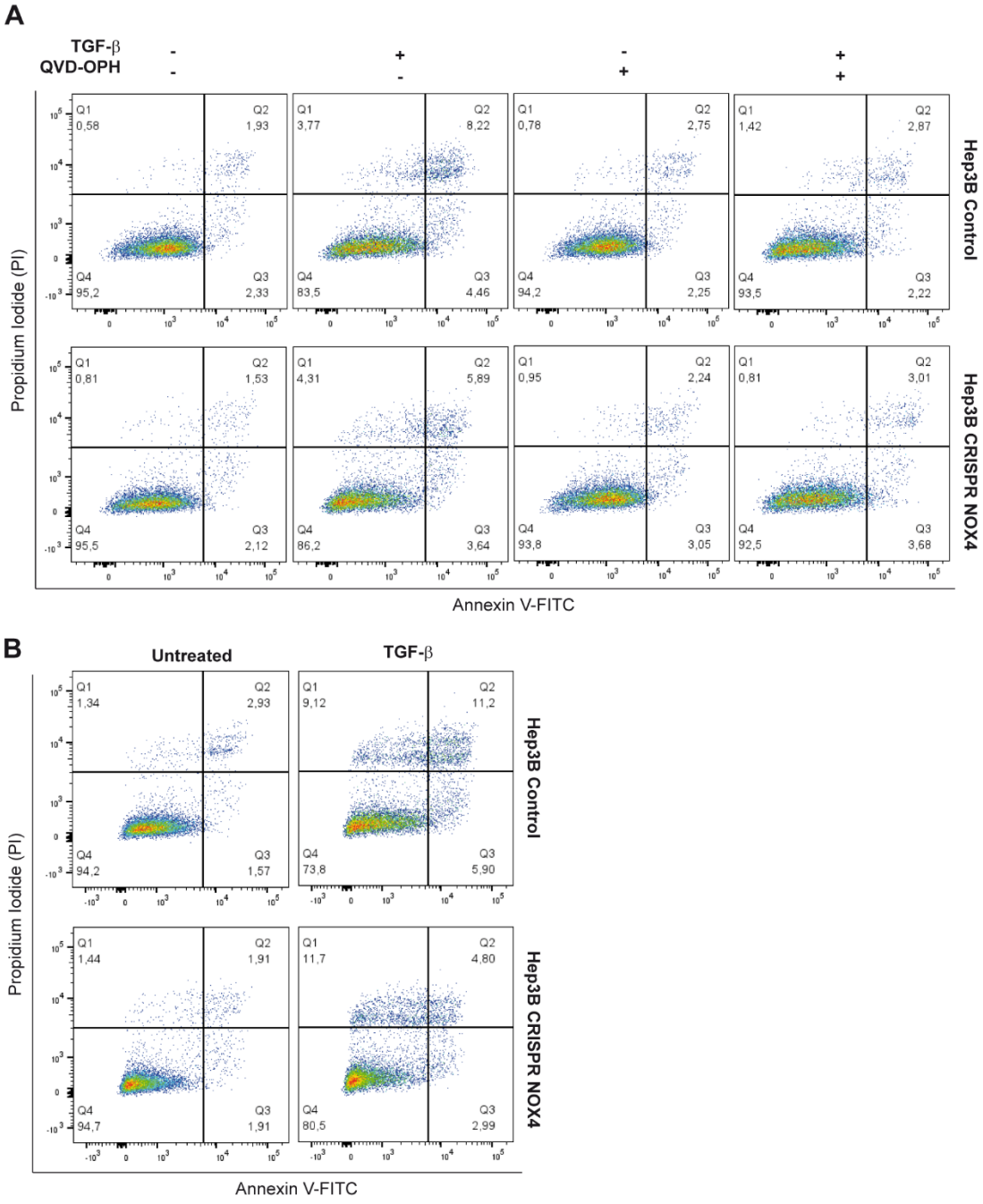

Figure 10. Role of NOX4 on TGF-β-induced apoptosis. Analysis made in Hep3B (Control and CRISPR NOX4) cells. **A-B)** Representative flow cytometry plots using Annexin V-FITC/PI staining for analysis of apoptosis in Hep3B (Control and CRISPR NOX4) treated with TGF-β for 48h (**A**) or 72h (**B**). In A, co-treatment with Q-VD-OPH, supporting the role of caspases in the process.

Once it had been proved that TGF-β-mediated apoptosis was decreased after stably silencing NOX4, we wondered which could be the molecular mechanisms that were regulating that. After TGF-β treatment for 48 hours, RNA expression of several genes implicated in this

pathway were analysed (**Figure 11A**). To start with, *BMF* and *BCL2L11* (BIM) were checked, as two pro-apoptotic Bcl-2 family members that are induced by TGF-β[223,59] (*see section 2.1.1*). Both genes increased their expression after TGF-β treatment, but there were no visible differences between cell lines. Following, two anti-apoptotic genes were analysed: *BCL2L1* (Bcl-xL) and *MCL-1*, which showed no regulation prompted by TGF-β, and no particular difference when silencing NOX4 (**Figure 11A**).

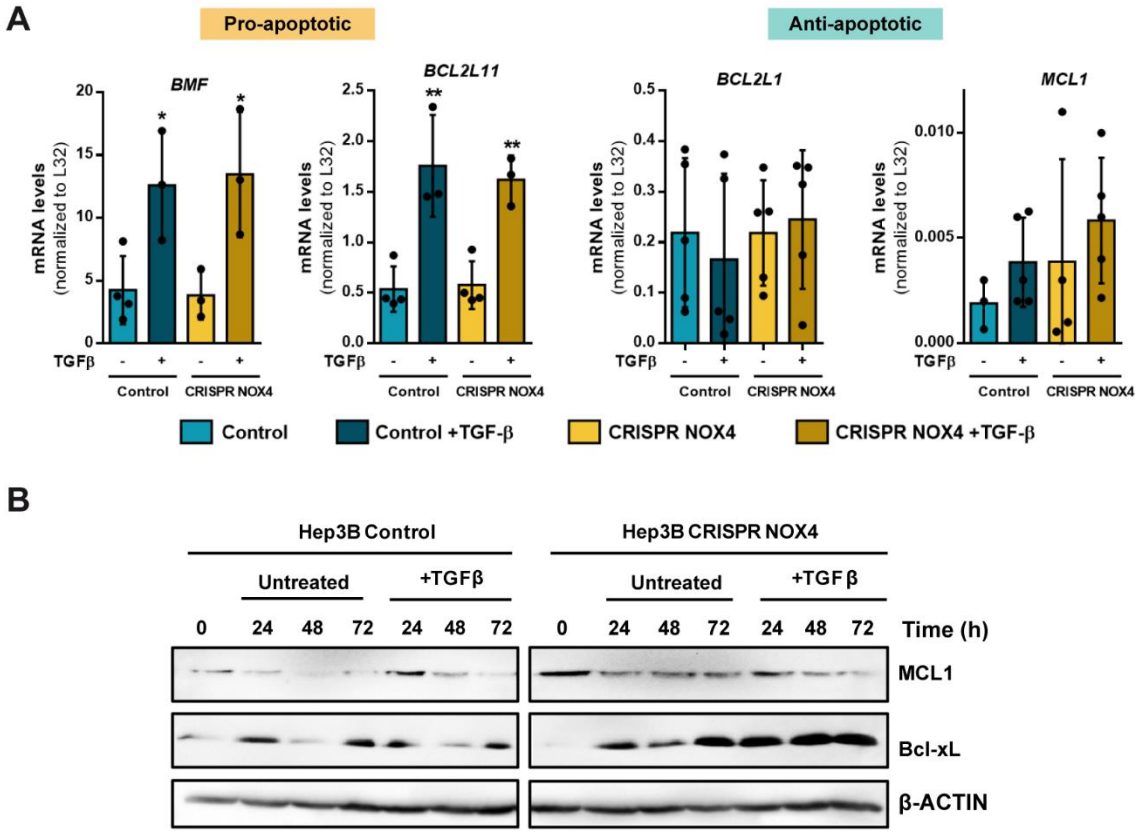

Figure 11. Role of NOX4 on TGF-β-induced apoptosis. Analysis made in Hep3B (Control and CRISPR NOX4) cells. **A** Proapoptotic (*BMF* and *BCL2L11*) and antiapoptotic (*BCL2L1* and *MCL1*) mRNA expression analysed by RT-qPCR, normalized to housekeeping gene *L32*, after TGF-β treatment at 48 h. Data are mean ± SD (n = 3–6). **B** MCL1 and Bcl-xL protein levels analysed by western blot after TGF-β treatment at 24, 48 and 72 h. β-Actin was used as loading control. Representative experiment is shown. *p<0.05 **p<0.01.

Nevertheless, protein level analysis by western blot revealed that, whereas MCL1 did not show any regulation, Bcl-xL levels were higher at basal conditions and increased after TGF-

β treatment, in Hep3B CRISPR NOX4 cells when compared to Hep3B Control cells (**Figure 11B**).

Overall, these results confirm that stable silencing of NOX4 regulates TGF-β-induced apoptosis, by means of post-transcriptional regulation of anti-apoptotic gene Bcl-xL, rather than by transcriptional regulation of pro-apoptotic genes.

3. NOX4-TGF-beta synergy in HCC patients

Taking into account the role of NOX4 in mediating tumour suppressor actions of TGF-β, we wondered whether this *in vitro* observation could have *in vivo* relevance. Surgical frozen samples from tumoral tissue obtained from a cohort of 124 patients were obtained by surgical procedures (resection or transplantation) at the HUB in collaboration with Dr. Emilo Ramos and Dr. Teresa Serrano. Their characteristics are summarised in **Table I**.

In **Figure 12**, the distribution of the patients regarding the expression of *NOX4* and *TGFB1* can be seen. The median value was defined in this analysis and "high" or "low" expression were determined depending on if the data were above or below it, respectively.

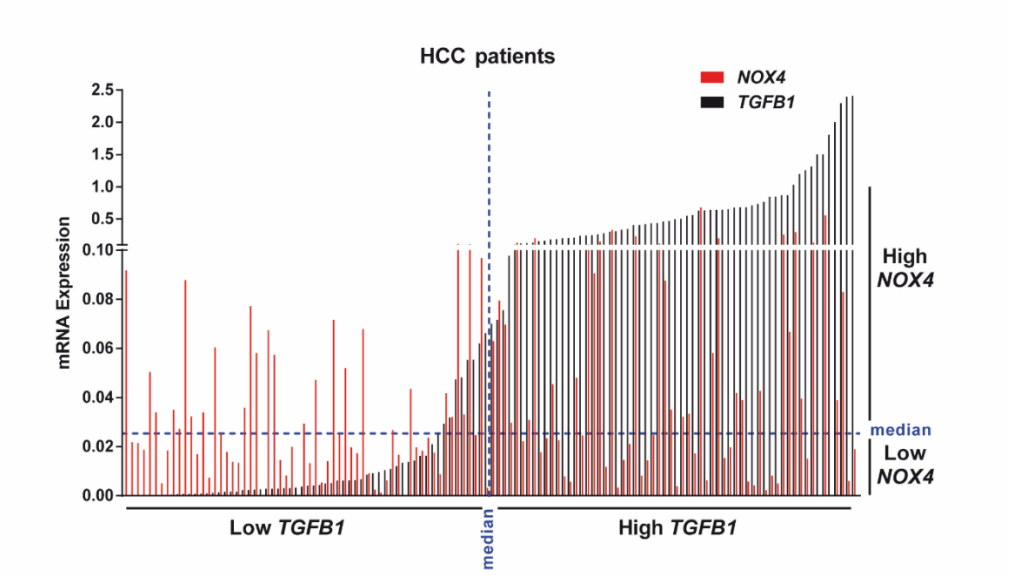

Figure 12. Expression of *NOX4* and *TGFB1* HCC patients. HCC patients n = 124 from HUB. Distribution of the patients according to the expression of *TGFB1* (black) and *NOX4* (red).

Considering the patient data, *NOX4* had a positive correlation with *TGFB1* expression (**Figure 13A**), which was statistically significant. Unexpectedly, when the Overall Survival (OS) was analysed, the patients that had high *NOX4* and high *TGFB1* expression, showed the worst prognosis (**Figure 13B**). This result was contrary to our initial hypothesis, which was that NOX4 could be mediating TGF-β tumour suppressor actions.

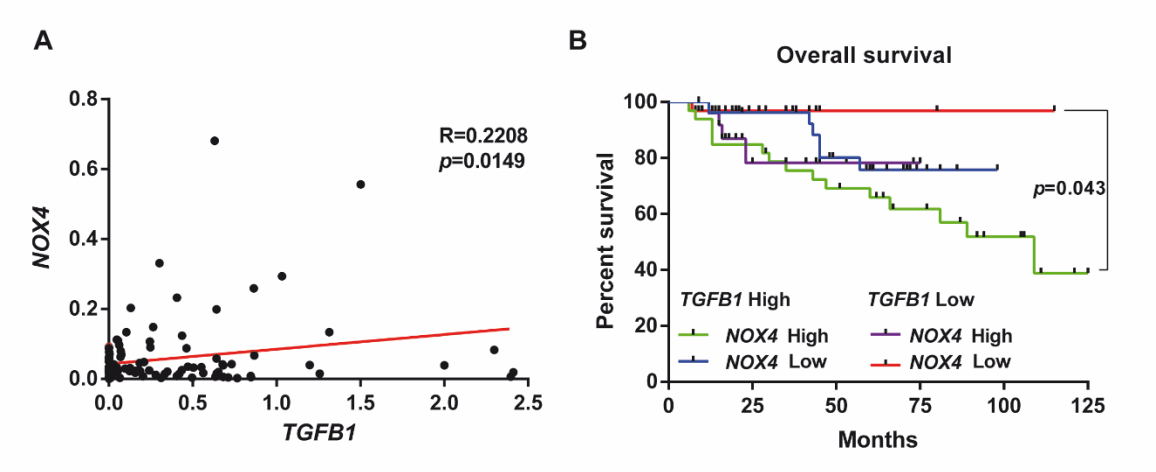

Figure 13. Impact of the expression of *NOX4* and *TGFB1* on different parameters in HCC patients. A Pearson correlation analysis between *NOX4* and *TGFB1* gene expression in 120 patients for which we had data of survival. **B** Kaplan-Meier curve for overall survival percentage when *TGFB1* and *NOX4* expression are high/low. $TGFB1^{high}/NOX4^{high}$ (green: 33 patients); $TGFB1^{high}/NOX4^{low}$ (blue: 27 patients); $TGFB1^{low}/NOX4^{high}$ (purple, 28 patients); $TGFB1^{high}/NOX4^{high}$ (red, 32 patients).

To further deepen into this and better elucidate the OS when *NOX4* expression is high or low, we moved to the TCGA public database (*see section 11.2*). As shown in **Figure 14A**, $NOX4^{high}$ in patients with high expression of TGF-β ligands lead to a worse OS compared to those with low TGF-β ligands expression, particularly in *TGFB2*'s case. Similar tendency was found when doing the same analysis with the high expression of TGF-β receptors, where $TGFBR1^{high}$ showed the most difference (**Figure 14B**). Remarkably, the tendency or differences were not observed when expression of TGF-β ligands or receptors was low.

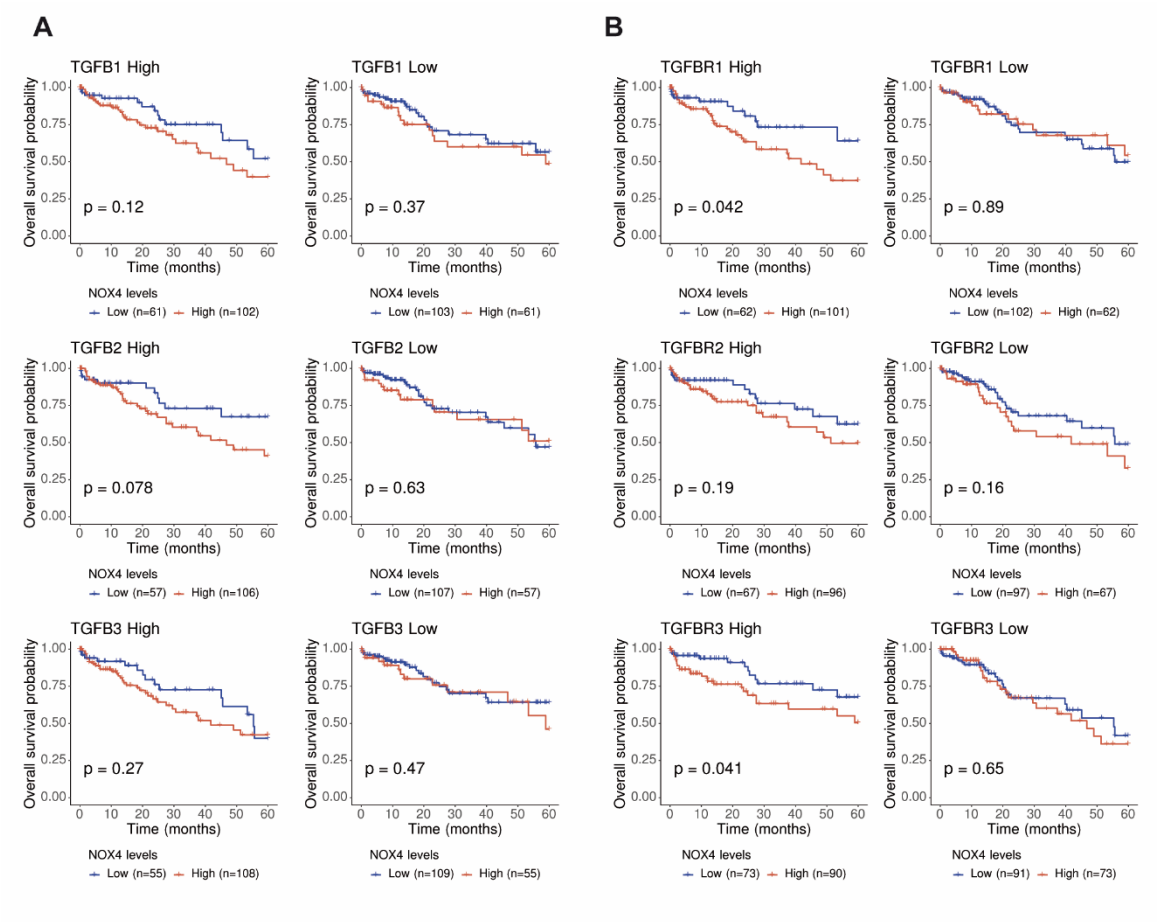

Figure 14. Kaplan-Meier curve for overall survival probability for *NOX4*- low versus *NOX4*-high HCC patients, stratified by TGF-β ligands and receptors expression levels. Data from TCGA-LIHC public data base (n=327). **A** TGF-β ligands: OS when *TGFB1*, *TGFB2* or *TGFB3* are high (**left**) or low (**right**). **B** TGF-β receptors: OS when *TGFBR1*, *TGFBR2* or *TGFBR3* are high (**left**) or low (**right**). Genes are categorized using the median, and p-values are derived from a log-rank test.

Moreover, TCGA database also showed a statistically significant positive correlation between *NOX4* and all the TGF-β ligands (*TGFB1, TGFB2, TGFB3*) and with all TGF-β receptors except for *TGFBR3* (**Figure 15**).

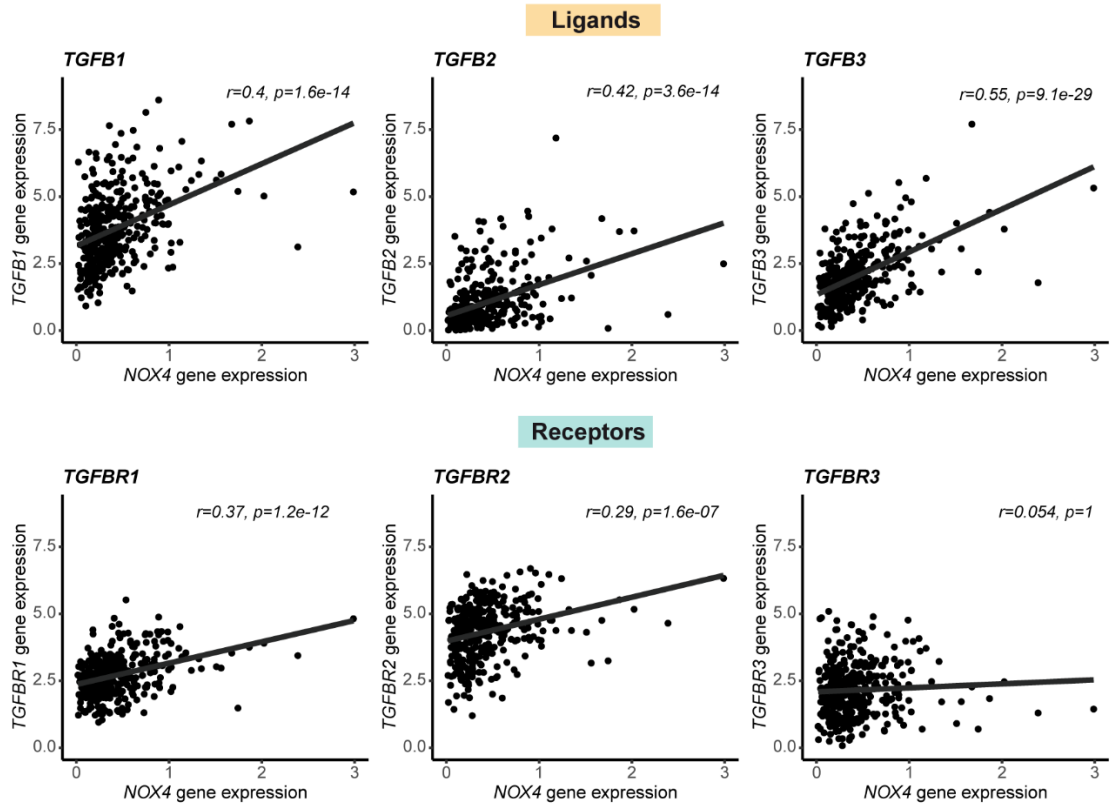

Figure 15. In silico analysis of the correlation of NOX4 expression and genes encoding TGF-β ligands and receptors. Data from TCGA-LIHC public data base (n=327). Pearson correlation analysis between *NOX4* gene expression and *TGFB1*, *TGFB2* or *TGFB3* (**top**) or *TGFBR1*, *TGFBR2* or *TGFBR3* (**bottom**).

Considering the correlation with most of the ligands and receptors of TGF-β signalling pathway, we also analysed the correspondence with a TGF-β gene signature. In **Table XVIII**, the genes that conform this TGF-β signature extracted from the Hallmarks of Cancer can be checked (*see section 11.2*). A positive correlation between the expression of *NOX4* and this signature was found, both with all HCC samples and also when restricting to samples with low stroma, pointing to a role of *NOX4* expression in tumour cells specifically (**Figure 16A**). Following a similar tendency to the previous results, the Kaplan-Meier curve for OS probability when the TGF-β signalling Hallmarks of Cancer signature is elevated showed a lower survival in $NOX4^{high}$ patients, in all and low stroma samples (**Figure 16B**).

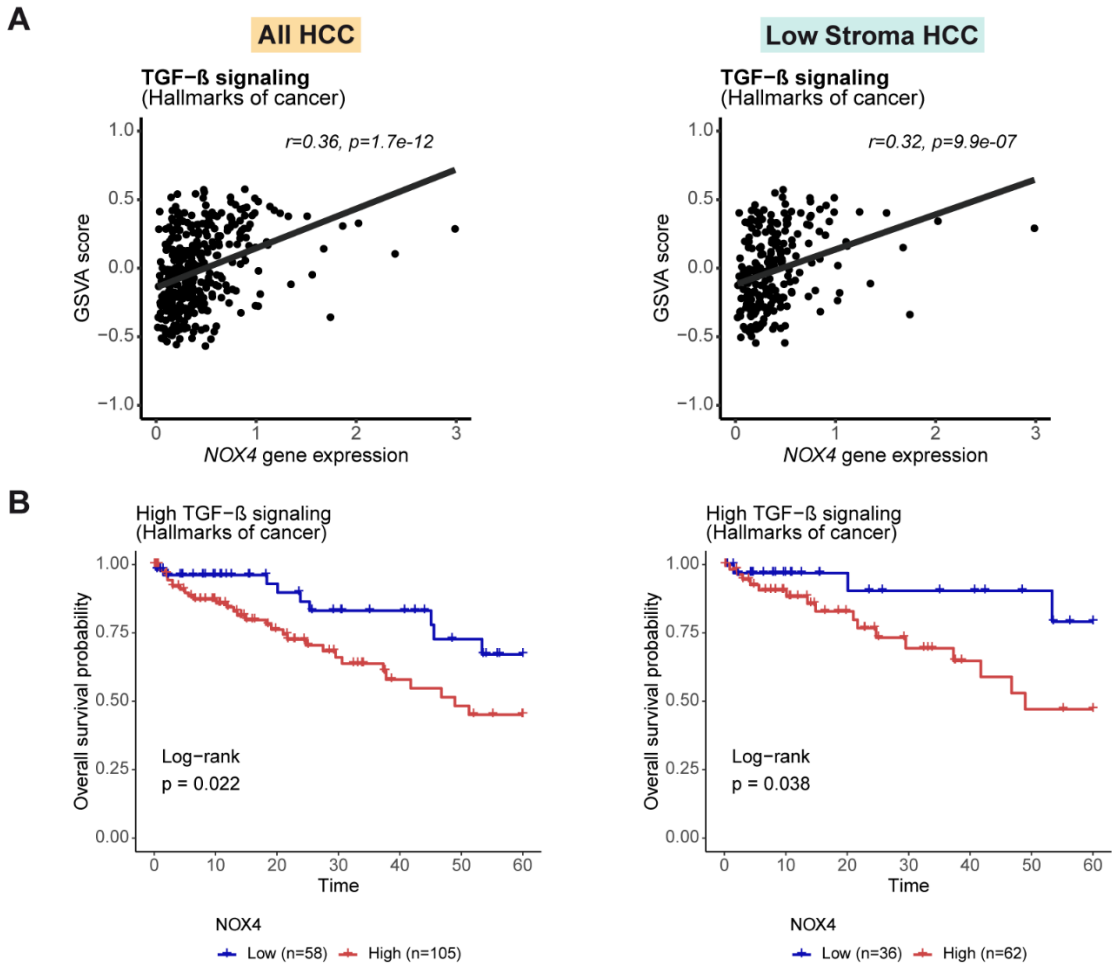

Figure 16. In silico analysis of the correlation of *NOX4* expression and a TGF-β-signalling gene signature (Hallmarks of Cancer) (see Table X). Data from TCGA-LIHC public data base (n=327). **A** Pearson correlation analysis between TGF-β signalling (quantified using Gene Set Variation Analysis (GSVA) score) and *NOX4* gene expression. Analysis done with all the HCC samples (**left**) or those with low stromal content (**right**). **B** Kaplan-Meier curve for overall survival probability for *NOX4*-low (blue) versus *NOX4*-high (red) patients when "TGF-β-signalling Hallmarks of Cancer" gene signature is high (above the median GSVA score). NOX4 is categorized using the median, and log-rank test is used to assess statistical differences. Analysis done with all the HCC samples (**left**) or those with low stromal content (**right**).

The data gathered in our cohort of HUB patients includes the size of the resected tumour. Interestingly, the percentage of tumours that were bigger than 5cm was slightly higher in those patients with a $NOX4^{low}/TGFB1^{high}$ expression, correlating with our *in vitro* results that say that NOX4 is mediating the TGF-β-induced growth inhibition (**Figure 17A**). However, the histological grade of the patients was a bit more advanced in the $NOX4^{high}$ samples (**Figure**

17B). Grade IV is infrequent because the patient cohort comes from surgical procedures, which are often just practiced in those patients in early stages (Table I).

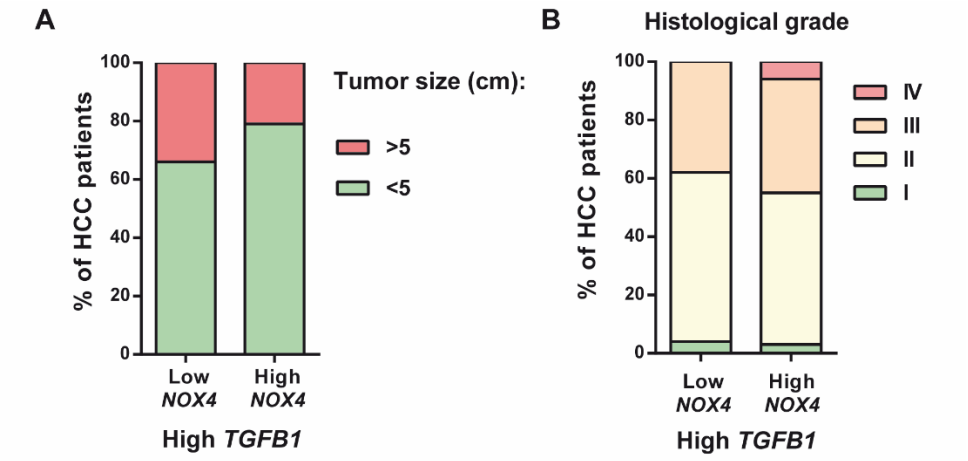

Figure 17. Impact of the expression of *NOX4* and *TGFB1* on different parameters in HCC patients. HCC patients n = 124 from HUB. **A** Percentage of HCC patients that have a tumour size bigger or smaller than 5 cm when *TGFB1* expression is high, depending on their *NOX4* expression. **B** Percentage of HCC patients in each histological grade (I-IV) when *TGFB1* expression is high, depending on their *NOX4* expression.

Finally, when analysing the relapse of those patients that are currently alive, it was clear that there is a higher proportion of relapse-free survival patients in $NOX4^{low}/TGFB1^{high}$ group (Figure 18A). On the contrary, etiologically, there were no differences found regarding a viral infection, alcohol, or NASH as a pathological cause (Figure 18B). Also, despite a slight tendency from the $NOX4^{high}/TGFB1^{high}$ patients to present mild fibrosis, no changes were observed in terms of cirrhosis (Figure 18C).

Altogether, these results would indicate that contrary to expectations regarding the strong role of TGF-β/NOX4 in mediating inhibition of growth and induction of apoptosis in liver tumour cells, the activation of both TGF-β and NOX4 pathways would reflect higher tumour progression.

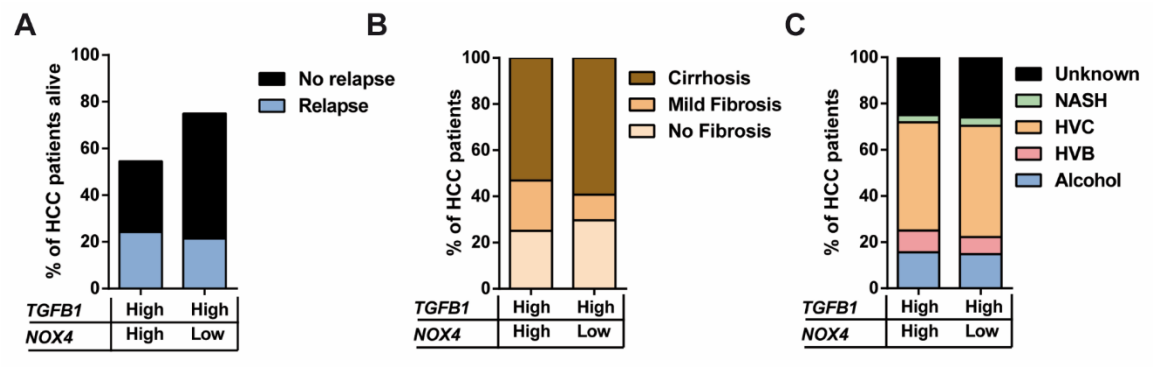

Figure 18. Impact of the expression of *NOX4* on relapse, fibrosis, and aetiology in HCC patients with high expression of *TGFB1*. Analysis performed in alive patients at the time of analysis.0 **A** Percentage of patients that suffered relapse versus those that did not. **B** Percentage of HCC patients with different aetiologies: Alcohol, HVB, HVC, NASH or Unknown origin. **C** Percentage of HCC patients presenting fibrosis, mild fibrosis or cirrhosis.

4. NOX4 role in TGF-beta protumorigenic actions

Even though our first hypothesis and previous knowledge was that NOX4 was playing a role in mediating the antitumorigenic actions of TGF-β, these last results observed in HCC patients made us take into consideration another potential role for NOX4. In this case, it could be contributing to tumour progression in parallel, thus holding a dual role as a TGF-β mediator.

4.1 In terms of cell migration

One of the key points in tumour progression is the metastatic capacity that its cells present. Therefore, the next point assessed was the invasive ability of HCC cells. Hep3B cell line was chosen to analyse the potential role of NOX4 in TGF-β-mediated migration.

To analyse the migratory capacity of Hep3B cells Control or CRISPR NOX4 in response to TGF-β, the xCELLigence real-time monitoring was performed (*see section 6.1*). A significant effect of TGF-β was seen in Control cells, where TGF-β increases significantly their migration. However, although Hep3B CRISPR NOX4 cells showed a higher migratory capacity compared to Control ones, they did not respond to TGF-β (**Figure 19**).

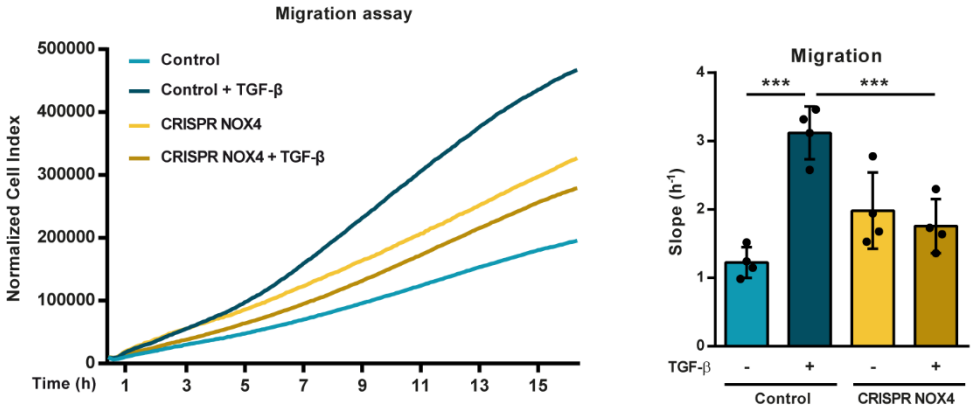

Figure 19. Role of NOX4 on TGF-β-induced cell migration and Epithelial-Mesenchymal Transition. Analysis made in Hep3B (Control and CRISPR NOX4) cells. Cell migration after TGF-β treatment, real-time monitored using xCELLigence system. Results expressed as Normalized Cell Index (**left**) or slope (h^{-1}) (**right**) of the first 16 h. Data are mean ± SD (n = 3–4). ***p<0.001

To further analyse this, an invasive growth assay was performed. First, 3D spheroids of Hep3B Control and CRISPR NOX4 with or without TGF-β were created (*see section 3.2*). Then, these spheroids were embedded in a mix of collagen gel, to monitor their ability to proliferate and invade the matrix. As observed in **Figure 20A**, untreated Hep3B Control cells spheroids were bigger in size. However, when treated with TGF-β, even though the spheroid was significantly smaller, their invasive front showed spreading of cells invading the collagen in Hep3B Control. In the case of Hep3B CRISPR NOX4 cells, this was not observed. On the contrary, untreated NOX4 silenced cells have increased proliferation and invasion, and this is inhibited when treated with TGF-β.

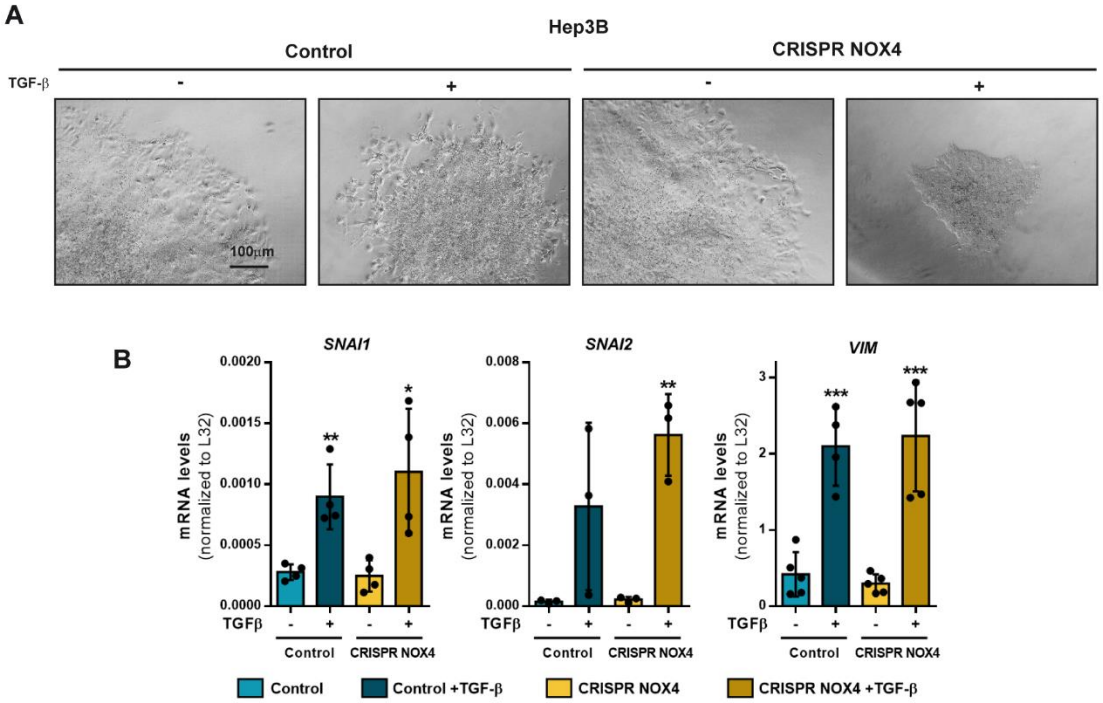

Figure 20. Role of NOX4 on TGF-β-induced cell migration and Epithelial-Mesenchymal Transition. A Representative images of spheroids from cells either untreated or treated with TGF-β, embedded in a collagen I matrix for 96h. Scale bar, 100µm. **B** *SNAI1*, *SNAI2* and *VIM* mRNA expression analysed by RT-qPCR, normalized to housekeeping gene L32, after 48h TGF-β treatment. Data are Mean ± SD (n = 3–4). *p<0.05, **p<0.01, ***p<0.001

4.2 In terms of EMT transcriptional program

It is known that Hep3B respond to TGF-β by undergoing EMT[224], and so NOX4 role in it was analysed. To do so, we analysed the RNA expression of several genes of interest. We observed (**Figure 20B**) that neither *SNAI1* (SNAIL 1), *SNAI2* (SNAIL 2 or SLUG) nor *VIM* (Vimentin) are affected by the silencing of NOX4 in terms of TGF-β response. Furthermore, E-cadherin expression and localization was checked by immunofluorescence (**Figure 21**) as a target of SNAIL. In both cases, its expression was lost when treated with TGF-β, regardless of the presence of NOX4.

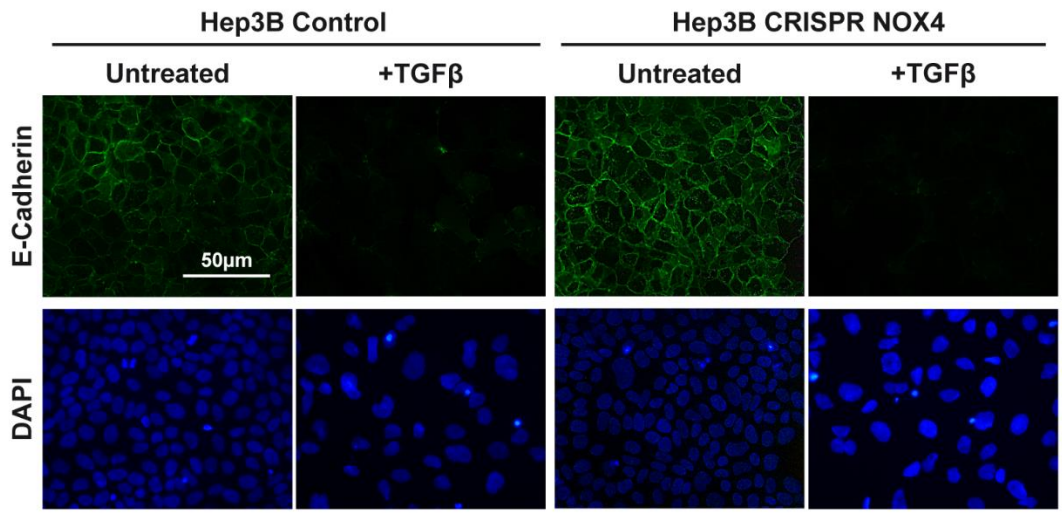

Figure 21. Role of NOX4 on TGF-β-induced cell migration and Epithelial-Mesenchymal Transition Immunofluorescence of E-Cadherin (green) and DAPI (blue) for nuclei staining after 48h TGF-β treatment. Representative images shown. Scale bar, 50μm.

Overall, these results indicated that NOX4 was not playing a role in regulating EMT transcriptional program in Hep3B cells in response to TGF-β.

4.3 In terms of cytoskeleton remodelling

To migrate and invade, cells also require cytoskeleton remodelling and replacement of focal adhesions. Therefore, another mechanism to increase the migratory ability of cells is to regulate those. Since we found differences in migration but not in the regulation of the EMT program, we looked into cytoskeleton.

To analyse the cytoskeleton, an immunofluorescence of Hep3B Control and CRISPR NOX4 with or without TGF-β treatment was performed (**Figure 22**). Phalloidin stains F-Actin (red) and Vinculin (green) was marked to observe the focal adhesions. Significant differences can be observed in untreated conditions, as actin filaments in Control cells are disposed pericellularly, whilst this is lost in CRISPR NOX4 cells. TGF-β treatment in Control cells notably increased the stress fibres stained by Phalloidin and, importantly, also increased the number and size of the focal adhesions, stained by vinculin. This consequence was also seen in CRISPR NOX4 cells treated with TGF-β, although it was clearly not so noticeable.

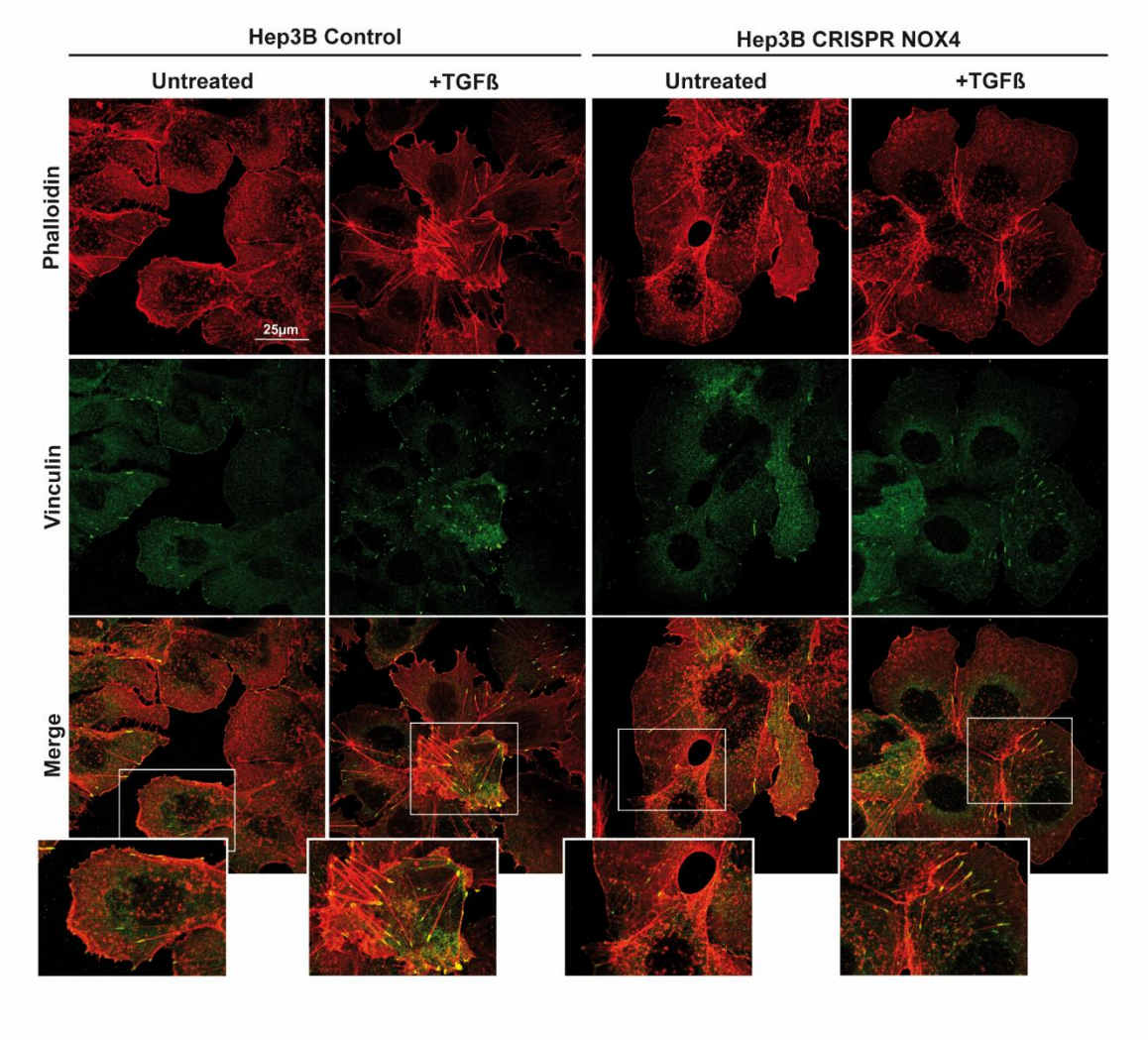

Figure 22. Role of NOX4 on TGF-β-induced cytoskeleton remodelling. Analysis made in Hep3B (Control and CRISPR NOX4) cells. Immunofluorescence of Phalloidin (red) and Vinculin (green) after 48h TGF-β treatment. Representative images shown. Scale bar, 25µm.

It is described that for cells to have a high migratory capacity, the focal adhesions must be mature[225]. This refers to the size, they need to be big; to the localization within the cell, they are required to be in the centre not the periphery; and the co-localization with the stress fibres. Observing this last figure, it is clearly seen how all these parameters are accomplished in the case of TGF-β-treated Hep3B Control cells (**Figure 22**). Overall, NOX4 seems to be needed for an efficient TGF-β cytoskeleton remodelling with the respective focal adhesions.

In other models, NOX4 had been suggested to be localized next to focal adhesions[124], which suggests an explanation to the effects by NOX4 explained in the previous section. For this reason, we decided to further deepen into the NOX4 subcellular localization, also when treated with TGF-β, which is, as explained in *section 3.3.2*, a controversial topic among literature. Therefore, immunofluorescence analysis of NOX4 and focal adhesions was done in Hep3B Control cells, analysed by Vinculin staining (**Figure 23**). This approach revealed some co-localization in only some few points. In fact, NOX4 was mainly located in intracellular vesicles (**Figure 23**) in both untreated and TGF-β-treated cells.

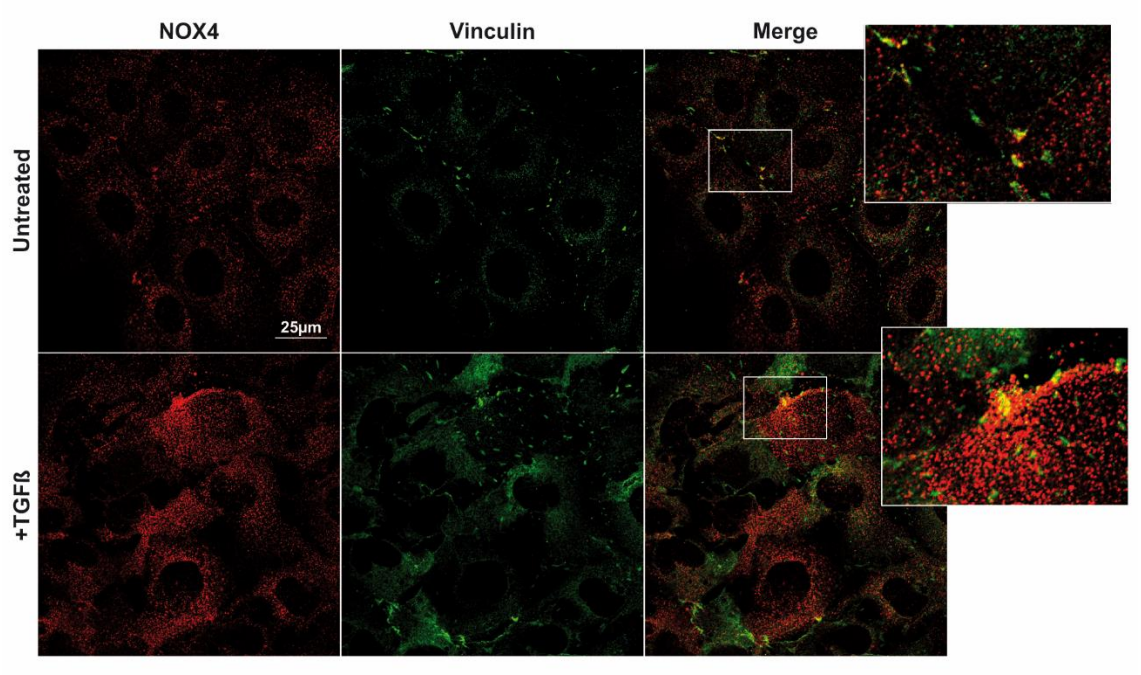

Figure 23. NOX4 protein localization in focal adhesions. Analysis made in Hep3B Control cells. Immunofluorescence of NOX4 (red) and Vinculin (green) in cells either untreated or treated during 48h with TGF-β. Representative images are shown. Scale bar, 25µm.

Next, we also performed a subcellular fractionation of untreated PLC/PRF/5 cells (*see section 9.3*), in order to observe the NOX4 protein levels in every cellular fraction: Total, cytoplasm, membrane, soluble nucleus and chromatin. Moreover, as some reports describe NOX4 localization in specific organelles, we also analysed specific fractions for ER and mitochondria. Analysis by western blot revealed that the majority of the NOX4 protein is in the cytosolic fraction (**Figure 24A**), which correlated with high levels in the endoplasmic

reticulum fraction (**Figure 24B**). Nevertheless, immunofluorescence and western blot results seem to also indicate that part of NOX4 expression may be in the nucleus (**Figure 23**) or even in the mitochondria (**Figure 24C**).

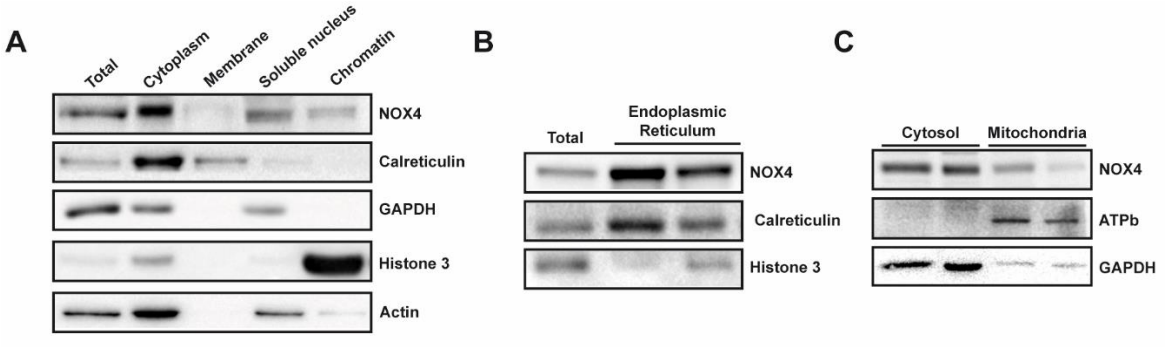

Figure 24. NOX4 protein localization in different cellular compartments. Analysis made in PLC/PRF/5 cells. **A** NOX4 protein levels analyzed by western blot in different subcellular fractions of untreated PLC/PRF/5 cells, extracted as described in the Material and Methods section. **B** Similar analysis in total or Endoplasmic Reticulum fractions and **C** in Cytosol and Mitochondria fractions. Marker proteins to follow fractionation were: Calreticulin for endoplasmic reticulum (ER), GAPDH for cytosolic compartment, ATPb for mitochondria and Histone 3 for chromatin. Images representative of at least 3 independent experiments.

As a tentative to look for molecular mechanisms to explain the regulation of TGF-β-induced cytoskeleton remodelling, the expression levels of RAC/RHO family genes were assessed. It is known that TGF-β induces the expression of *RHOA*, *RHOC*, *RAC1* and *CDC42*, all members of the named family, upregulation that can be seen in **Figure 25**. However, no differences between Control and CRISPR NOX4 cells were found.

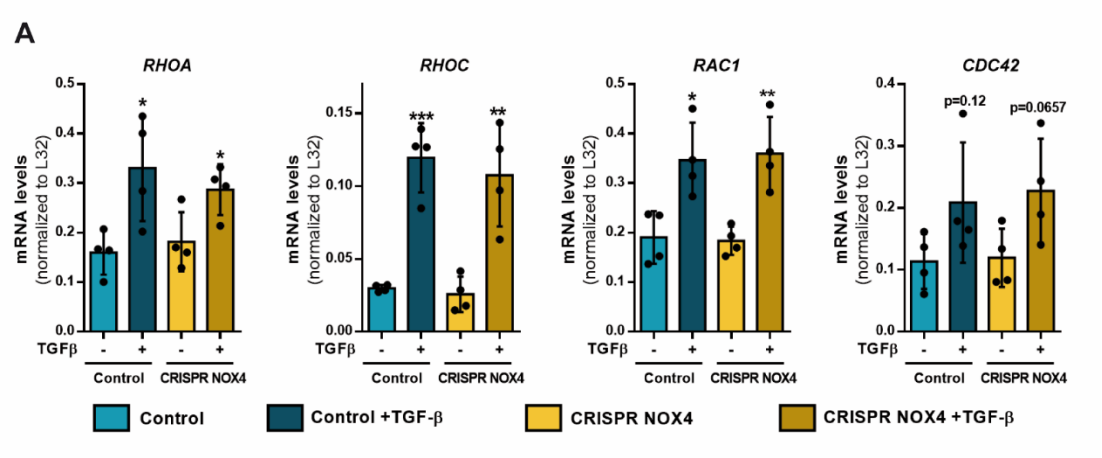

Figure 25. NOX4 silencing in HCC Hep3B cells do not affect the response to 48h TGF-β treatment in terms of RhoGTPases family gene expression. *RHOA*, *RHOC*, *RAC1* and *CDC42* mRNA expression analyzed by RT-qPCR, normalized to housekeeping gene *L32*, after TGF-β treatment at 48 hours. Data are Mean ± SD (n=4). *p<0.05 **p<0.01, ***p<0.001.

Overall, although these genes have been described as one of the possible regulators of cytoskeleton and focal adhesions, no differences depending on *NOX4* expression were found. Looking for additional molecular mechanisms, we found that Hic-5 is a protein previously proposed as a TGF-β mediator of adhesion in Vascular Smooth Muscle Cells (VSMC)[83]. Indeed, immunofluorescence of Hic-5 (**Figure 26A**) showed significant differences. On one hand, not only did the Hic-5 staining from Control cells increase with TGF-β treatment but also it localized in focal adhesion-like regions. On the other hand, Hep3B CRISPR NOX4 cells showed low levels of Hic-5, which did not increase upon TGF-β treatment.

Additionally, Hic-5 subcellular localization, in the focal adhesions, requires the chaperon protein Hsp27, known to be a transcriptional target gene mediated by NOX4. Therefore, we thought that a difference in this protein level could explain the difference observed in Hic5 by immunofluorescence. Precisely, Hsp27 analysis by western blot revealed an increase after TGF-β treatment, which was clearly attenuated in CRISPR NOX4 cells (**Figure 26B**). These findings indicate that NOX4 is essential for the TGF-β-mediated control of cytoskeleton dynamics and focal adhesions. Furthermore, NOX4 is required for the TGF-β-induced elevation of the chaperone Hsp27 and Hic-5, as well as the accurate localization of Hic-5 within focal adhesions.

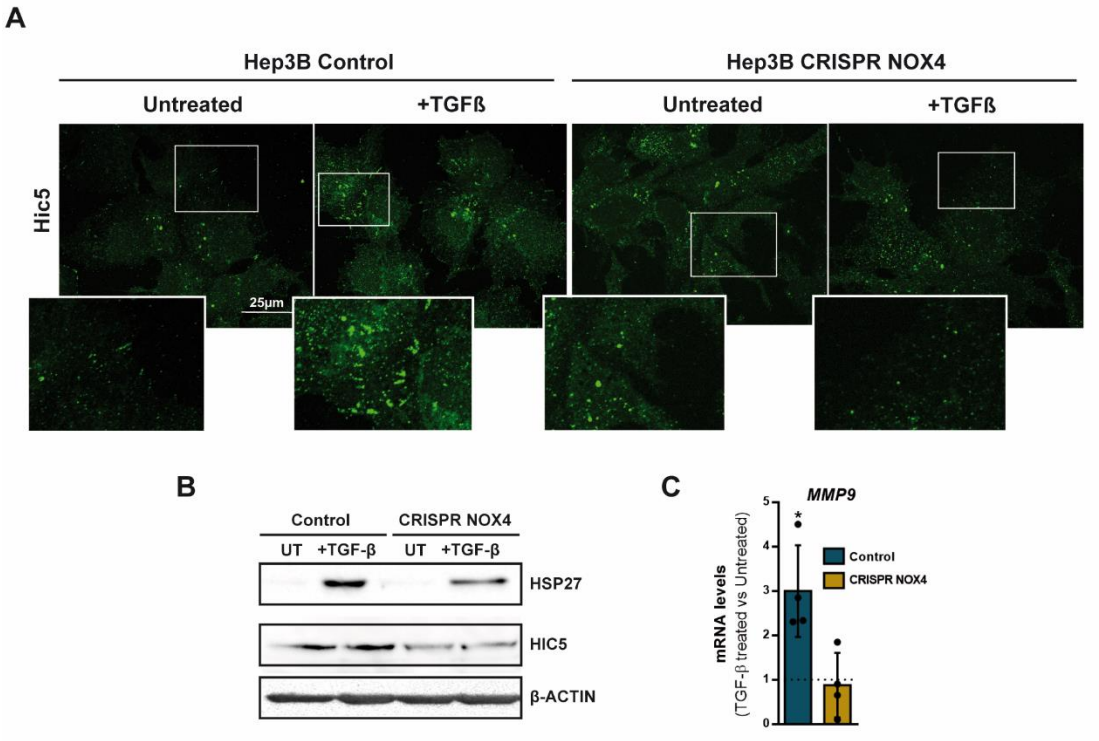

Figure 26. Role of NOX4 on TGF-β-induced cytoskeleton remodeling molecular mechanisms. Analysis made in Hep3B (Control and CRISPR NOX4) cells. **A** Immunofluorescence of Hic-5 (green) after 48h TGF-β treatment. Representative images are shown. Scale bar, 25 µm. **B** Hsp27 and Hic-5 protein levels analyzed by western blot after 48 h of TGF- β treatment. β-Actin was used as loading control **C** *MMP9* mRNA expression analyzed by RT-qPCR, normalized to housekeeping gene *L32*, after 48h TGF-β treatment and represented as fold induction (TGF-β-treated versus untreated cells). Mean ± SD (n = 4–6). *p<0.05.

Finally, *MMP9* was shown to be significantly upregulated in Control cells upon TGF-β treatment, but not in CRISPR NOX4 (**Figure 26C**), as a regulator of actin polymerization and cell migration[226,227]. Regarding TCGA data, MMP9 expression in TGFB1high patient cohort showed higher levels in NOX4high patients, compared to NOX4low ones. This difference could not be seen in the cohort where patients are TGFB1low (Figure 27), reinforcing the capacity of NOX4 to regulate MMP9 under TGF-β pathway. Analysis of TGFB1l1, gene name for Hic-5, revealed the same pattern; that is, the highest expression level in the patient cohort of TGFB1high – NOX4high. Moreover, the same study was performed on HCC samples that are classified as Low stroma ones. The results were quite similar to those from samples that contained stromal and tumoral cells (**Figure 27**), meaning that the differences are mainly due to tumour cells.

Collectively, these findings strongly suggest that NOX4 plays a crucial role in facilitating TGF-β-mediated enhancement of migration in HCC cells. This facilitation occurs via the modulation of cytoskeleton dynamics and focal adhesions, which aligns with alterations in the expression levels of key proteins such as Hsp27, Hic-5, and MMP9.

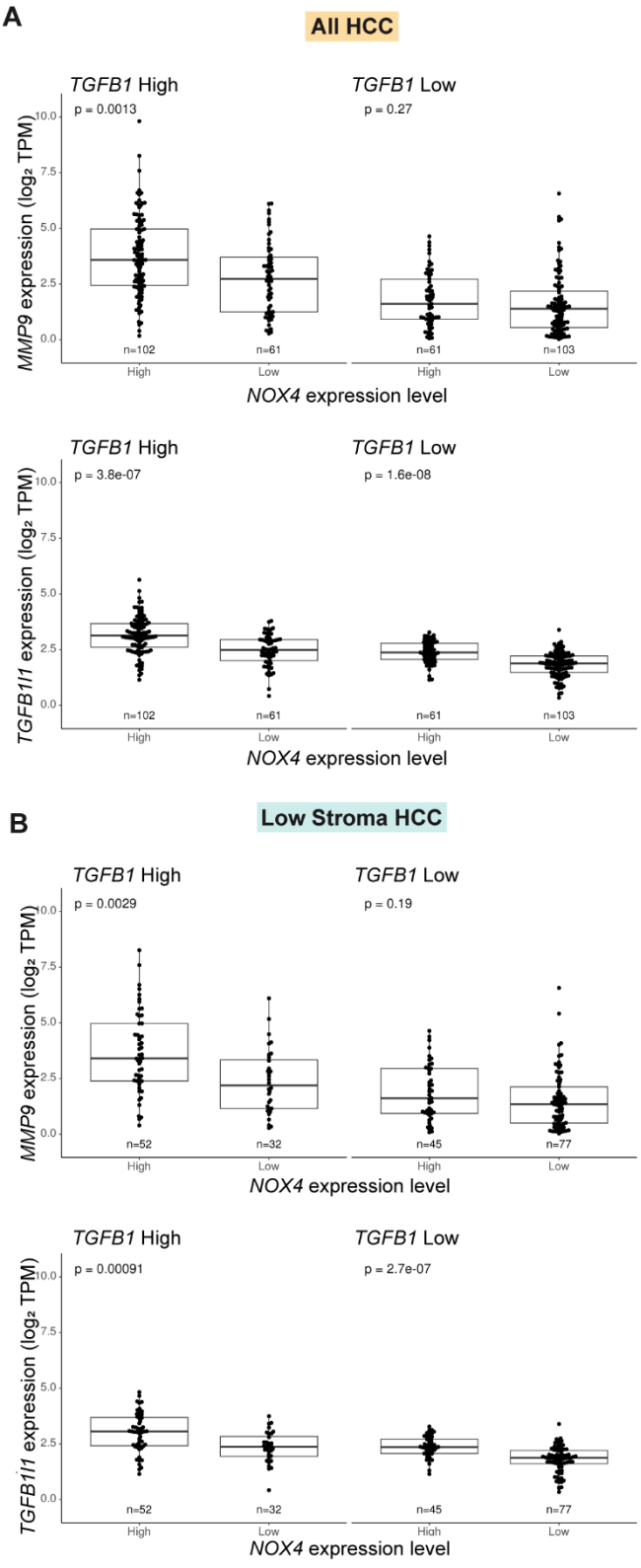

Figure 27. In silico analysis of the correlation of the expression of *NOX4* with *MMP9* and *TGFB1I1* genes in HCC patients. A) Boxplot of *MMP9* (**top**) or *TGFB1I1* (**bottom**) gene expression for *NOX4*-low versus *NOX4*-high patients when *TGFB1* expression is low or high. Analysis done with all the HCC samples. **B)** Boxplot of *MMP9* (**top**) or *TGFB1I1* (**bottom**) gene expression for *NOX4*-low versus *NOX4*-high patients when *TGFB1* expression is low or high. Analysis done with low stromal content samples. Data from TCGA-LIHC public data base (n=327). P-values from a Mann-Whitney U test, adjusted for multiple testing.

Dissecting the role of NOX4 - TGF-β in the interactome of HCC

5. Role of NOX4 on liver tumorigenic progression in the DEN-induced mice model

Aiming to analyse the role of NOX4 *in vivo*, an experiment was performed using WT and NOX4 -/- mice, which were exposed to PBS or DEN, and gathered after 11 months of treatment (*see section 2.1*). This approach allows us to study liver tumour progressions and tumour characteristics when NOX4 is present, or knocked out, in all liver cells.

5.1 Macroscopic and microscopic analysis of the tumoral lesions

Previous results from the group had demonstrated in xenograft experiments that injecting NOX4-silenced cells in mice liver conferred an advantage in HCC initiation and progression in terms of tumour size[132]. As expected, DEN-treated mice after 11 months post-treatment, developed tumours (**Figure 28A**), both in WT and NOX4 -/- mice.

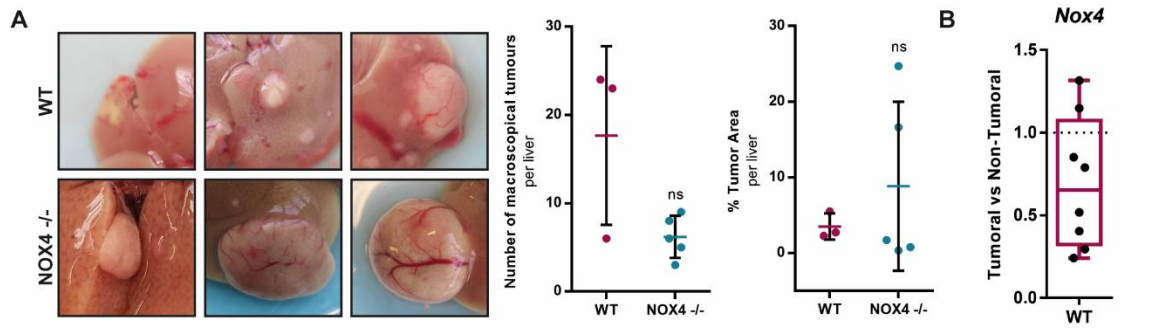

Figure 28. Characterization of the macroscopical tumours. A Macroscopical images of livers in mice at 11 months post-DEN treatment. **B** Quantification of the number and size of macroscopical tumours observed at 11 months post-DEN treatment. **C** *Nox4* mRNA expression in WT mice 11 months post-DEN treatment. Data are represented as ratio of tumour versus non-tumour.

Consequently, we started by analysing several macroscopic characteristics, such as tumour size, number of tumours…Although the number of macroscopical tumours was lower

(**Figure 28B**), their size was slightly bigger in NOX4 -/- tumours (**Figure 28B**). WT mice presented clearly small visible tumours (at least one), but most of them lower than 5mm of diameter; only one mouse presented two tumours of higher size, around 8mm each. The expression of Nox4 found in the tumoral area, when compared to the non-tumoral area, in WT mice correlated with previous results from the group that showed that under proliferative situations, Nox4 gene is downregulated (**Figure 28C**). From the five NOX4 -/- mice incorporated in the study, two of them showed a necrotic liver and apparent hepatomegaly with appearance of a spongy liver. In the other three mice, very large tumours were observed in two of the cases with a size of approximately 2 cm.

It is known that DEN-induced liver tumours are not a fibrogenic HCC model and, therefore, fibrosis does not appear prior to HCC initiation[228,229], as it is common in HCC patients, that come from cirrhosis. Hematoxilin-Eosin staining showed some macrovesicular and microvesicular steatosis, but no fibrotic bridges. Also, the non-tumoral parenchyma presented normal structure and architecture in most of the mice (**Figure 29A**). Assessment of the microscopical area of tumours showed no difference between WT and NOX4 -/- mice (**Figure 29B**).

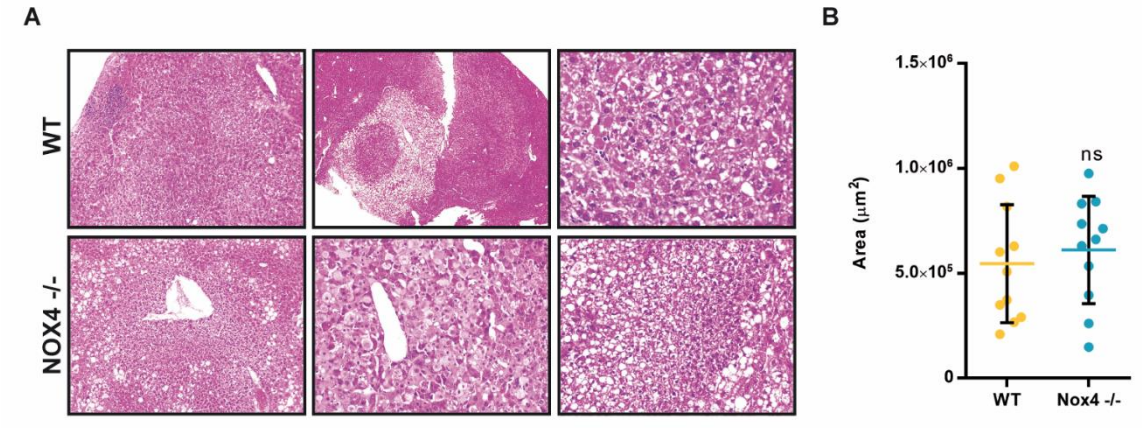

Figure 29. Characterization of the microscopical tumours. A Hematoxylin and Eosin (H&E) in liver tumours from WT and NOX4 -/- mice at 11 months post-DEN treatment. Representative images shown. **B** Quantification of the area of microscopical tumours observed at 11 months.

Considering that hepatocytes' proliferation is one of the tumour progression hallmarks, as in most cancer types, we further analysed the proliferative capacity of tumours in WT or NOX4 -/- mice. Corroborating the research group background, NOX4 -/- tumours showed almost statistical differences in terms of a higher cell proliferation, analysed as Ki67 staining (**Figure 30**). Overall, NOX4 -/- tumours showed a higher number of Ki67-positive cells per field (**Figure 30**), confirming the fact that their tumours were bigger in size.

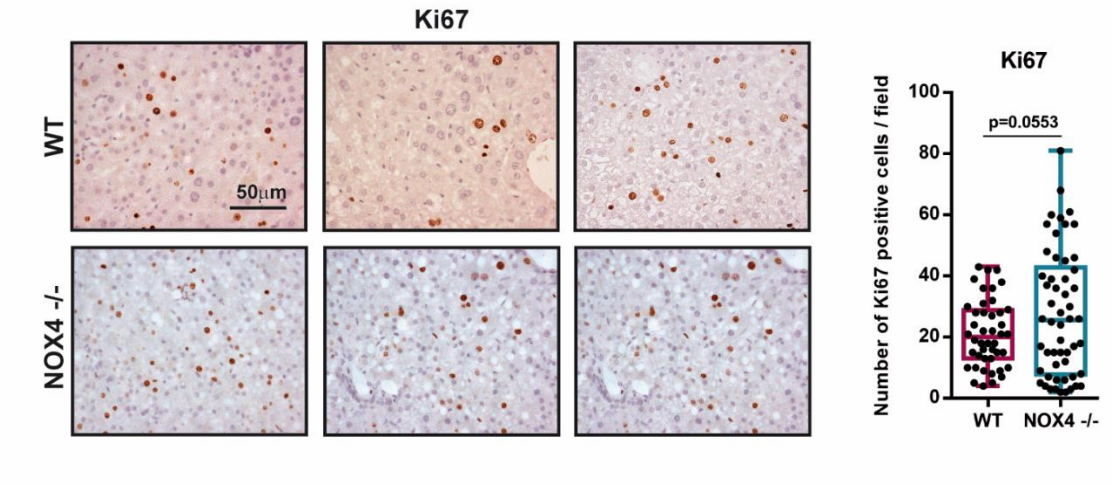

Figure 30. Characterization of the tumoral proliferation. Ki67 staining in liver tumours from WT and NOX4 -/- mice at 11 months post-DEN treatment. Representative images shown (**left**). Scale bar: 100µm. Quantification of Ki67-positive nuclei per field (**right**). Data is expressed as box plots with whiskers (min to max) (n=3).*p<0.05

5.2 NOX4 role in TGF-β gene signature *in vivo*

As we could not expect where we could start looking for the implications of NOX4 silencing in a model as complex as mice, we sent the samples for an RNA sequencing analysis (*see section 10.4*).

In a first Principal Component (PC) Analysis (**Figure 31A**) we can see that there is a good clustering among the different groups and conditions, except for two DEN NOX4 -/- mice. In fact, one of them is coincident with one of the mice that had a different phenotype in terms of H-E analysis. However, we decided to maintain all of the samples in the subsequent analysis, due to the shortage of number of animals. Further characterizing the analysis, we

could see that both PBS and Tumour conditions show differential gene expression (DEG) between WT or NOX4 -/- mice (**Figure 31B**), as represented in the Volcano plots.

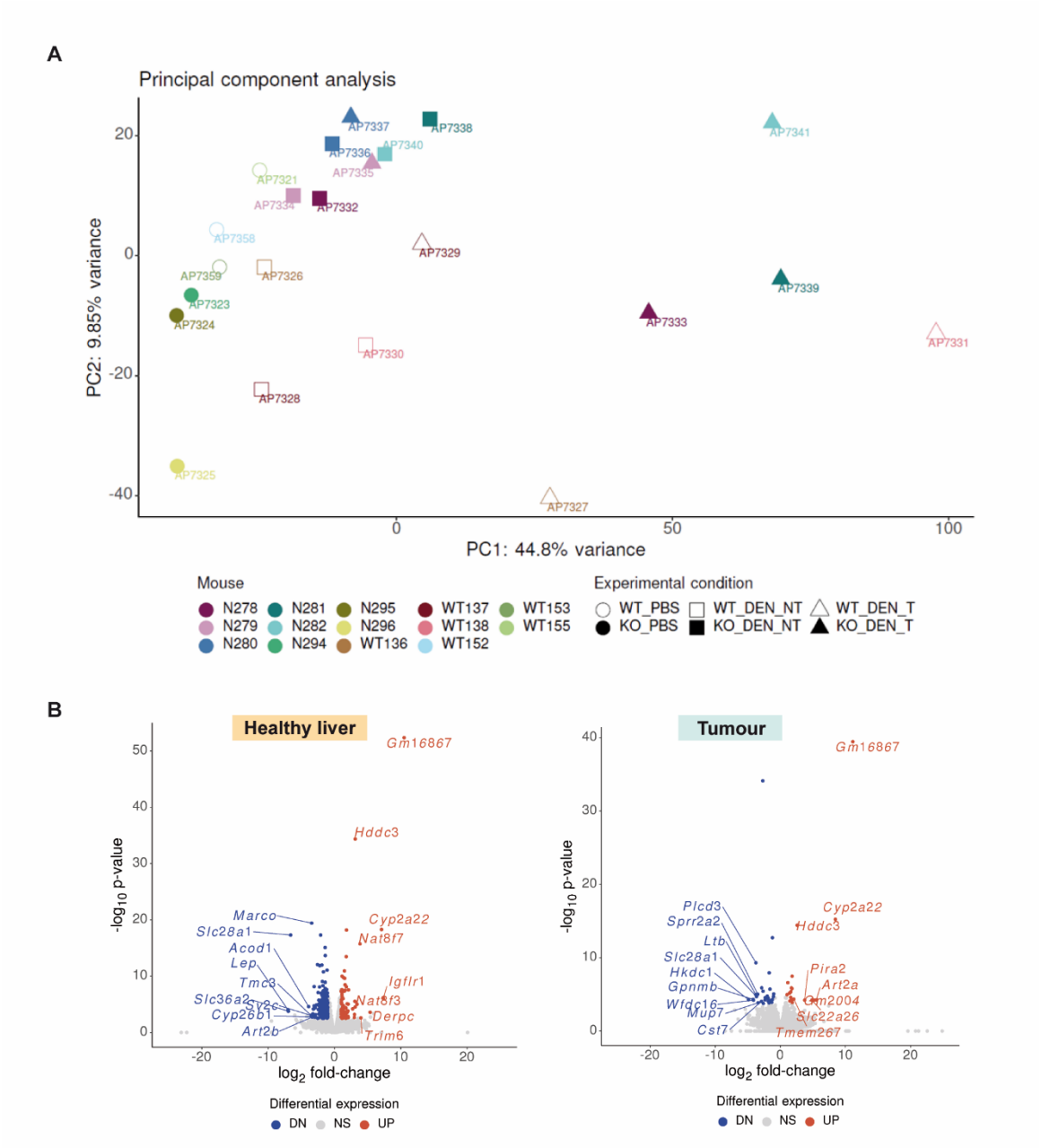

Figure 31. Preliminary data from RNAseq analysis in WT and NOX4 -/- mice at 11 months post DEN-treatment A Principal Component Analysis of the RNA sequencing samples. **B** Volcano plot of differentially expressed genes in WT compared to NOX4 -/- mice in PBS or Tumour conditions. Red = upregulated, blue=downregulated.

Interestingly, while we were studying the DEN-induced hepatocarcinogenesis, we also found several differential features between WT and NOX4 -/- mice at basal

levels (PBS), that is, in the healthy liver. This demonstrates the importance of NOX4 in several physiological pathways. Relative pathway activation was analysed in GSVA score. Indeed, NOX4 -/- livers showed a downregulated pathway for apoptosis and TGF-β signalling, corroborating the role of NOX4 in regulating these pathways (**Figure 32A**).

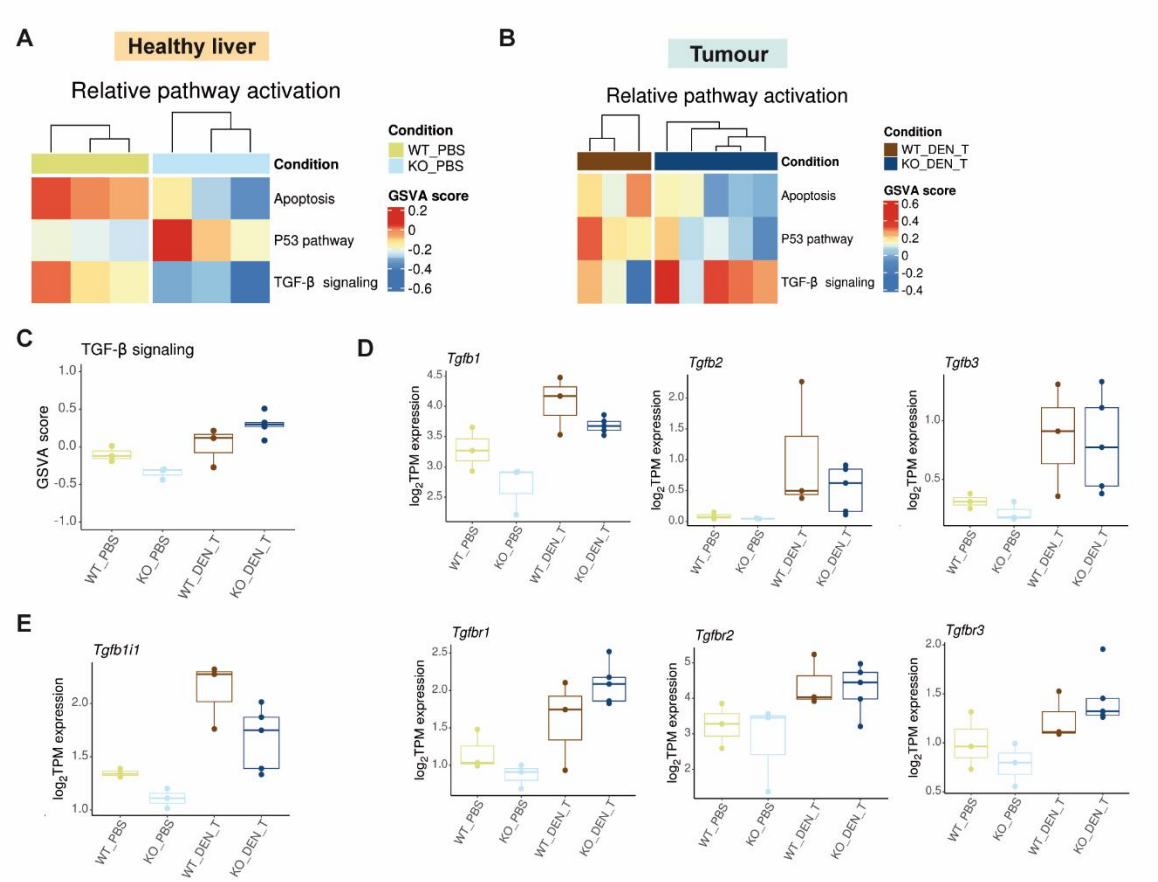

Figure 32. RNAseq analysis in WT and NOX4 -/- mice at 11 months post DEN-treatment. A-B Heatmaps of Relative expressions of Hallmark Pathway Enrichment Scores in WT compared to NOX4 -/- mice in PBS (**A**) or Tumour (**B**) conditions. Colour scale indicates the GVSA score with red representing high enrichment and blue representing low enrichment. **C** Boxplot representation of TGF-beta signalling Hallmark Pathway Enrichment Score in WT compared to NOX4 -/- mice. **D** Boxplot representation of Log2 TPM expression levels of TGF-β ligands (**top**) and receptors (**bottom**) genes in WT compared to NOX4 -/- mice. **E** Boxplot representation of Log2 TPM expression levels of *Tgfb1i1* gene in WT compared to NOX4 -/- mice.

On the other hand, the apoptosis pathway was still downregulated in NOX4 -/- mice under hepatocarcinogenesis, whereas TGF-β signalling was upregulated (**Figure 32B**). TGF-β

signalling pathway is also represented as a boxplot, to better observe the changes between conditions (**Figure 32C**). This result could be explained by the different expression of TGF-β ligands or receptors between samples. Therefore, expression of *TGFB1, TGFB2* and *TGFB3,* as ligands; and *TGFBR1, TGFBR2* and *TGFBR3*, as receptors, was analysed (**Figure 32D**). Even if there was a high dispersion among the same conditions, there was a slight tendency for the NOX4 -/- tumours to express higher levels of *TGFBR1*, which could explain the increase in TGF-β signalling. Finally, correlating with the previous part of my thesis, we checked the levels of *Tgfb1i1* (Hic-5), whose expression correlated with the *in vitro* results (**Figure 32E**).

5.3 Role of NOX4 in fibroblast activation

As NOX4 is known to have a role in activating HSC upon TGF-β treatment, we were interested in assessing the state of the fibroblasts in this model.

As explained in section 4.2.1, when liver myofibroblasts are activated, they produce ECM proteins. Therefore, initially, we started by analysing in RNAseq some specific genes related with fibroblast activation. Mainly, we found that NOX4-deficient mice had a downregulation of the expression of several Collagen genes, in the healthy liver (**Figure 33A**). Furthermore, when comparing WT and NOX4 -/- tumours collagen expression, lower levels were observed again (**Figure 33B**).

Apart from the differential gene expression, we also ought to check relative expression pathways from the M5 hallmarks database. Several pathways related to fibroblast activation and proliferation had a negative Normalized Enrichment Score (NES) in NOX4 -/- Tumours (**Figure 33C**), correlating with the previous analysis.

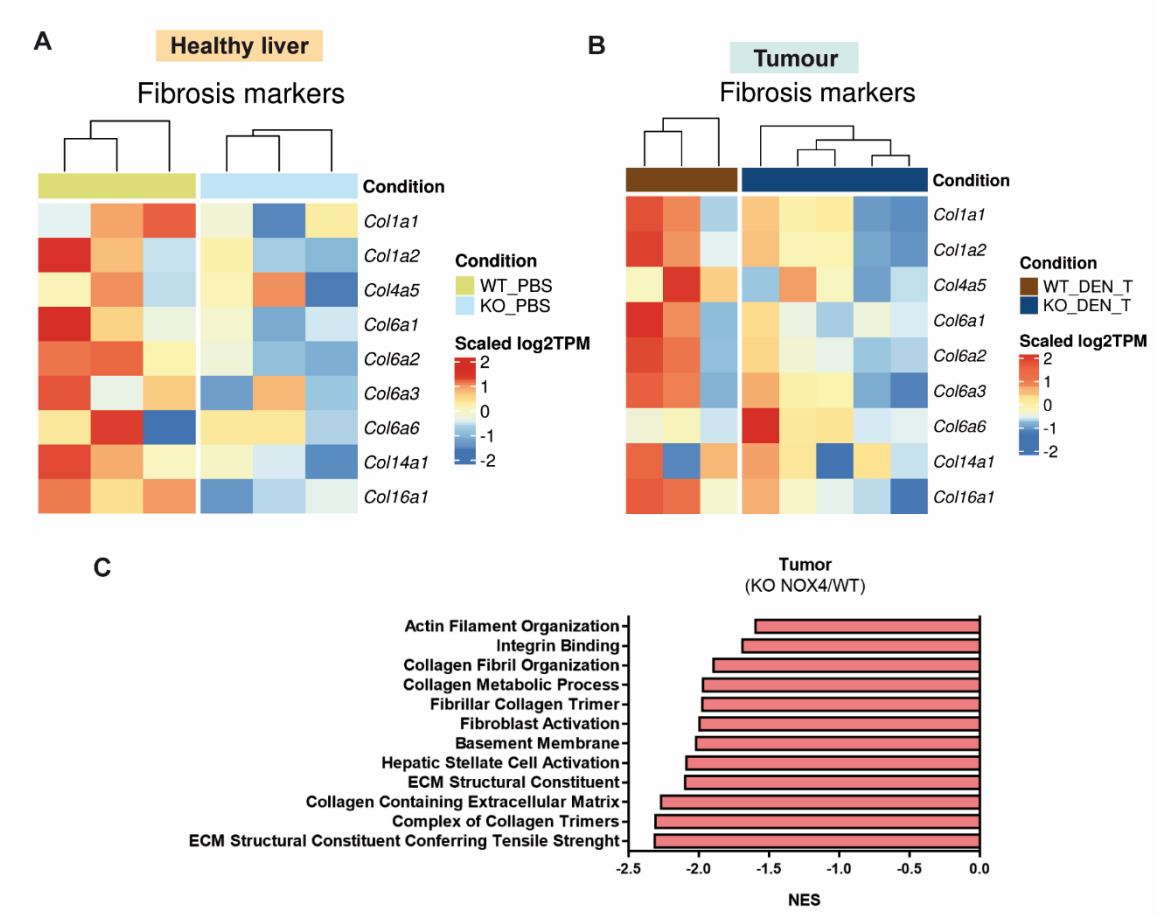

Figure 33. Analysis of RNAseq's fibrosis-related genes and pathways in the livers from WT and NOX4 -/- mice after 11-month DEN treatment. A-B Heatmaps of Relative expressions of Fibrosis Markers in WT compared to NOX4 -/- mice in PBS (**A**) or Tumour (**B**) conditions. Color scale indicates the GVSA score with red representing high enrichment and blue representing low enrichment. **C** Computational analysis of data from the RNAseq analysis. Enrichment analysis of biological functions based on the transciptomic level (M5 database).

Taking into account this promising results in RNAseq analysis, we wanted to check for potential differences in tumoral CAFs, in WT and NOX4 -/- tumours. α-SMA staining by IHC revealed a different disposition of the myofibroblast (**Figure 34A**). While WT mice had a more organised structure, which seemed to be surrounding the tumoral areas (checked either by H-E or Ki67), NOX4 -/- mice's myofibroblasts were disorganized among the parenchyma. *Acta2* gene was checked by qPCR, in a manner of quantification. An increase in tumoral areas, compared to non-tumour is shown (**Figure 34A**). However, no differences between WT and NOX4 -/- mice were seen.

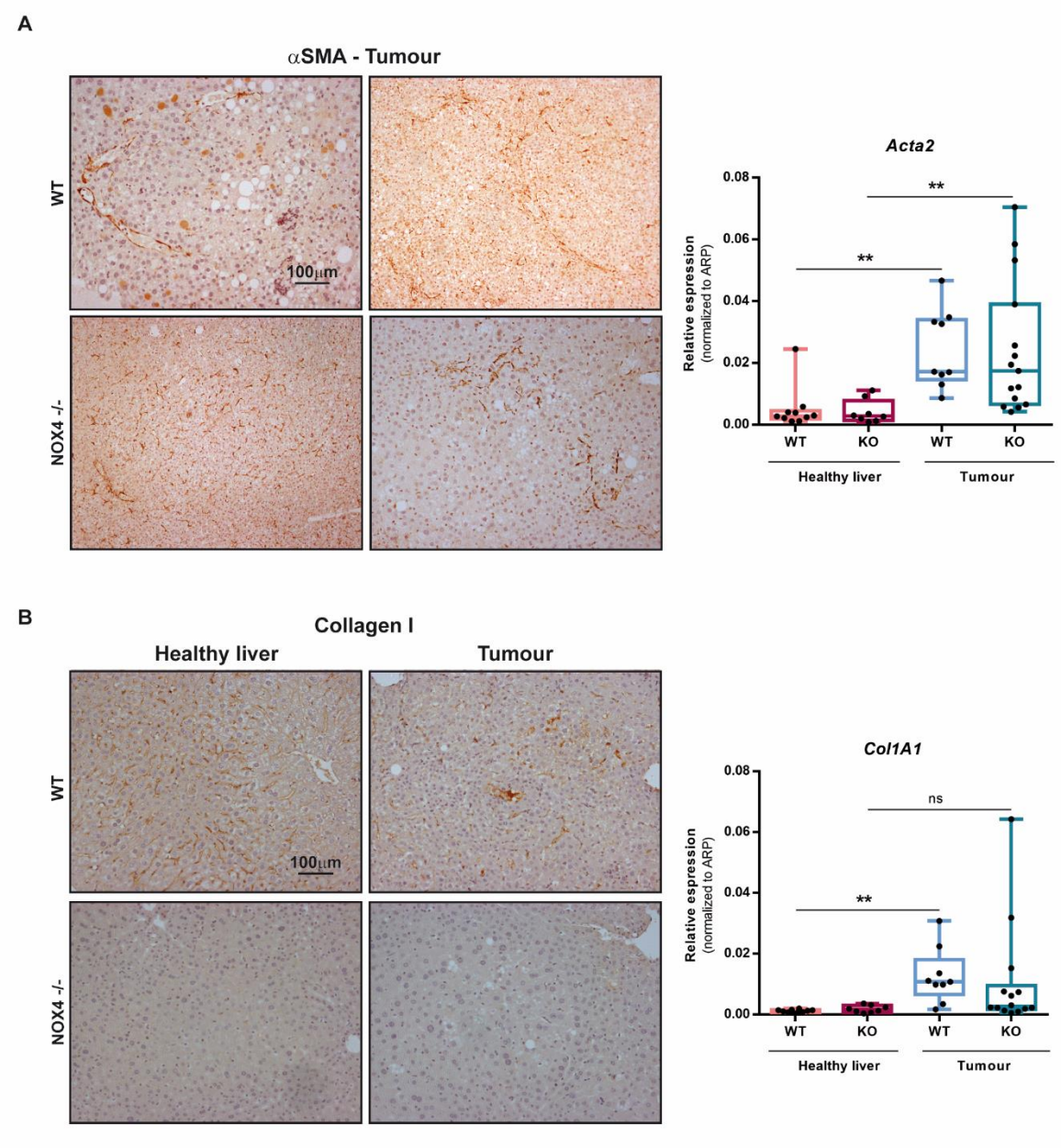

Figure 34. Analysis of activation of fibroblasts in the livers from WT and NOX4 -/- mice after 11-month DEN treatment. A Immunohistochemistry of α-SMA expression. Representative images shown (**left**). mRNA expression of *Acta2* gene analyzed by RT-qPCR in liver tumors from WT and NOX4 -/- mice at 11 months post-DEN treatment (**right**). **B** mRNA expression of *Col1A1* gene analyzed by RT-qPCR in liver tumors from WT and NOX4 -/- mice at 11 months post-DEN treatment (**left**). Immunohistochemistry of Collagen 1 expression. Representative images shown (**right**). *mARP* used as gene expression normalizer. In all the graphs, data are expressed as box plots with whiskers (min to max) (n=9: 3 lysates from 3 different animals).*p<0.05, **p<0.01

Because of the Collagen expression data results from the RNAseq analysis, we decided to check Collagen 1 at qPCR and protein level, too. On one hand, *Col1A1* (Collagen 1) RNA

expression showed a high increase in WT tumours compared to non-tumoral area (Figure 34B). This result correlates with the increment in Acta2, as more activated myofibroblasts are supposed to produce more ECM components. NOX4 -/- tumours presented high heterogeneity, but most of them showed no increase in *Col1A1* expression, corresponding with the results from the RNAseq, even if they also had the same levels of tumoral *Acta2* as WT do in tumours. Additionally, protein distribution was checked by IHC and Collagen 1 showed a very important difference (**Figure 34B**). Under carcinogenic conditions, levels and distribution of Collagen 1 were high in WT tumours, whereas NOX4 -/- livers presented a big reduction.

These results need further study, and given the importance of them, a new branch in the current research project is further analysing this, also in in vitro experiments.

5.4 Role of NOX4 in immune system profiling

Interestingly, one of the biggest differences we saw in pathways and specific markers was regarding the immune system landscape. This fact caught our attention, and we decided to further study this immune system profiling, taking advantage of the RNAseq data.

There, we observed a downregulation in a wide range of hallmarks regarding immune system activation. Again, basal condition (PBS, healthy liver) showed a downregulation in several generic Relative pathways in NOX4-deficient mice (**Figure 35A**). This surprising result could depict a tendency to NOX4 -/- mice to be more prone to have worse prognosis in HCC, as the immune system seems to be less capable of being activated. Furthermore, under hepatocarcinogenesis, these same pathways, showed a downregulation, too (**Figure 35B**). Additionally, similar to what we did for myofibroblasts' analysis, several pathways extracted from the M5 hallmarks database (*see section 11*) were analysed. Those more specific of T cells (**Figure 35 C**) and Inflammatory/Macrophages (**Figure 35 D**) had a negative NES in NOX4 -/- Tumours, correlating with the previous analysis.

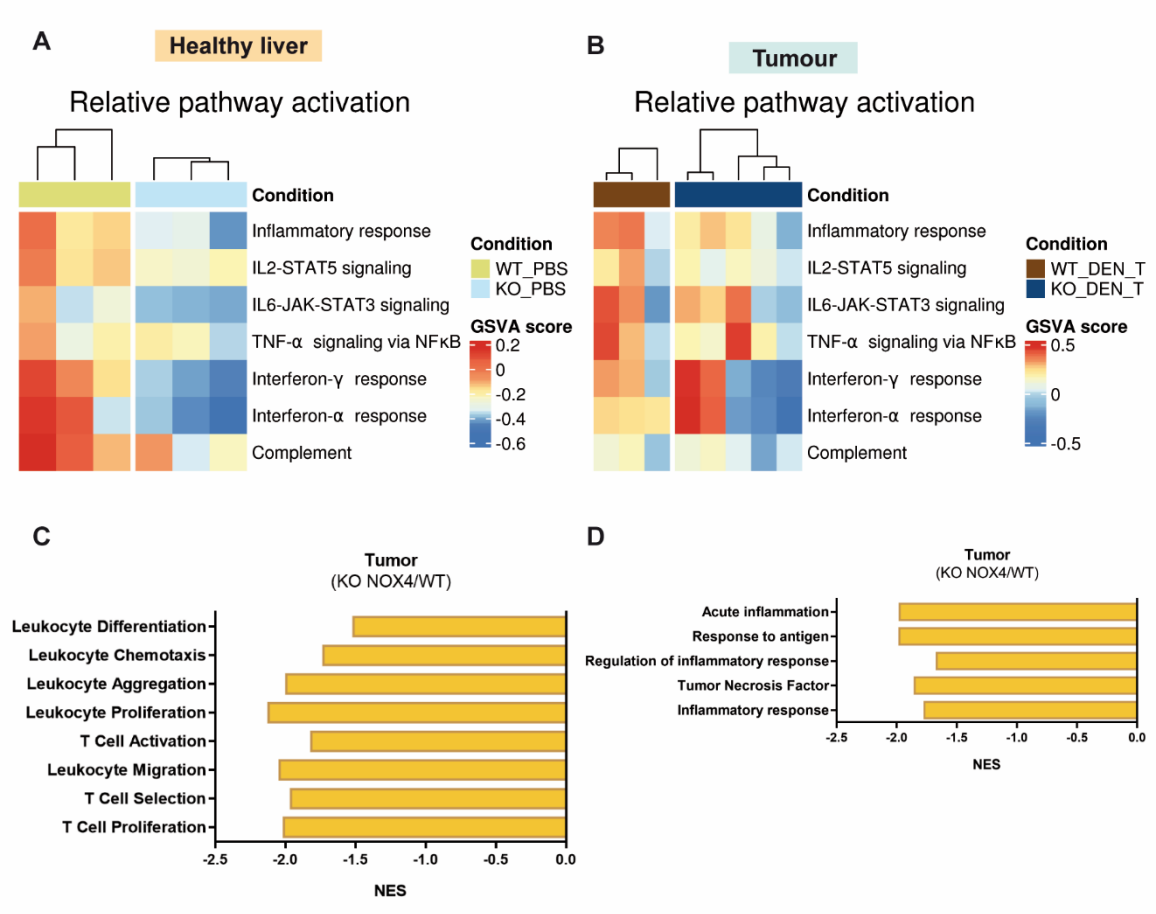

Figure 35. RNAseq analysis reveals differential expression in immune system hallmarks. A-B Heatmaps of Relative expressions of Immune system Hallmarks in WT compared to NOX4 -/- mice in PBS (**A**) or Tumour (**B**) conditions. Color scale indicates the GVSA score with red representing high enrichment and blue representing low enrichment. **C** Computational analysis of data from the RNAseq analysis. Enrichment analysis of T cell pathways based on the transciptomic level (M5 database). **D** Computational analysis of data from the RNAseq analysis. Enrichment analysis of inflammation pathways based on the transciptomic level (M5 database).

Overall, we had found that NOX4 -/- mice have an underactivated immune system, either in a healthy or carcinogenic situation, which made us wonder which are the specific populations that are affected by knocking out NOX4. First, an analysis in depth of the immune system relative enrichment through the seqImmuCC deconvolution method (*see section 11*) was performed. Clear differences in the predicted percentage of immune system populations were found, specifically in CD8+ T cells, that were much less in NOX4 -/- tumours (**Figure 36A**). Interestingly, another deconvolution method, mMCP-counter, showed more specific differences (**Figure 36B**). T cell population are elevated in WT Tumours, and specifically of

CD8+ cells, which is completely reversed in NOX4 -/- tumours. Finally, a clear tendency in NOX4 -/- tumours of some changes in the Monocyte/Macrophage population was seen (**Figure 36B**).

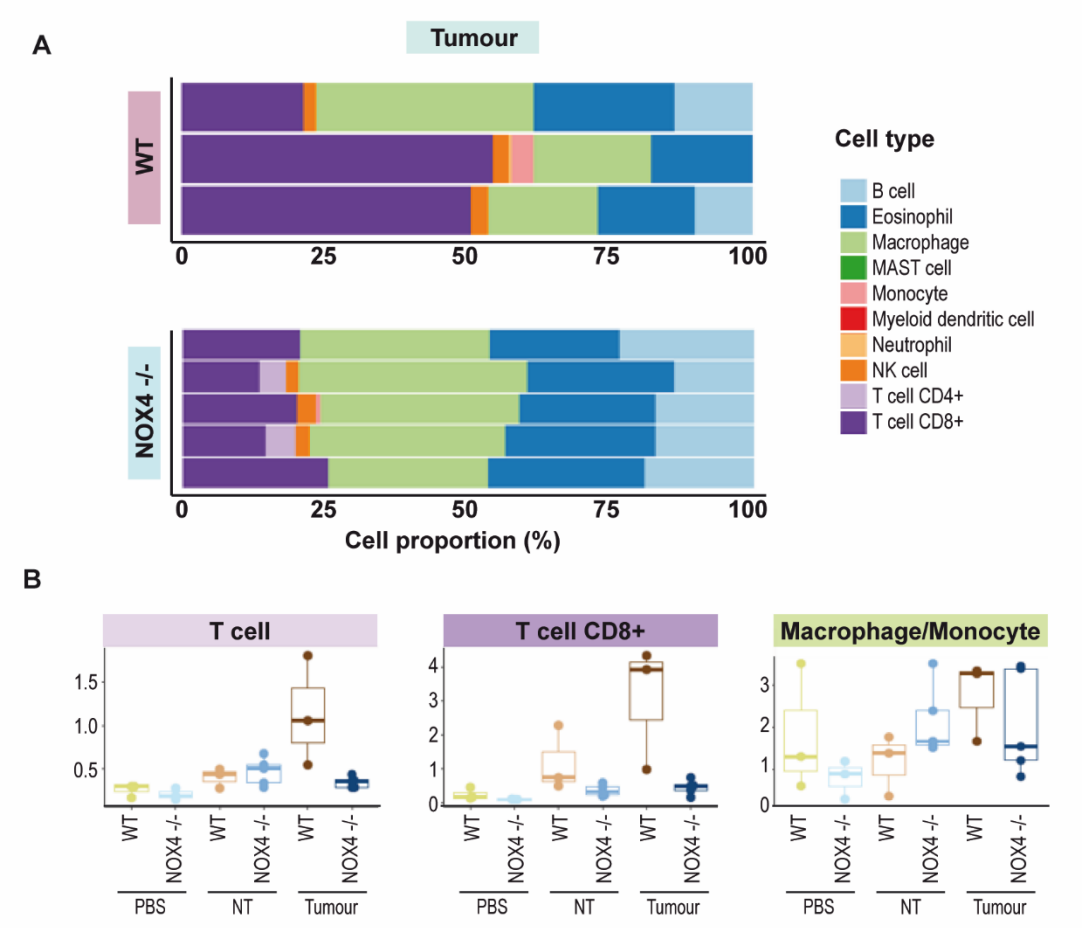

Figure 36. RNAseq analysis reveals different populations in immune system A Immune system relative enrichment by seqImmuCC dataset in WT compared to NOX4 -/- tumours. **B** Immune system relative enrichment by mMCP-counter dataset in WT compared to NOX4 -/- mice. T cell, T cell CD8+ and Macrophage/Monocyte are represented as boxplots.

Taking into account these last results, we then moved to analyse some specific gene markers for these immune populations that caught our attention. In this sense, specific T cell genes were analysed. As previously seen, lymphocyte markers were significantly less expressed in NOX4 -/- mice than in WT ones in healthy livers (**Figure 37**). Similarly, NOX4 -/- tumours had a "colder" T cell landscape profile when compared to WT tumours.

Regarding the macrophagic population, general markers for macrophages and also more specific ones for M1 or M2-like macrophages were analysed (**Figure 37**). Cd14 and Cd68 showed a downregulation in NOX4 -/-, either in healthy liver or in a tumoral situation. However, what was more striking of these results is the difference between the two phenotypes of macrophages. M1-like markers (*Tnf, Tnfsf12* and *Il12b*) were clearly more expressed in WT tumours, while M2-like markers (*Mrc1* and *Cd163*) were mostly expressed in NOX4 -/- tumours (**Figure 37**). This indicates that macrophages in NOX4-deleted HCC, undergo a phenotypic switch, which are often associated with a pro-tumoral behaviour.

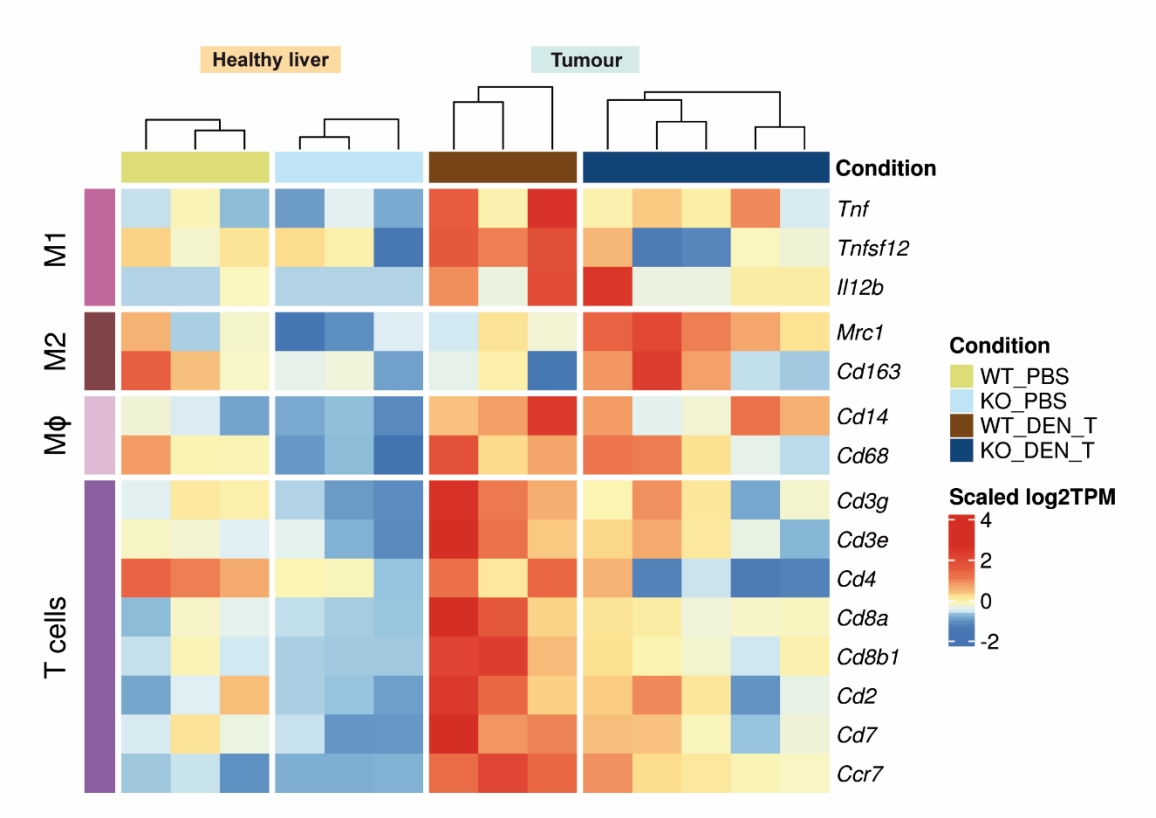

Figure 37. Heatmap of Scaled Log2TPM Expression Levels of Specific Immune System Cell Genes Data extracted from RNA seq analysis from WT and NOX4 -/- mice PBS and Tumour conditions. Each row represents a specific gene, and each column represents an individual sample. Color scale indicates the gene expression level, with red representing high expression and blue representing low expression.

To conclude, the most important results were checked in the mice tissue. First, CD68 IHC was performed to analyse the positivity of the tumoral tissues. All the DEN-induced samples were analysed (**Figure 38A**), but no differences were seen, nor in the quantity nor in

the distribution. Moreover, when gene expression levels were analysed, there was a high dispersion and no significant changes between WT or NOX4 -/- tumours (**Figure 38A**).

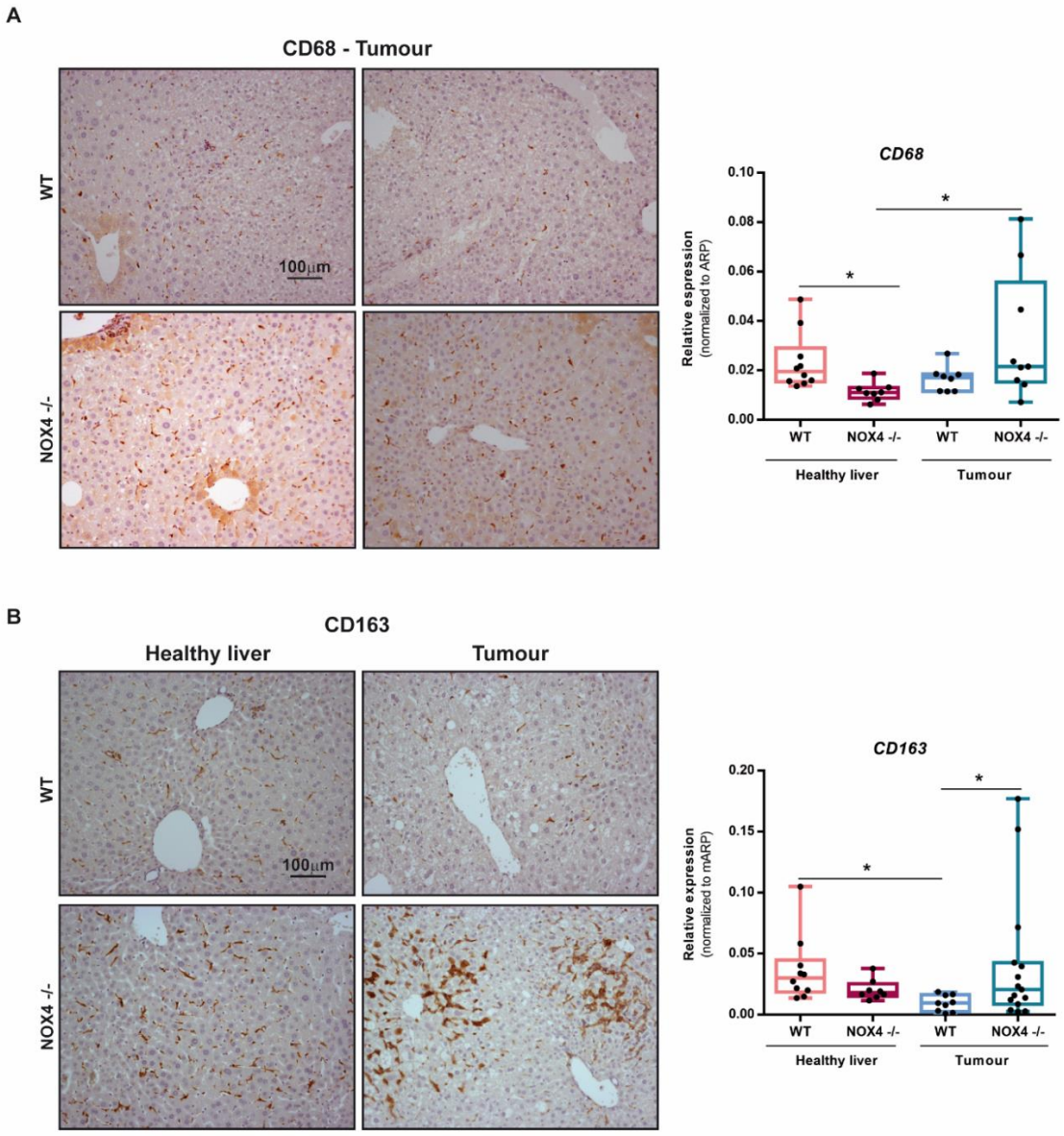

Figure 38. Histological and gene expression analysis show a distinct phenotype in macrophages
A Immunohistochemistry of CD68 expression. Representative images shown (**left**). mRNA expression of *CD68* gene analyzed by RT-qPCR in liver tumors from WT and NOX4 -/- mice at 11 months post-DEN treatment (**right**). **B** Immunohistochemistry of CD163 expression. Representative images shown (**left**). mRNA expression of *CD163* gene analyzed by RT-qPCR in liver tumors from WT and NOX4 -/- mice at 11 months post-DEN treatment (**right**). *mARP* used as gene expression normalizer. In all the graphs, data are expressed as box plots with whiskers (min to max) (n=9: 3 lysates from 3 different animals). *p<0.05. Scale bar 100µm.

Nevertheless, when we analysed CD163 by IHQ, an M2-like marker, images showed a high presence in NOX4 -/- mice, either at basal or under carcinogenesis (**Figure 38B**). The latest one was corroborated at gene expression level, where we could see a significant upregulation in NOX4 -/- tumours (**Figure 38B**).

In summary, all these results indicate that deleting NOX4 in mice leads to a general suppression of the immune system, which later on, under hepatocarcinogenesis, makes the NOX4 -/- tumour environment have an impact on immune system recruitment and macrophages phenotype.

6. Role of NOX4 in non-tumoral cells

Until now we have studied the interactions of tumoral and stromal cells by silencing NOX4 expression in HCC cells. On one hand, we have used two techniques, CRISPR-Cas9 or shRNA, to downregulate NOX4 at the *in vitro* approaches. On the other hand, we performed a DEN-induced hepatocarcinogenic model in WT and NOX4 -/- mice. This experiment allowed us to study the effect of knocking out NOX4 in all the cells of the organism. However, we still could not understand whether the data we were obtaining were the result of NOX4 in the stromal cells or in the HCC cells. To finally unravel this, we performed a syngeneic orthotopic experiment with mouse cells that have high NOX4 levels (**Figure 39**).

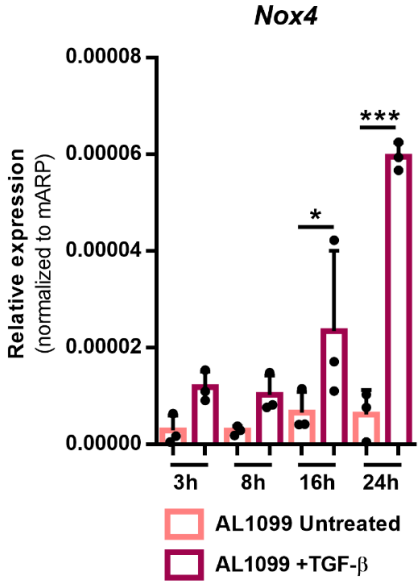

Figure 39. Characterization of the mouse HCC cells. *Nox4* mRNA expression in untreated or TGF-β-treated conditions, at different timepoints: 3h, 8h, 16h and 24h. *mARP* used as gene expression normalizer. Data are expressed as Mean±SD n=3.

This approach allows us to compare the progression and characteristics of HCC when the tumour has NOX4 levels, but stromal cells that may contribute to its worsening, do not. After three or four weeks, tumours were extracted from the mice (*see section 2.2*). Macroscopically, both in WT and in NOX4 -/- mice, great tumours developed (**Figure 40A**). Interestingly, when looking into *Nox4* expression in the tumour, coming from the cell lines, we observe that NOX4 -/- mice have lower levels compared to WT mice (**Figure 40A**).

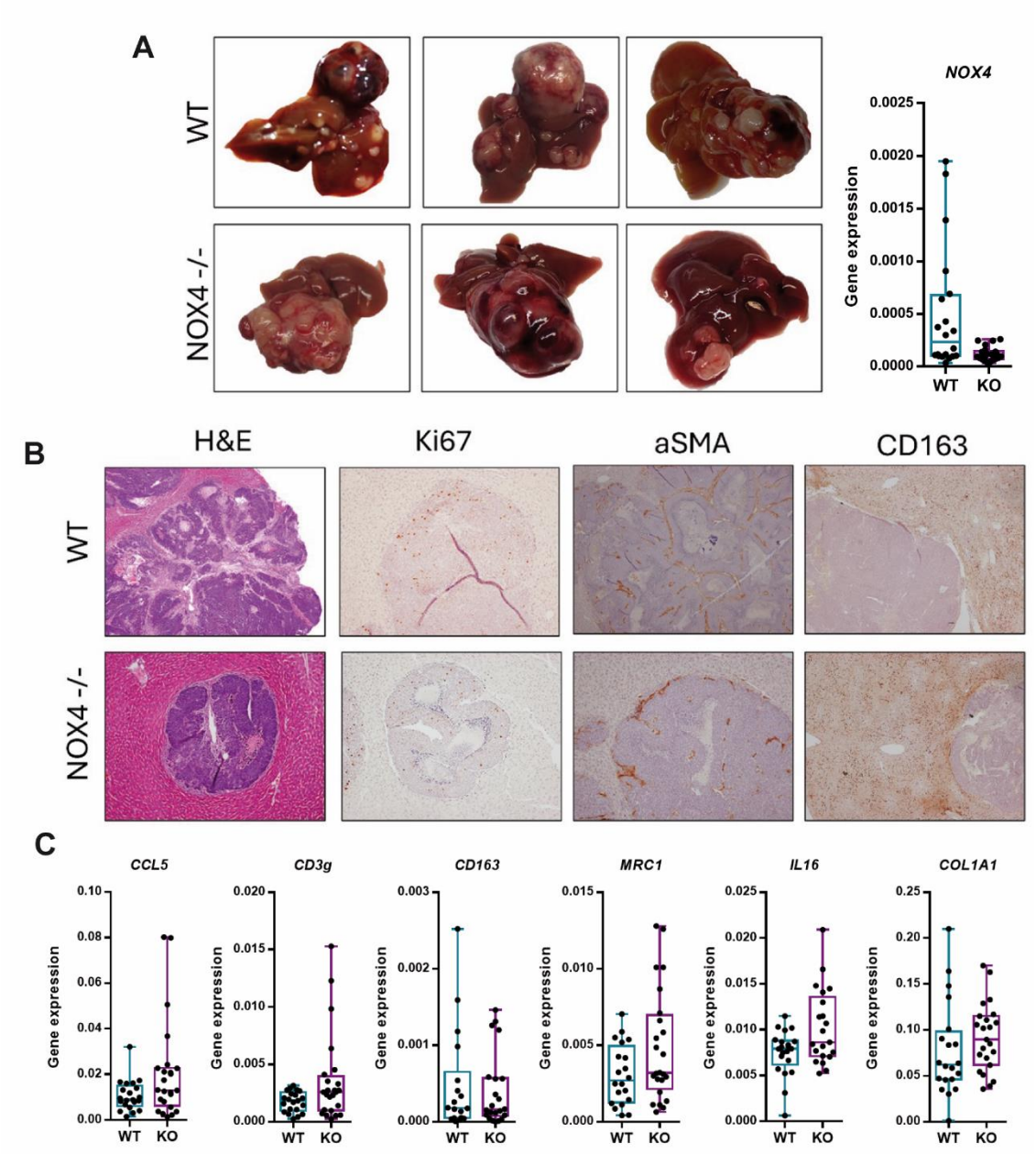

Figure 40. Characterization of the syngeneic HCC model. WT and NOX4 -/- in syngeneic HCC model **A** Macroscopical images of livers in WT and NOX4 -/- mice (**left**). *Nox4* mRNA expression in WT and NOX4 -/- tumours (**right**). **B** Haematoxylin and Eosin (H&E), Ki67, αSMA and CD163 in liver tumours. Representative images shown. Scale bar, . **C** *CCL5, CD3g, CD163, MRC1, IL16* and *COL1A1* mRNA expression in WT and NOX4 -/- tumours. *mARP* used as gene expression normalizer. In all the graphs, data are expressed as box plots with whiskers (min to max) (n=21: 3 lysates from 7 different animals).

Once we had characterized the macroscopical features, we wondered how the morphology of this tumours was. H&E (**Figure 40B**) showed that the component of the HCC syngeneic tumours was mainly mesenchymal, which was easily differentiated from the normal parenchyma. Besides, the non-tumoral parenchyma had a normal architecture. Moreover, when we stained with Ki67 to assess the proliferative capacity of these tumours, no major differences were found between WT and NOX4 -/- mice (**Figure 40B**). Just this indicated that both DEN and Syngeneic models of hepatocarcinogenesis, presented in a really different manner.

Interestingly, when we next moved to study the interaction with fibroblasts, we could not see differences between the conditions. On one side, IHQ of αSMA, which in DEN model presented a difference in the disposition, did not show changes in this case. On the other side, gene expression of *Col1A1* was not regulated in NOX4 -/- tumours, as we had previously found. Finally, we wondered if we could see the phenotypical switch in macrophages in this model. To do so, we performed IHQ of CD163, the M2-like macrophagic marker, and a subset of several immune-related genes that had been significantly regulated in RNAseq analysis (**Figure 40B-C**). Even though it was obvious that a greater number of CD163+ macrophages were along the non-tumoral parenchyma, none were inside the tumoral area. Additionally, gene expression showed no changes between WT and NOX4 -/-.

Overall, these last results indicate that is NOX4 deletion specifically in HCC cells which affect the interaction between tumoral cells and stroma, particularly fibroblasts activation and disposition, and T cells or macrophages.

7. Impact of NOX4 on HCC 3D spheroids

In vivo experiments in DEN-induced hepatocarcinogenesis indicated that deleting NOX4 leads to a depressed immune system, which may contribute to tumour progression. However, although *in vivo* models confer a good way to mimic the TME, they are also a complex model to analyse in detail the cell-cell interaction. The results obtained in the syngenic model, where WT liver tumour cells were injected, indicated that is the expression of NOX4 in the tumour cells who may determine the effects on the microenvironment. Given the interesting results seen in macrophages, we next wanted to further study the role of NOX4 in the interactome between HCC cells and macrophages. To do so, we moved to *in vitro* 3D experiments that involve the co-culture of macrophages with a 3D spheroid of HCC cells. It is worthy mentioning that, due to the huge results observed in T cells, another part of the current research group projects is focusing on further analysing these immune cells.

7.1 Set up of 3D spheroid model with HCC cells

In this part, we worked with a model of NOX4 silencing in PLC/PRF/5 cells performed by shRNA (ShControl or ShNOX4) as it is better characterized in our research group[133, 219]. Spheroids were created by hanging drop technique (*see section 3.2*), which was an optimized method in our group that showed a good reproducibility. This approach allows us to also study the TGF-β-NOX4 axis in this model, as we can expose the spheroids to the cytokine. First of all, we started by characterizing the tumoral spheroids by themselves, to also assess other features such as proliferation, among other things. After collecting the spheroids, they were cultured and monitored for 48 hours.

PLC/PRF/5 Control cells displayed a good formation of spheres, that grow during the culture (**Figure 41A**). Besides, PLC/PRF/5 ShNOX4 spheroids show higher proliferation and progression, in terms of spheroid area, confirming the proposed role in mediating the growth inhibition. Moreover, they also appear to be proliferating aberrantly and in an uncontrolled

manner, as the spheroids lose circularity (**Figure 41B**). Additionally, when PLC/PRF/5 ShControl spheroids were incubated with TGF-β, the spheres formed were smaller from time 0h, and they did not grow over culture, undergoing the TGF-β-mediated inhibition of proliferation also in 3D, and the spheroids appear smaller and "denser". However, when the treatment is done in the cells with the silencing of NOX4, the spheroids are not only smaller, but also aberrant and disintegrated (**Figure 41A**).

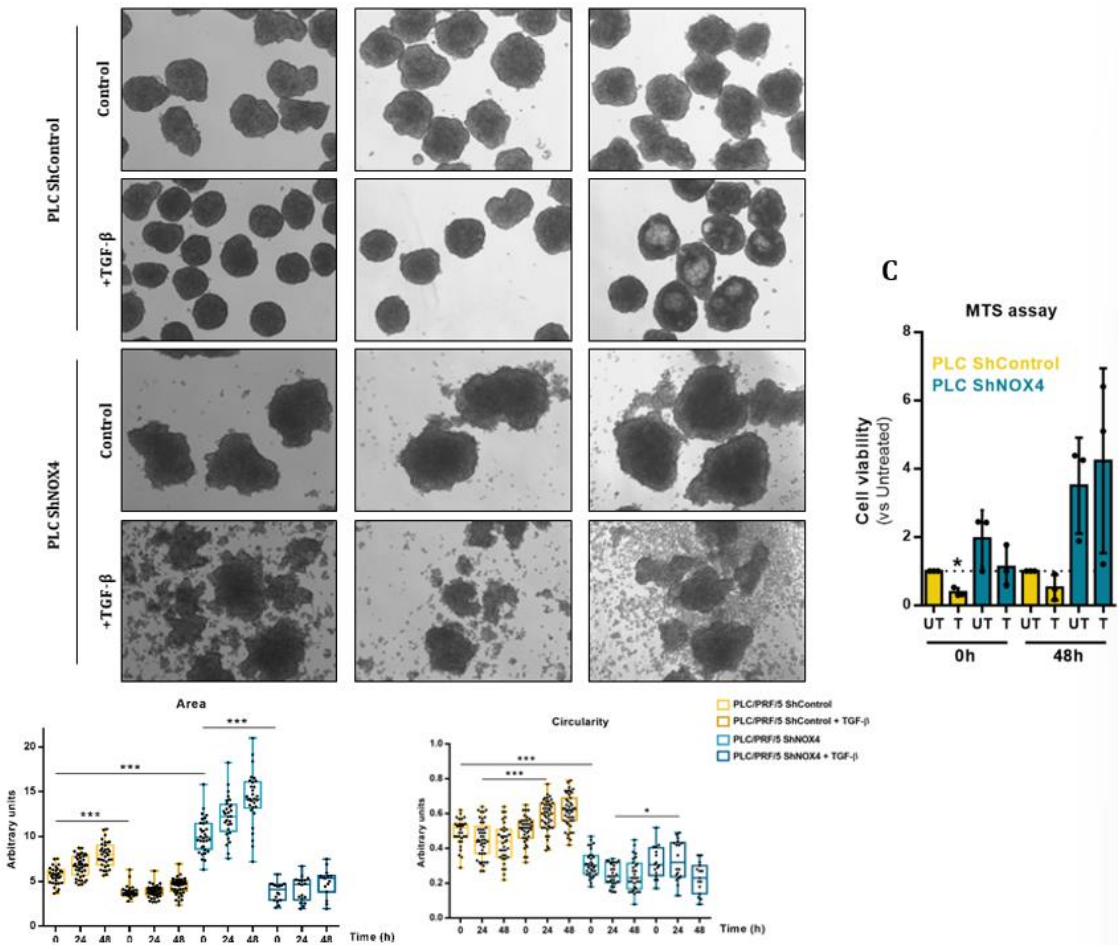

Figure 41. In vitro 3D models to study the role of NOX4 in HCC cells in the absence or presence of TGF-β. PLC/PRF/5 cell line was used with a stable silencing of NOX4 with ShRNA. **A** Characterization of the PLC/PRF/5 spheroid development at 0, 24 and 48 hours with or without 2ng/ml of TGF-β treatment. Scale bar 200μm. **B** Quantification of spheroid area (**left**) and circularity (**right**) by Image J software. **C** Cell viability analysis assessed by MTS assay. Data represented vs each Untreated condition, at 0h and 48h after collecting the spheroids. Data are Mean ± SD (n = 3). *p<0.05, **p<0.01, ***p<0.001.

This last result was unexpected for us, as NOX4-silenced cells were not supposed to respond to TGF-β by seemingly stopping proliferation or dying. Therefore, we decided to further study this phenomenon and elucidate what was happening.

The first thing that we wanted to clarify is if 3D culture was affecting the viability of the cells, as it is known to be a harder environment. An MTS assay (*see section 7.2*) showed that in PLC ShControl treated with TGF-β, there were significantly less viable cells that in untreated conditions (**Figure 41C**). Also, PLC/PRF/5 ShNOX4 had an increase in the number of viable cells, correlating with the area increment. Interestingly, TGF-β treatment did not decrease cell viability (**Figure 41C**), meaning that the floating cells are not dead, but unattached.

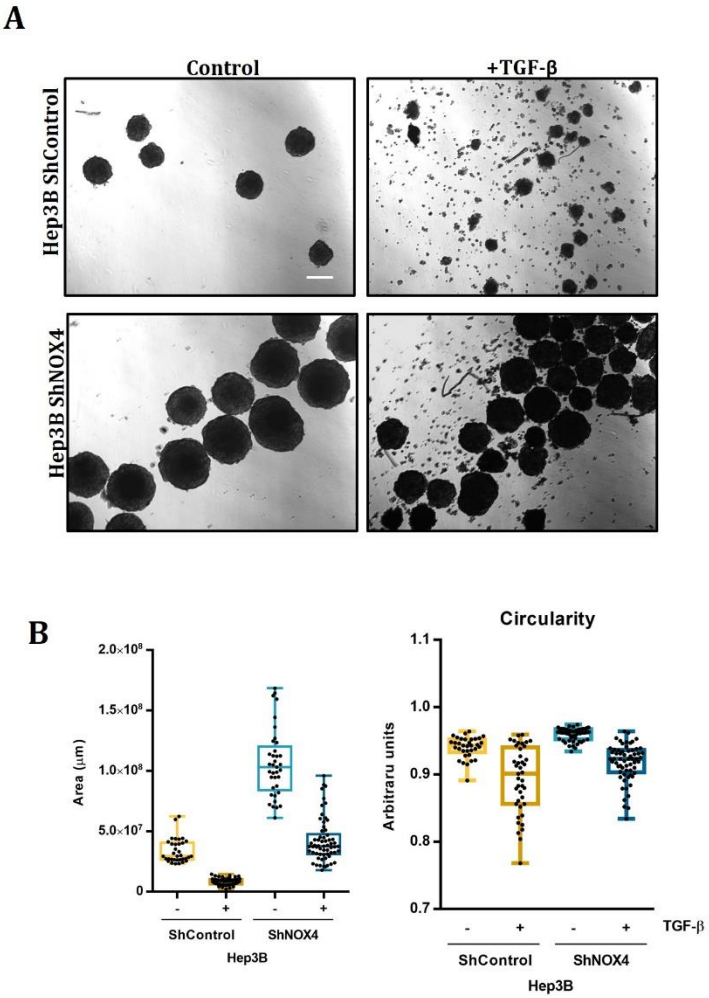

Figure 42. In vitro 3D models to study the role of NOX4 in HCC cells in the absence or presence of TGF-β. Hep3B cell line was used with a stable silencing of NOX4 with ShRNA. **A** Representative image of Hep3B spheroids at selected time of 72 hours post TGF-β treatment. Scale bar 200μm. **B** Quantification of spheroid area (**left**) and circularity (**right**) by Image J software.

As a proof of concept, we also checked for the formation and progression of 3D spheroids in another HCC cell line, Hep3B cells that had also NOX4 silenced by ShRNA[133]. Similar results were seen in Hep3B cell lines, where ShControl cells responded really well to

TGF-β in terms of growth inhibition and be less responsive to TGF-β in terms of growth inhibition (**Figure 42**).

7.2 Role of NOX4 in TGF-β-induced structural differences in 3D spheroids

At this point, we still had the question mark on the condition with TGF-β treatment in PLC/PRF/5 ShNOX4 spheroids. They can be characterized in several ways. One of them is by analysing the structure their cells are capable of maintaining. Several stainings were performed in spheroids that had been previously embedded in paraffin (*see section 8.2.2*). H-E revealed that untreated PLC/PRF/5 ShControl spheroids had some "holes" in the centre of the sphere, which could suggest some kind of death in the core, probably necrosis. On the contrary, this feature was not found in PLC/PRF/5 ShNOX4 spheroids, even when treated with TGF-β, result that could point to a protection from death, which typically happens due to lack of oxygen or nutrients in the core (**Figure 43A**).

When wondering about the reason why TGF-β-treated PLC ShNOX4 spheroids are disintegrated and aiming to better analyse the cohesive ability of the cells in 3D, we analysed E-Cadherin and N-Cadherin (**Figure 43B-C**). PLC ShNOX4 spheroids have much less levels of both proteins, both at treated and untreated conditions, something expected for previous results from the group[219]. However, TGF-β treatment in PLC ShControl show an increase in E-cadherin but a slight decrease in N-cadherin expression. What action TGF-β-treatment is doing in PLC ShNOX4 spheroids is yet to be elucidated, so further investigation will be done to better understand. We believe this could be a critical point, because of its potential implication in prognosis or migration.

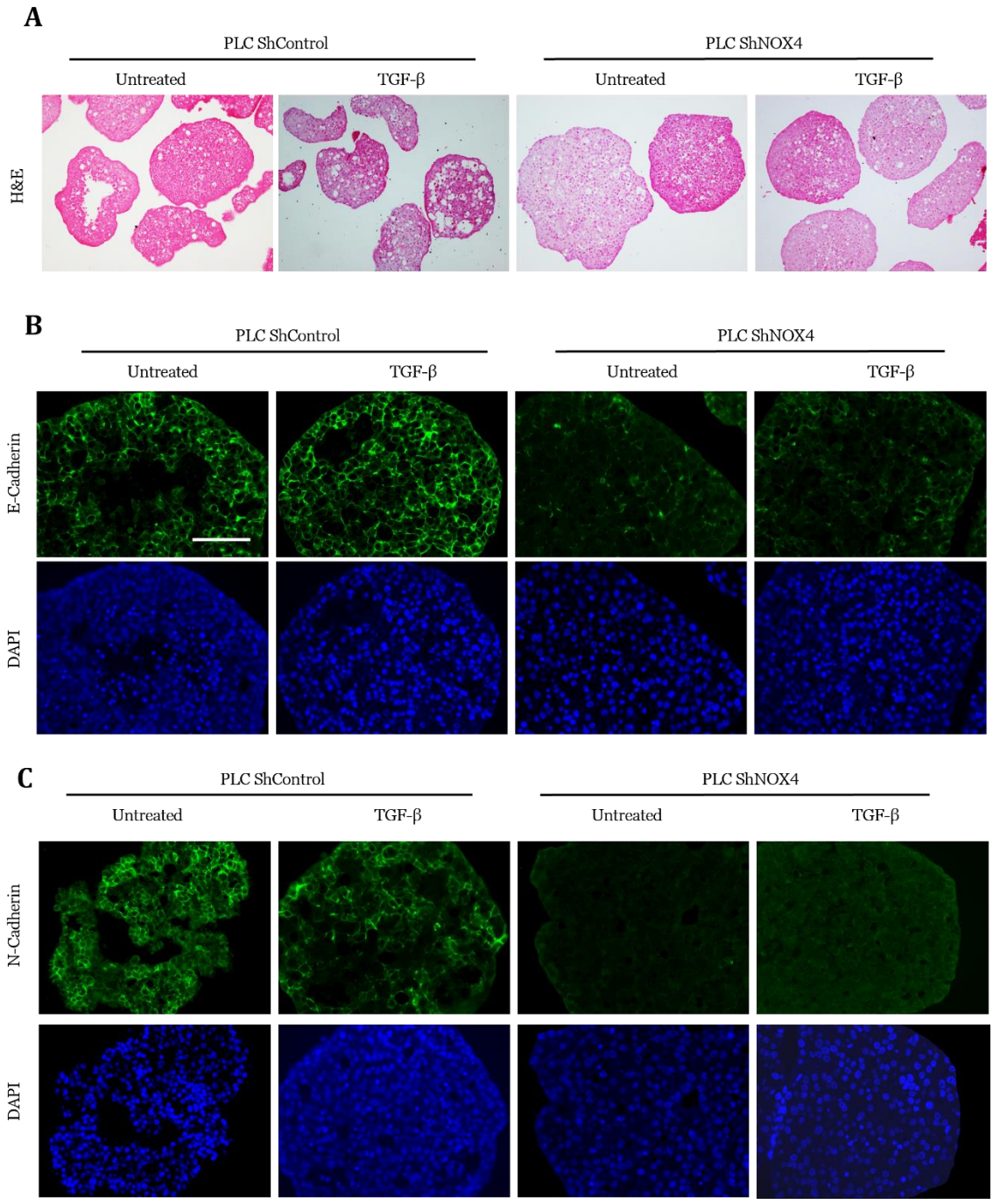

Figure 43. Characterization of HCC spheroids in the absence or presence of TGF-β. PLC/PRF/5 cell line was used with a stable silencing of NOX4 with ShRNA. Spheroids were included in paraffin at 24h. **A** Haematoxylin-Eosin staining of PLC spheroids. **B** E-cadherin (green) staining of spheroids at 24h with or without 2ng/ml of TGF-β treatment. **C** N-cadherin (green) staining of spheroids at 24h with or without 2ng/ml of TGF-β treatment. DAPI (blue) was used as nuclei staining. Scale bar, 100μm

7.3 Role of NOX4 in the interactome between tumour and macrophages

To better analyse the interactome between HCC cells and monocytes/macrophages in the laboratory, we decided to work with THP-1 cell line. This cell line is a monocytic cell line, which allows us to focus in the effect on their activation and action.

In this sense, we have optimized the co-culture of the tumoral cells PLC/PRF/5 ShControl or ShNOX4 with THP-1. THP-1 monocytes were previously pre-activated with TGF-β 48 hours prior to the formation of the multicellular spheroids.

Spheroids were formed with the usual HCC cells number, with an added 10% of THP-1 cells (untreated or pre-activated), which were previously marked in green to monitor the co-culture (**Figure 44**). Images were taken at the collection time (0h), 24h and 48h, while the spheroids were in a low-attachment plate. Interestingly, as the area quantification shows (**Figure 44**), in PLC/PRF/5 ShControl, addition of THP-1 decreased the spheroid size, as TGF-β does. However, in the case of PLC/PRF/5 ShNOX4, the smaller area was only seen in the presence of TGF-β treatment, not when THP-1 where not pre-treated. This suggests that some difference in the interactome depends on NOX4 presence in HCC tumours. In fact, although co-culture of PLC/PRF/5 ShNOX4 spheroids with TGF-β treatment were smaller, a better preservation than without THP-1 could be seen, showing a contribution of macrophages in forming and maintaining the spheroid structure (**Figure 44**).

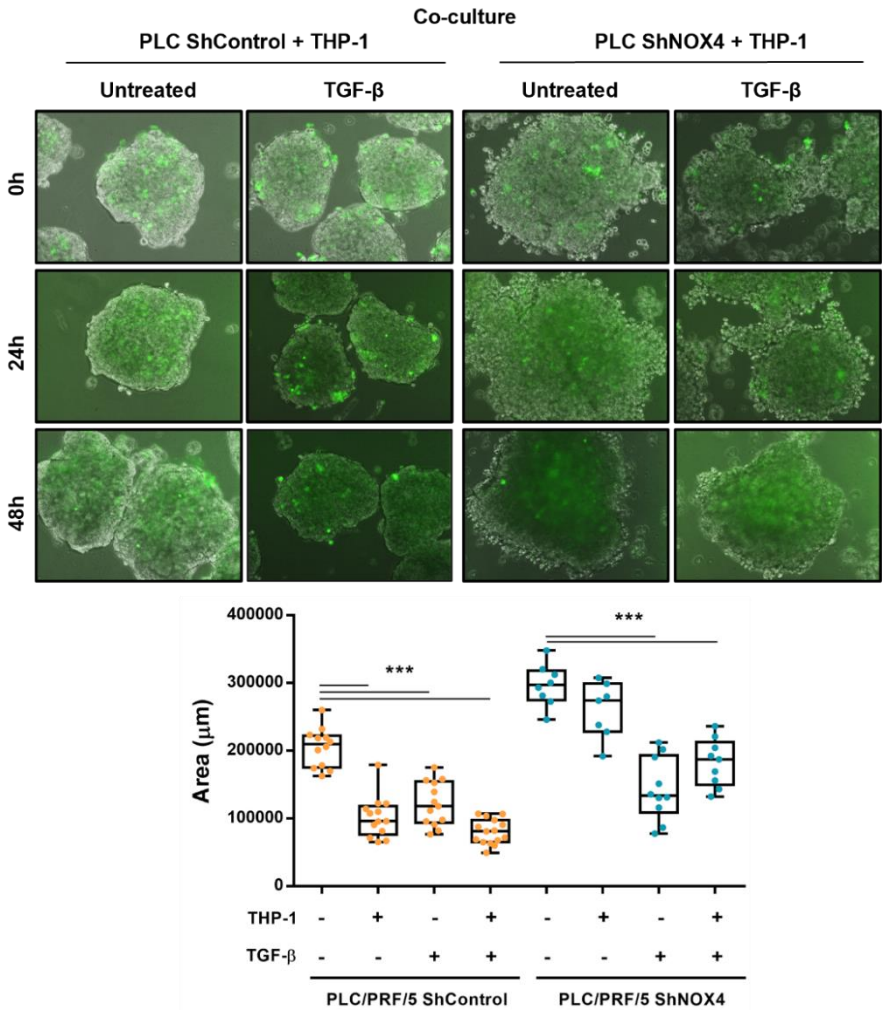

Figure 44. In vitro 3D co-culture model to study the role of NOX4 in HCC cells in the absence or presence of monocytic cell line THP-1. PLC/PRF/5 cell line was used with a stable silencing of NOX4 with ShRNA, and THP-1 cell line. Representative fluorescent images of spheroids at 0, 24 and 48 hours (**left**). THP-1 monocytes tagged in green. Quantification of spheroid area (**right**).

Then, the proliferative capacity of the cells in 3D was assessed (**Figure 45A**). Proliferation is often described in the outer ring of the sphere, as nutrient/oxygen gradients determine these actions. On one hand, in monoculture (only HCC), Ki67 staining shows a higher proliferative capacity in PLC ShNOX4 spheroids, as expected from previous results from the group. Intriguingly, TGF-β-mediated growth inhibition could not be seen in PLC/PRF/5 ShControl, as the percentage of Ki67-positive nuclei did not change significantly from the Untreated condition. On the other hand, in THP-1 co-culture, adding pre-activated THP-1 cells to the PLC/PRF/5 ShControl spheroid gave them a higher proliferative capacity. The same effect was seen in PLC/PRF/5 ShNOX4 spheroids with untreated THP-1 (**Figure 45A**).

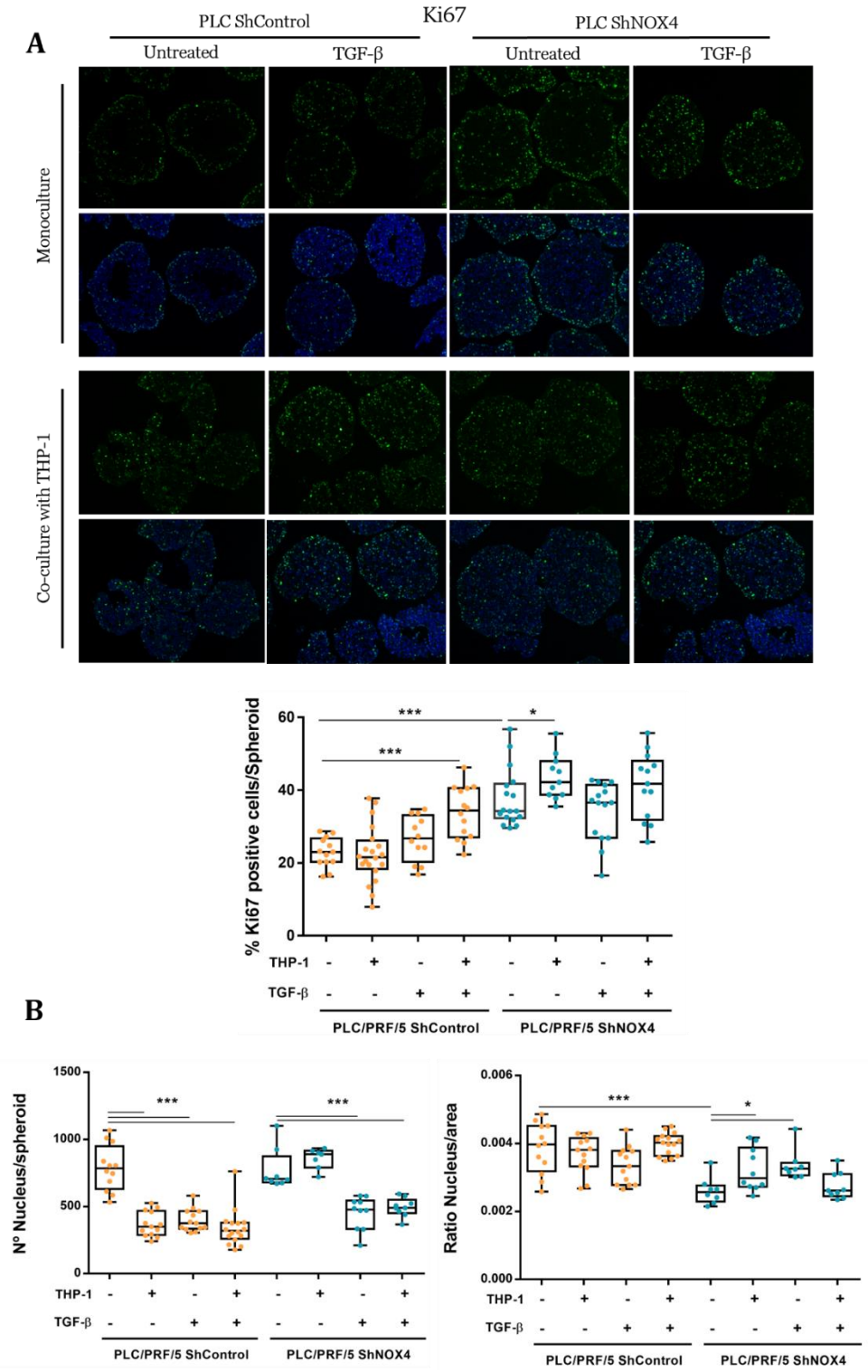

Figure 45. In vitro 3D co-culture model to study the role of NOX4 in HCC cells in the absence or presence of monocytic cell line THP-1. PLC/PRF/5 cell line was used with a stable silencing of NOX4 with ShRNA, and THP-1 cell line. **B** Ki67 (green) staining of spheroids at 24h with or without 2ng/ml of TGF-β treatment, in monoculture (only PLC) or Co-culture (with THP-1 or pre-activated THP-1). DAPI (blue) was used as nuclei staining (**left**). Quantification of the Ki67% positive nuclei per spheroid (**right**). **C** Quantification of the number of nuclei per spheroid (**left**) and the Ratio of nuclei/Area (**right**). All quantifications made with Image J software.

One extra characteristic we took a look into is the number of nuclei in each spheroid, as it seemed that when treated with TGF-β they appeared to be closer to each other. Therefore, we first quantified the number of nuclei per spheroid (**Figure 45B**). The number of nuclei was significantly decreased among all the conditions of PLC/PRF/5 ShControl, as happened with the PLC/PRF/5 ShNOX4, except for THP-1 co-culture. With this information and the area of each sphere, the density of nuclei per spheroid area was quantified (**Figure 45B**) by calculating the ratio between the Number of nuclei per spheroid vs the Area of the spheroids. This ratio did not change among all the conditions in the PLC/PRF/5 ShControl. However, PLC/PRF/5 ShNOX4 were less dense than ShControl, having the nuclei more separated among them. The condition with THP-1 and TGF-β treatment in PLC/PRF/5 ShNOX4 increased the ratio, meaning that the cells are much closer to one another.

7.4 Role of NOX4 in the macrophagic phenotype

For the last part of this project, considering the results we had seen *in vivo*, we wanted to further analyse how NOX4 in HCC can regulate the recruitment and phenotype of macrophages.

In **Figure 46**, an immunofluorescence of CD68 (macrophage marker, red) and CD163 (M2-like macrophage marker, green) is observed. Results point to a higher proportion of CD163 positive macrophages in PLC ShControl spheroids. This is a point which is being unravelled at this moment, and further investigation is needed.

Besides, one of the other aspects that had caught our attention in the co-culture, was the different ratio of monocytes/macrophages, marked in green, in some conditions. Even though it is not the best approach to assess this, there seemed to be some changes in recruitment.

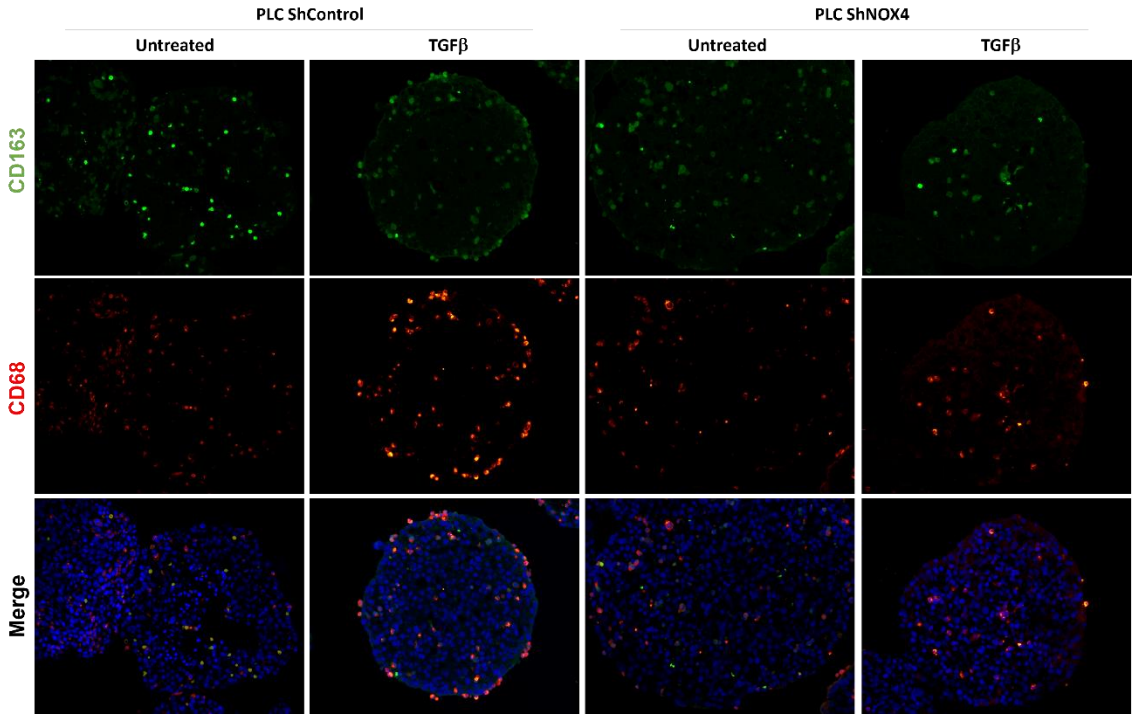

Figure 46. Characterization of HCC spheroids in presence of monocytic cell line THP-1 and the absence or presence of TGF-β. PLC/PRF/5 cell line was used with a stable silencing of NOX4 with ShRNA. CD163 (green) and CD68 (red) staining of spheroids at 24hours, with or without 2ng/ml of TGF-β treatment. DAPI (blue) was used as nuclei staining.

One disadvantage that we found in the co-cultures was that, if we wanted to analyse gene expression from those samples, we would not be able to differentiate coming from mRNA from HCC cells or from macrophages. As a way to fix that, we designed some experiments where we collected CM from HCC spheroids after 48 hours of culture. Then, THP-1 were incubated with this CM from PLC/PRF/5 ShControl or ShNOX4 spheroids for the required time (**Figure 47**).

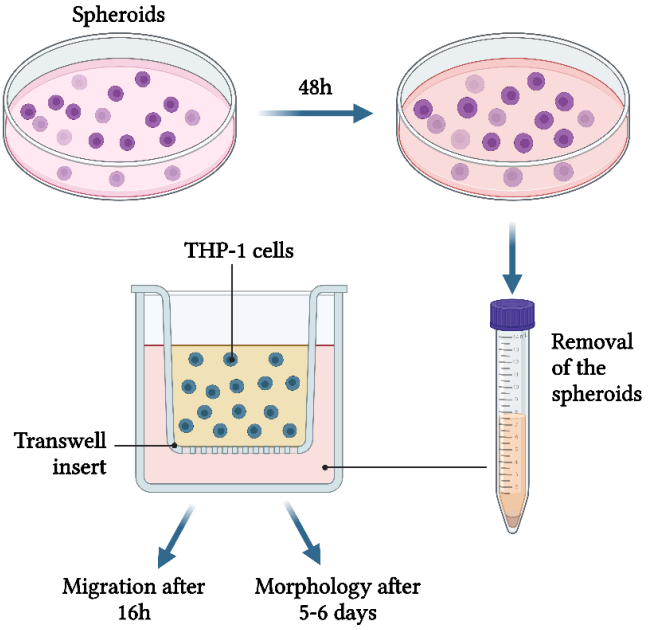

Figure 47. Diagram of experiment. Spheroids are formed and collected as usual. After 48h of culture, the spheroids are discarded, and the remaining media collected. Transwell assay is performed with the CM in the bottom chamber, and the THP-1 on the top chamber.

To assess the recruitment capacity of each CM, two-chambers assays were done. These consist of a transwell assay where the bottom chamber contains the CM, either from PLC/PRF/5 ShControl or ShNOX4, and the top chamber contains THP-1 cells, previously marked in green. After 16h, cells that had migrated through the transwell where monitored and quantified (**Figure 48**). Results show a significant increase in the chemotaxis of THP-1 towards CM from PLC ShNOX4 (**Figure 48**). Moreover, an important change in the THP-1 morphology is seen in this condition, too, probably reflecting an increased activation (**Figure 48B**). To better understand this phenotypic change, an array of inflammatory cytokines would be adequate to analyse in this last part.

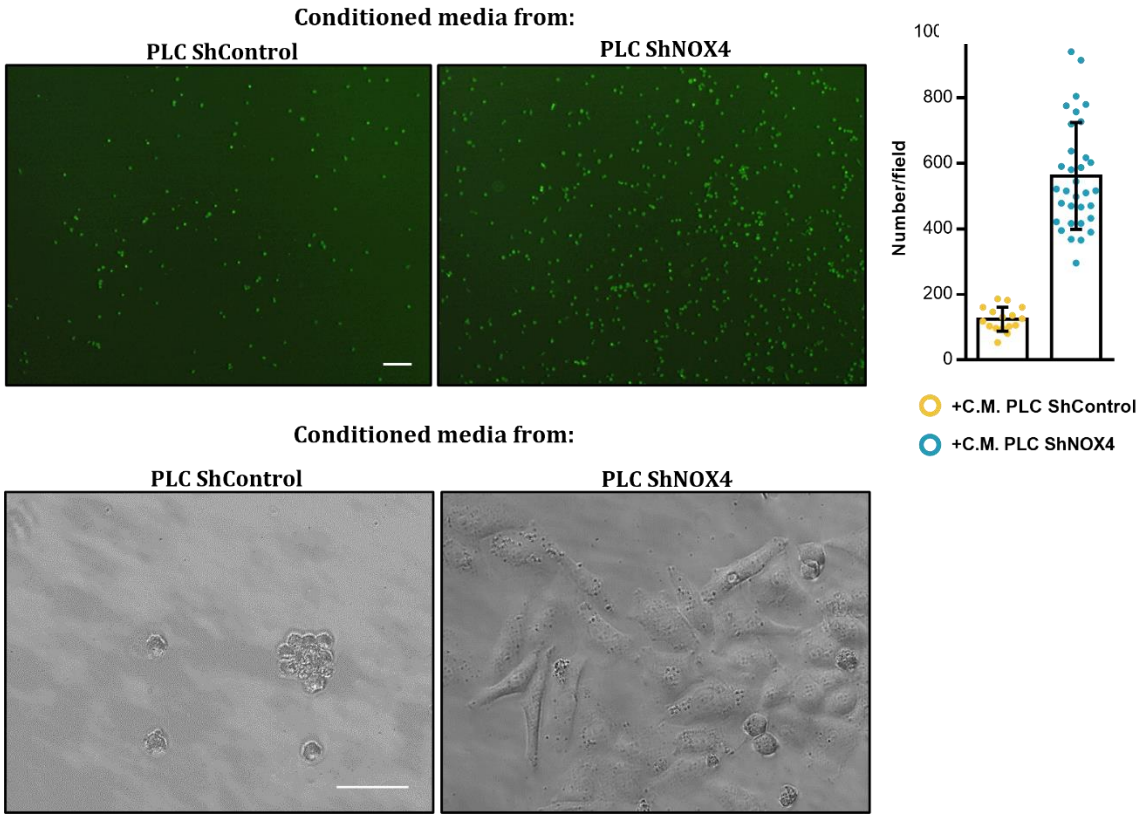

Figure 48. THP-1 monocytic cell line have more attraction to the conditioned media from spheroids of PLC/PRF/5 cells without NOX4. Analysis of the recruitment capacity and effects of the CM on the THP-1 with transwell assay technique. Images of the THP-1 cells (green) that have migrated through the transwell (**left**). Quantification of the number of cells in the bottom well (**right**). Data is mean ±S.D. of at least 16 fields per condition. Representative phase contrast images of THP-1 cells after migrating through the transwell well and incubation with the conditioned media for 4-5 days (**bottom**).

DISCUSSION

HCC is one of the deadliest malignancies worldwide because of its high recurrence rate, high metastatic potential, and resistance to drugs [230]. Elucidation of the mechanisms underlying malignancy in HCC is needed to improve diagnosis, therapy, and prognosis.

1. Role of NOX4 in TGF-β signalling in HCC

The first part of my thesis points to a crucial role for NOX4 in regulating both suppressor and pro-tumorigenic signals induced by TGF-β. On one side, NOX4 is required for an efficient SMADs phosphorylation and full inhibition of cell proliferation by TGF-β. Although the specific targets of the NOX4-mediated ROS are unclear, we may speculate that inactivation of protein phosphatases could be a probable possibility. In this sense, it has been proposed that protein phosphatase 2A (PP2A), physically interact with SMAD2/3, thereby promoting their dephosphorylation[231] and absence of Nox4 facilitates nuclear PP2A translocation in murine models of carcinogen-induced solid tumours[232]. In terms of proliferation, probably the most relevant aspect is that the absence of NOX4 provoked increase in the expression of MYC and Cyclin D1, being TGF-β unable of properly down-regulate the expression of these genes. Cyclin D1 is required for HCC cell proliferation and previous results strongly demonstrated that its overexpression impairs TGF-β-induced growth inhibition[233]. Indeed, the capacity of TGF-β to inhibit proliferation in CRISPR NOX4 cells may be significantly attenuated due to the high levels of Cyclin D1. Furthermore, NOX4 is required for an efficient TGF-β-induced apoptosis. Although these results could be expected, the previous experiments were performed by transiently knock-down of NOX4[52]. Results here reinforce the crucial role of NOX4 in TGF-β-induced apoptosis, showing no compensatory mechanism when NOX4 is stably silenced for long time. TGF-β induces pro-apoptotic genes (such as *BMF* or *BCL2L11*) in primary cultures of hepatocytes, but also increases the levels of anti-apoptotic genes, such as *Bcl-xL*, the balance among them decides cell fate[59]. Inhibition of survival signals, such as the EGFR or the MAPK/ERKs pathways, abrogates the increase in the expression of the anti-apoptotic genes, in particular *Bcl-xL*, and significantly enhances cell death[57,59,234]. Results here shown demonstrate a role for NOX4 not through transcriptional regulation of pro-apoptotic genes,

but through post-transcriptional regulation of anti-apoptotic proteins, particularly Bcl-xL. Indeed, in the absence of NOX4, apoptosis may be prevented by the high levels of Bcl-xL. Considering this essential role of NOX4 in TGF-β-induced tumour suppressor functions, it should have been expected that in HCC patients presenting high expression levels of TGF-β ligands and/or receptors, high level of NOX4 expression may define a better prognosis. Contrary to these expectations, analysis in a cohort of patient from the HUB in our campus, as well as in silico data from TCGA public data, revealed that high expression of NOX4 defines a worse overall survival in patients presenting high expression of TGF-β-related genes or a TGF-β cancer-related gene signature. A more detailed analysis in the HUB cohort correlated this $NOX4^{high}$/$TGFB1^{high}$ group with a more aggressive phenotype. This stratification of patients has facilitated a better comprehension of the role of NOX4 in HCC and could explain the controversial data in the literature, with some publications defending a better prognosis [134,135], not any relevance, or even worse prognosis for $NOX4^{high}$ patients [123].

The reason for the potential role of NOX4 as pro-tumorigenic in the context of overactivation of the TGF-β pathway can be explained by the results demonstrating that NOX4 is required for TGF-β-induced migration of HCC cells. Nothing was known in HCC, but other solid tumours suggested that NOX4 is required for an efficient TGF-β-mediated EMT and increase in cell migration[235]. Here we propose the molecular mechanism that may explain these effects. We found that NOX4 is not required for regulation of the EMT-related transcriptional program, but for TGF-β-induced regulation of cytoskeleton dynamics and focal adhesions. Although poorly described in the context of tumorigenesis, a role for NOX4 in regulating cytoskeleton dynamics and focal adhesions was elegantly demonstrated in VSMC[124,125,236]. Particularly, it was proposed that TGF-β, by a NOX4-dependent mechanism, increases Hic-5 expression and localization in focal adhesions, which is essential for the TGF-β-mediated increase in focal adhesions number, adhesive forces and migration[83]. Our results indicate that NOX4 is also required to regulate the levels of Hic-5 and its intracellular localization. NOX4 is required for TGF-β-induced increase in the chaperone Hsp27, a target of NOX4-mediated gene transcription that is required for correct subcellular localization of Hic-5 within focal

adhesions[83]. Additionally, we also observed that NOX4 is essential for TGF-β-mediated regulation of MMP9 expression. Interestingly, it has been proposed that NOX4 and associated reactive oxygen species (ROS) regulate MMP9 expression both at promoter activation and mRNA stability levels[237, 238]. Poorly studied in the context of the TGF-β actions in cancer, MMP9 has been described as an essential regulator of proteins involved in actin polymerization and cell migration during TGF-β-induced EMT in epithelial cells[227]. In vitro results are reinforced by data in patients, indicating the highest expression of *MMP9* or *TGFB1l1* in TGFB1^{high}NOX4^{high} patients. In conclusion, data here presented open new insights about the role of NOX4 in the context of overactivation of the TGF-β pathway in HCC. NOX4 mediates the tumour suppressor actions of TGF-β by regulating Bcl-xL, c-Myc and Cyclin D1. However, NOX4 is also required for regulation of cytoskeleton dynamics and focal adhesions by TGF-β, correlating with changes in expression of Hsp27, Hic-5 and MMP9, which contribute to the migratory capacity of HCC cells. Later on, the Hic-5 result was also corroborated in the DEN mice model when studying the RNAseq analysis (*Tgfb1li1*). Altogether, NOX4 could participate in both suppressor and protumorigenic TGF-β actions in HCC cells (**Figure 49**).

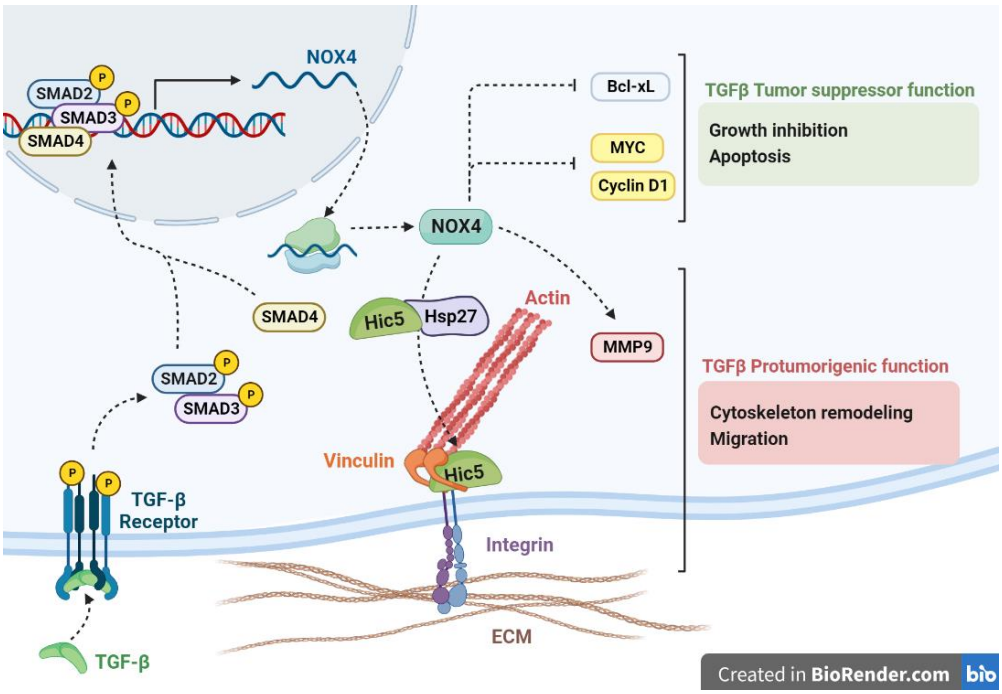

Figure 49. NOX4 plays a dual role in mediating TGF-β actions. Graphical abstract made with BioRender.

2. Role of NOX4 in liver tumorigenic progression in mice models

In any research, translationality of the basic knowledge developed is utterly important. In here, we worked with a model of DEN-induced hepatocarcinogenesis, which is a model that often resembles the human HCC in terms of mutagenesis[239,228,240]. Even if NOX4 -/- mice did not develop a higher number of tumours, as seen in other solid tumours, they did have an increased proliferation rate[232]. Nox4 has also been described in other models as a tumour suppressor protein, as it facilitated the DNA damage recognition[241]. DEN hepatocarcinogenesis is well-characterized as an inflammatory model, rather than a fibrotic one[228,240,229]. Indeed, some macrovesicular and microvesicular steatosis was observed in the H-E staining, but no fibrosis, often seen in HCC patients as fibrotic bridges[242, 243]. This was not found either when analysing fibroblast features, such as α-SMA staining or Collagen1. Fibroblasts showed a differential disposition depending on if the tumour and stroma expressed *Nox4* or not. Strangely, collagen fibres did not follow the fibroblast pathway, encapsulating the tumoral areas, as sometimes can be found in solid tumours[244, 245]. Specifically, NOX4KO mice have been seen to have a hepatic fibrosis decrease, concordant with fewer α-SMA positive-fibroblasts[147]. However, these results were shown in another model, with carbon tetrachloride (CCl_4), which courses with fibrosis.

Another tumour microenvironment characteristic that needs to be considered is the immune system landscape. Specially in HCC, where one of the first-line therapeutic options is Atezolizumab/Bevacizumab, a combination of an anti-PDL1 and an anti-VEGF, understanding the immune system implications is crucial[246]. We know that silencing NOX4 in HCC cell lines increases the redox state, thus increasing the ROS production, in those cells[133]. Therefore, we could think that tumoral cells in NOX4 -/- mice might also have a pathogenic redox state, which has clearly been related to carcinogenic processes, by DNA damage caused by oxidization of nucleosides[247, 248].

The immune system function, especially that of phagocytic cells, is regulated by ROS, too. The oxidative burst is a rapid release of hydrogen peroxide and superoxide into the phagosomes, where ROS act as bactericide effectors[249, 101]. NOX2, a member of the NOXs family, is crucial for this effect, and therefore, is tightly regulated on the phagosomal membrane upon Rac-dependent activation[250,251]. However, NOX4 has not been linked to this phagocytic function. Some studies in arthritic mice had pointed at Nox1 as responsible for the inflammatory response in monocytes/macrophages, challenging the thought that Nox1 is a non-phagocytic isoform of NADPH oxidase[252]. However, others had previously analysed inflammatory cell infiltration related with Nox4 in a fibrotic/carcinogenic model with CCl_4. Overall, less F4/80 staining was seen in NOX4KO mice, accompanied by less gene expression of *TNFα*, *IL-1β* and other pro-inflammatory cytokines[147]. In this study, not only we corroborate these findings, but also, we explore further. We demonstrate in our DEN mice model, through different RNAseq analysis, that NOX4 -/- mice have a downregulated overall immune system. This suggests a role of NOX4 as a regulator of some immunological pathways, particularly implicated in CD8+ T cells and macrophages. On the contrary, others have described an increased inflammation in *Nox4* deficient mice in terms of increased pro-inflammatory cytokines, and a macrophage polarization to M1-like macrophages[253]. Nevertheless, these findings were done in a fibrosarcoma model, where effect of Nox4 might not be as tightly regulated as is in the liver, under TGF-β activation.

The expression of NOX4 in macrophages is a controversial topic, inconsistent throughout the literature, suggesting that NOX4 expression might be volatile over macrophage's phenotype. For instance, it has been reported to drive cell death in monocytes and macrophages in response to oxidized low density lipoproteins (oxLDL), through its ROS production[254,255]. Another model where NOX4 has been shown to modulate the phenotype of macrophage is in lung macrophages asbestosis, where they became more profibrotic[200]. In fact, our NOX4 -/- model proposes a phenotypical switch of macrophages towards an anti-inflammatory (M2-like) polarization when *Nox4* is silenced, thus corroborating the *in vitro* spheroids results. Nonetheless, this mice model is a total knock out of the protein, which can

be a downside when wondering whose Nox4 is exerting these results, the one from the macrophages or the one from the tumour. In fact, an inducible knock out of hepatocytes or of macrophages would be the best suited model to better study this interactions, as other studies demonstrate[200, 256].

In conclusion, understanding Nox4's role could provide insights into the dual nature of ROS in cancer development and potential therapeutic approaches.

3. Role of NOX4 in the interactome between HCC 3D spheroids and macrophages

With the main goal of deepening in the interactome between HCC cells and macrophages, we set up a 3D multicellular spheroid model, which also allows us to better explore the TGF-β-NOX4 axis in this situation. In the last years, 3D spheroids have emerged as a widely used tool to better study the molecular and cellular mechanisms, compared to 2D cellular culture. In fact, some have described metabolic differences in pancreatic and colorectal cancers between 2D and 3D cultures, demonstrating that cell-cell and cell-matrix interactions can be critical for mimicking the tumour environment[257]. Therefore, spheroids are a good model as they can provide more physiological results as a pre-step to *in vivo* research. Proof of this is that liver spheroids made with HepG2 cell line have shown a maintenance of some liver-specific functions such as albumin production, urea synthesis and cytochrome activity[258]. Following the *in vivo* accuracy, several 3D spheroids have been seen to have proliferative kinetics similar to *in vivo* tumours[259]. Nevertheless, variability in the composition and structure of spheroids may present some challenges in the reproducibility of experiments, especially in drug resistance or toxicology research[260]. Moreover, a better standardization of the 3D cell culture protocol is further needed. Some difficulties to reach this aim are the diversity among all the cellular lines[260, 261]. For instance, several formation methods are described, which must be chosen depending on the cell needs[262]. In this project, we have optimized the protocol as a scaffold-free system, particularly performing the hanging drop method. Although scaffold-based systems may confer additional information with the cell-

matrix interactions, this methodology grants a better spheroid size control and, therefore, has better reproducibility[262261].

Overall, 3D spheroids offer a more accurate and robust model for liver cancer research, making them a valuable tool for studying tumour biology and testing new therapies. One of the spheroid features that caught our attention was the "holes" found in PLC ShControl ones. Although further experiments would be needed to correctly answer this question, we thought that they could be due to one of two reasons. Firstly, even though we have not worked with big spheroids (>400μm), as they grow, oxygen and nutrient supply must be limited to the sphere core[261]. Secondary necrosis has widely been described, mainly characterized by Haematoxylin-Eosin immunohistochemistry[263264265]. PLC/PRF/5 ShControl spheroids may be displaying some necrotic features in the spheroid core, as the morphology resembles this death type, which disappeared in the ShNOX4 spheroids. Those showed a better structural maintenance, that was also maintained when treated with TGF-β. Additionally, this result is further corroborated with the MTS assay result, that shows how PLC/PRF/5 ShControl are less viable than ShNOX4 ones. Cell viability assays are an indirect method to detect a possible necrotic process [266], despite the fact that further experiments would be required to conclude that. Secondly, some suggest that HCC organoids, in some conditions, can undergo a reconformation of the structure of the spheroid. In this case, a polarized hole is created, as seen in some studies with Hep3B 3D cultures [267]. However, in other tumoroid models from patient-derived cells, this feature has not been described [268]. All in all, further characterization should be done to suggest a polarization like this in our model.

Necrosis in this 3D spheroids usually is closely related to hypoxia, as oxygen gradient creates a hypoxic core surrounded by a proliferative periphery[269, 270, 262]. Indeed, PLC ShControl followed the peripherical proliferation (in terms of Ki67 positive nuclei), even when treated with TGF-β. Interestingly, when PLC ShNOX4 were treated with TGF-β, this growth front was lost, and the proliferation could be seen throughout all the spheroid. This was accompanied with less loss of tissue in the centre of the sphere, suggesting a better response to hypoxic

conditions in those cells were NOX4 is silenced. Previous results from the group that show how NOX4-silenced cells have an increased oxidative stress[133] propose a possible explanation for the protective state from putative necrotic processes in PLC ShNOX4. Moreover, spheroid analysis in PLC ShNOX4 showed an unexpected response to TGF-β treatment, as spheroid formation was impaired and there were a great number of unattached cells. Nevertheless, characterization of the structure, with H-E staining but also with immunofluorescence of E-Cadherin and N-Cadherin, did not elucidate the reason of this unexpected response. Obviously, the expected loss of E-Cadherin levels when silencing NOX4 were seen, as previously described in the group[219]. Further investigation is needed to unravel the mechanisms by which TGF-β-NOX4 axis affects the spheroids conformation, and how they respond to 3D conditions.

On the other hand, in order to study the interaction between monocyte/macrophage cells and HCC cells, we set up a model of multicellular spheroids, a co-culture with THP-1 monocytic cell line. Pathophysiologically, monocytes are likely to encounter activating or pro-inflammatory cytokines before reaching the tumoral site. That is the reason why they were pre-activated with TGF-β prior to the formation of co-culture spheroids by hanging drop protocol[271, 272]. Finally, this 3D multicellular spheroid approach suggested two main ideas. Firstly, addition of pre-activated THP-1 in the TGF-β-treated PLC ShNOX4 condition, reversed the disaggregation of the spheroids. Therefore, macrophages seem to be contributing to the formation and maintenance of NOX4-silenced spheroids when treated with TGF-β. This idea was contributed with the bigger area quantified in the co-culture with PLC/PRF/5 ShNOX4. An interesting fact was the observation that THP-1 presence provoked an increased ratio nuclei/area in NOX4-silenced cells, that was accompanied by an increased proliferation. Nevertheless, PLC ShControl spheroids maintained the same Ki67 proliferative rate, while had a smaller area and a smaller number of nuclei, indicating that cells were probably dying. Secondly, a deeper analysis of macrophagic recruitment and position was needed, as some differences could be intuited. This brought us to analyse CD68, as an undifferentiated macrophage marker[273], and CD163, as an M2-like macrophage marker[274, 275], also known as anti-inflammatory macrophage.

Results from conditioned media recruitment indicate that although PLC/PRF/5 ShNOX4 cells secrete more chemotactic factors, that recruit more efficiently monocytes, those monocytes differentiate into a phenotypically different macrophage depending on the presence or absence of NOX4 in the tumour. Overall, *in vitro* results suggest that tumours might have a differentiated interaction with monocytes/macrophages depending on NOX4 levels. An improvement in this model might be the use of Bone Marrow-derived Macrophages (BMDM), widely used primary macrophages because they usually provide a more physiological model[276].

CONCLUSIONS

1. NOX4 mediates the tumour suppressor actions of TGF-β by regulating proliferation (c-Myc, Cyclin D1) and apoptosis (Bcl-xL).

2. However, high levels of *TGFB1* and *NOX4* in HCC patients correlated with worse overall survival.

3. NOX4 also regulates TGF-β pro-tumorigenic actions by modulating cytoskeleton dynamics and focal adhesions, which correlate with Hsp27 and Hic-5 alterations.

4. *In vivo* model of DEN-induced hepatocarcinogenesis reflects that loss of NOX4 in HCC influences not only the tumour cell behaviour, but also the tumour microenvironment. The syngeneic orthotopic model suggested that is NOX4 in tumoral cells who modulates stroma cells.

5. RNAseq analysis *in vivo* showed a downregulation in immune system activation, specifically a decrease in CD8+ T cells and an increase in M2-like macrophages in NOX4 -/- mice.

6. *In vitro* experiments with conditioned media from HCC 3D spheroids demonstrate that NOX4 expression levels in tumour cells regulates the macrophages phenotype towards an anti-inflammatory (low NOX4) or pro-inflammatory (high NOX4) behaviour.

REFERENCES

1. Nagaraju, G. P., Dariya, B., Kasa, P., Peela, S. & El-Rayes, B. F. Epigenetics in hepatocellular carcinoma. Seminars in Cancer Biology vol. 86 622–632 Preprint at https://doi.org/10.1016/j.semcancer.2021.07.017 (2022).

2. Rumgay, H. et al. Global, regional and national burden of primary liver cancer by subtype. Eur J Cancer 161, 108–118 (2022).

3. Llovet, J. M. et al. Hepatocellular carcinoma. Nature Reviews Disease Primers vol. 7 Preprint at https://doi.org/10.1038/s41572-020-00240-3 (2021).

4. Kim, E. & Viatour, P. Hepatocellular carcinoma: old friends and new tricks. Experimental and Molecular Medicine vol. 52 1898–1907 Preprint at https://doi.org/10.1038/s12276-020-00527-1 (2020).

5. Craig, A. J., von Felden, J., Garcia-Lezana, T., Sarcognato, S. & Villanueva, A. Tumour evolution in hepatocellular carcinoma. Nature Reviews Gastroenterology and Hepatology vol. 17 139–152 Preprint at https://doi.org/10.1038/s41575-019-0229-4 (2020).

6. Blach, S. et al. Global change in hepatitis C virus prevalence and cascade of care between 2015 and 2020: a modelling study. Lancet Gastroenterol Hepatol 7, 396–415 (2022).

7. Tan, Z. B. & Zhang, J. Recent advances in treatment strategies for hepatocellular carcinoma with portal vein cancer thrombus. Eur Rev Med Pharmacol Sci 27, 8119–8134 (2023).

8. Llovet, J. M. et al. Hepatocellular carcinoma. Nat Rev Dis Primers 2, (2016).

9. Müller, M., Bird, T. G. & Nault, J. C. The landscape of gene mutations in cirrhosis and hepatocellular carcinoma. Journal of Hepatology vol. 72 990–1002 Preprint at https://doi.org/10.1016/j.jhep.2020.01.019 (2020).

10. Guichard, C. et al. Integrated analysis of somatic mutations and focal copy-number changes identifies key genes and pathways in hepatocellular carcinoma. Nat Genet 44, 694–698 (2012).

11. Lee, J. S. The mutational landscape of hepatocellular carcinoma. Clinical and molecular hepatology vol. 21 220–229 Preprint at https://doi.org/10.3350/cmh.2015.21.3.220 (2015).

12. Chen, R., Lin, M. & Gao, D. Major genomic mutations driving hepatocellular carcinoma. Genome Instab Dis 4, 239–253 (2023).

13. Llovet, J. M., Montal, R., Sia, D. & Finn, R. S. Molecular therapies and precision medicine for hepatocellular carcinoma. Nature Reviews Clinical Oncology vol. 15 599–616 Preprint at https://doi.org/10.1038/s41571-018-0073-4 (2018).

14. Demory, A., Nault, J. & Jean Verdier, H. Molecular Perspectives for the Treatment of Hepatocellular Carcinoma.

15. Fabregat, I. & Caballero-Díaz, D. Transforming growth factor-β-induced cell plasticity in liver fibrosis and hepatocarcinogenesis. Frontiers in Oncology vol. 8 Preprint at https://doi.org/10.3389/fonc.2018.00357 (2018).

16. Tzavlaki, K. & Moustakas, A. TGF-B signaling. Biomolecules vol. 10 Preprint at https://doi.org/10.3390/biom10030487 (2020).

17. Batlle, E. & Massagué, J. Transforming Growth Factor-β Signaling in Immunity and Cancer. Immunity vol. 50 924–940 Preprint at https://doi.org/10.1016/j.immuni.2019.03.024 (2019).

18. Santibanez, J. F., Obradovic´, H. O., Kukolj, T., Krstic´3, J. & Krstic´3, K. Transforming Growth Factor-b, Matrix Metalloproteinases, and Urokinase-Type Plasminogen Activator Interaction in the Cancer Epithelial to Mesenchymal Transition. doi:10.1002/dvdy.

19. Dewidar, B., Meyer, C., Dooley, S. & Meindl-Beinker, N. Tgf-β in hepatic stellate cell activation and liver fibrogenesis—updated 2019. Cells vol. 8 Preprint at https://doi.org/10.3390/cells8111419 (2019).

20. Liu, M. & Chen, P. Proliferation-inhibiting pathways in liver regeneration (Review). Molecular Medicine Reports vol. 16 23–35 Preprint at https://doi.org/10.3892/mmr.2017.6613 (2017).

21. Fabregat, I. et al. TGF-β signalling and liver disease. FEBS Journal 2219–2232 (2016) doi:10.1111/febs.13665.

22. Massagué, J. TGFβ in Cancer. Cell vol. 134 215–230 Preprint at https://doi.org/10.1016/j.cell.2008.07.001 (2008).

23. Massagué, J. TGFβ signalling in context. Nature Reviews Molecular Cell Biology vol. 13 616–630 Preprint at https://doi.org/10.1038/nrm3434 (2012).

24. Herranz-Itúrbide, M., Peñuelas-Haro, I., Espinosa-Sotelo, R., Bertran, E. & Fabregat, I. The TGF-β /NADPH oxidases axis in the regulation of liver cell biology in health and disease. Cells vol. 10 Preprint at https://doi.org/10.3390/cells10092312 (2021).

25. Macias, M. J., Martin-Malpartida, P. & Massagué, J. Structural determinants of Smad function in TGF-β signaling. Trends in Biochemical Sciences vol. 40 296–308 Preprint at https://doi.org/10.1016/j.tibs.2015.03.012 (2015).

26. Xin, X., Cheng, X., Zeng, F., Xu, Q. & Hou, L. The Role of TGF-ß/SMAD Signaling in Hepatocellular Carcinoma: from Mechanism to Therapy and Prognosis. International Journal of Biological Sciences vol. 20 1436–1451 Preprint at https://doi.org/10.7150/ijbs.89568 (2024).

27. Seoane, J. Escaping from the TGFβ anti-proliferative control. Carcinogenesis vol. 27 2148–2156 Preprint at https://doi.org/10.1093/carcin/bgl068 (2006).

28. Derynck, R. & Budi, E. H. Specificity, Versatility, and Control of TGF-b Family Signaling. https://www.science.org (2019).

29. Derynck, R. & Budi, E. H. Specificity, Versatility, and Control of TGF-b Family Signaling. https://www.science.org (2019).

30. Jingwen, B., Yaochen, L. & Guojun, Z. Cell cycle regulation and anticancer drug discovery. Cancer Biol Med 14, 348 (2017).

31. Drabsch, Y. & Ten Dijke, P. TGF-β signalling and its role in cancer progression and metastasis. Cancer and Metastasis Reviews 31, 553–568 (2012).

32. Decker, J. T., Ma, J. A., Shea, L. D. & Jeruss, J. S. Implications of TGFβ signaling and Cdk inhibition for the treatment of breast cancer. Cancers vol. 13 Preprint at https://doi.org/10.3390/cancers13215343 (2021).

33. Petritsch, C., Beug, H., Baimain, A. & Oft, M. TGF-β inhibits p70 S6 kinase via protein phosphatase 2A to induce G1 arrest. Genes Dev 14, 3093–3101 (2000).

34. Moustakas, A. & Heldin, C. H. Non-Smad TGF-β signals. Journal of Cell Science vol. 118 3573–3584 Preprint at https://doi.org/10.1242/jcs.02554 (2005).

35. Sánchez, A., Álvarez, A. M., Benito, M. & Fabregat, I. Apoptosis induced by transforming growth factor-β in fetal hepatocyte primary cultures: Involvement of reactive oxygen intermediates. Journal of Biological Chemistry 271, 7416–7422 (1996).

36. Padua, D. & Massagué, J. Roles of TGFβ in metastasis. Cell Research vol. 19 89–102 Preprint at https://doi.org/10.1038/cr.2008.316 (2009).

37. Taylor, R. C., Cullen, S. P. & Martin, S. J. Apoptosis: Controlled demolition at the cellular level. Nature Reviews Molecular Cell Biology vol. 9 231–241 Preprint at https://doi.org/10.1038/nrm2312 (2008).

38. Tait, S. W. G. & Green, D. R. Mitochondria and cell death: Outer membrane permeabilization and beyond. Nature Reviews Molecular Cell Biology vol. 11 621–632 Preprint at https://doi.org/10.1038/nrm2952 (2010).

39. Wright, K. M., Linhoff, M. W., Potts, P. R. & Deshmukh, M. Decreased apoptosome activity with neuronal differentiation sets the threshold for strict IAP regulation of apoptosis. Journal of Cell Biology 167, 303–313 (2004).

40. Gama, V. et al. The E3 ligase PARC mediates the degradation of cytosolic cytochrome c to promote survival in neurons and cancer cells. Sci Signal (2014) doi:10.1126/scisignal.2005309.

41. Tait, S. W. G., Ichim, G. & Green, D. R. Die another way - non-apoptotic mechanisms of cell death. J Cell Sci 127, 2135–2144 (2014).

42. Bid, a Bcl2 Interacting Protein, Mediates Cytochrome c Release from Mitochondria in Response to Activation of Cell Surface Death Receptors.

43. Czabotar, P. E., Lessene, G., Strasser, A. & Adams, J. M. Control of apoptosis by the BCL-2 protein family: Implications for physiology and therapy. Nature Reviews Molecular Cell Biology vol. 15 49–63 Preprint at https://doi.org/10.1038/nrm3722 (2014).

44. Llambi, F. et al. A Unified Model of Mammalian BCL-2 Protein Family Interactions at the Mitochondria. Mol Cell 44, 517–531 (2011).

45. Cleavage of BID by Caspase 8 Mediates the Mitochondrial Damage in the Fas Pathway of Apoptosis.

46. Franklin, C. C., Rosenfeld-Franklin, M. E., White, C., Kavanagh, T. J. & Fausto, N. TGFβ1-induced suppression of glutathione antioxidant defenses in hepatocytes: caspase-dependent posttranslational and caspase-independent transcriptional regulatory mechanisms. The FASEB Journal (2003).

47. Ramesh, S., Wildey, G. M. & Howe, P. H. Transforming Growth Factor β (TGFβ)-Induced Apoptosis: The Rise & Fall of Bim.

48. Schuster, N. & Krieglstein, K. Mechanisms of TGF-β-mediated apoptosis. Cell and Tissue Research vol. 307 1–14 Preprint at https://doi.org/10.1007/s00441-001-0479-6 (2002).

49. Herrera, B. et al. Activation of caspases occurs downstream from radical oxygen species production, Bcl-xL down-regulation, and early cytochrome c release in apoptosis induced by transforming growth factor β in rat fetal hepatocytes. Hepatology 34, 548–556 (2001).

50. Herrera, B. et al. Reactive Oxygen Species (ROS) Mediates the Mitochondrial-Dependent Apoptosis Induced by Transforming Growth Factor in Fetal Hepatocytes.

51. Herrera, B. et al. Source of early reactive oxygen species in the apoptosis induced by transforming growth factor-β in fetal rat hepatocytes. Free Radic Biol Med 36, 16–26 (2004).

52. Carmona-Cuenca, I. et al. Upregulation of the NADPH oxidase NOX4 by TGF-beta in hepatocytes is required for its pro-apoptotic activity. J Hepatol 49, 965–976 (2008).

53. Liu, S., Ren, J. & ten Dijke, P. Targeting TGFβ signal transduction for cancer therapy. Signal Transduction and Targeted Therapy vol. 6 Preprint at https://doi.org/10.1038/s41392-020-00436-9 (2021).

54. Murillo, M. M. et al. Activation of NADPH oxidase by transforming growth factor-β in hepatocytes mediates up-regulation of epidermal growth factor receptor ligands through a nuclear factor-κB-dependent mechanism. Biochemical Journal 405, 251–259 (2007).

55. Sancho, P. & Fabregat, I. NADPH oxidase NOX1 controls autocrine growth of liver tumor cells through up-regulation of the epidermal growth factor receptor pathway. Journal of Biological Chemistry 285, 24815–24824 (2010).

56. Carmona-Cuenca, I. et al. EGF blocks NADPH oxidase activation by TGF-β in fetal rat hepatocytes, impairing oxidative stress, and cell death. J Cell Physiol 207, 322–330 (2006).

57. Caja, L. et al. Overactivation of the MEK/ERK pathway in liver tumor cells confers resistance to TGF-β-induced cell death through impairing up-regulation of the NADPH oxidase NOX4. Cancer Res 69, 7595–7602 (2009).

58. Murillo, M. M., Del Castillo, G., Sánchez, A., Fernández, M. & Fabregat, I. Involvement of EGF receptor and c-Src in the survival signals induced by TGF-β1 in hepatocytes. Oncogene 24, 4580–4587 (2005).

59. Caja, L., Sancho, P., Bertran, E. & Fabregat, I. Dissecting the effect of targeting the epidermal growth factor receptor on TGF-β-induced-apoptosis in human hepatocellular carcinoma cells. J Hepatol 55, 351–358 (2011).

60. Caja, L. et al. Differential intracellular signalling induced by TGF-β in rat adult hepatocytes and hepatoma cells: Implications in liver carcinogenesis. Cell Signal 19, 683–694 (2007).

61. Moreno-Càceres, J. et al. Caveolin-1 is required for TGF-ß-induced transactivation of the EGF receptor pathway in hepatocytes through the activation of the metalloprotease TACE/ADAM17. Cell Death Dis 5, (2014).

62. Moreno-Càceres, J. et al. Caveolin-1-dependent activation of the metalloprotease TACE/ADAM17 by TGF-β in hepatocytes requires activation of Src and the NADPH oxidase NOX1. FEBS J 283, 1300–1310 (2016).

63. Caballero-Díaz, D. et al. Clathrin switches transforming growth factor-β role to pro-tumorigenic in liver cancer. J Hepatol 72, 125–134 (2020).

64. Sancho, P. et al. The inhibition of the epidermal growth factor (EGF) pathway enhances TGF-β-induced apoptosis in rat hepatoma cells through inducing oxidative stress coincident with a change in the expression pattern of the NADPH oxidases (NOX) isoforms. Biochim Biophys Acta Mol Cell Res 1793, 253–263 (2009).

65. Bertran, E. et al. Overactivation of the TGF-β pathway confers a mesenchymal-like phenotype and CXCR4-dependent migratory properties to liver tumor cells. Hepatology 58, 2032–2044 (2013).

66. Morrison, C. D., Parvani, J. G. & Schiemann, W. P. The relevance of the TGF-β Paradox to EMT-MET programs. Cancer Letters vol. 341 30–40 Preprint at https://doi.org/10.1016/j.canlet.2013.02.048 (2013).

67. Lamouille, S., Xu, J. & Derynck, R. Molecular mechanisms of epithelial-mesenchymal transition. Nature Reviews Molecular Cell Biology vol. 15 178–196 Preprint at https://doi.org/10.1038/nrm3758 (2014).

68. Katsuno, Y., Lamouille, S. & Derynck, R. TGF-β signaling and epithelial-mesenchymal transition in cancer progression. Current Opinion in Oncology vol. 25 76–84 Preprint at https://doi.org/10.1097/CCO.0b013e32835b6371 (2013).

69. Wang, X., Eichhorn, P. J. A. & Thiery, J. P. TGF-β, EMT, and resistance to anti-cancer treatment. Seminars in Cancer Biology vol. 97 1–11 Preprint at https://doi.org/10.1016/j.semcancer.2023.10.004 (2023).

70. Hao, Y., Baker, D. & Dijke, P. Ten. TGF-β-mediated epithelial-mesenchymal transition and cancer metastasis. International Journal of Molecular Sciences vol. 20 Preprint at https://doi.org/10.3390/ijms20112767 (2019).

71. Heldin, C. H., Vanlandewijck, M. & Moustakas, A. Regulation of EMT by TGFβ in cancer. FEBS Letters vol. 586 1959–1970 Preprint at https://doi.org/10.1016/j.febslet.2012.02.037 (2012).

72. Sá Nchez, A. et al. Apoptotic Response to TGF-<beta> in Fetal Hepatocytes Depends upon Their State of Differentiation. http://www.idealibrary.com (1999).

73. Malfettone, A. et al. Transforming growth factor-β-induced plasticity causes a migratory stemness phenotype in hepatocellular carcinoma. Cancer Lett 392, 39–50 (2017).

74. Bertran, E. et al. Role of CXCR4/SDF-1α in the migratory phenotype of hepatoma cells that have undergone epithelial-mesenchymal transition in response to the transforming growth factor-β. Cell Signal 21, 1595–1606 (2009).

75. Lee, J. H. & Massagué, J. TGF-β in developmental and fibrogenic EMTs. Seminars in Cancer Biology vol. 86 136–145 Preprint at https://doi.org/10.1016/j.semcancer.2022.09.004 (2022).

76. Valdés, F. et al. Transforming growth factor-beta activates both pro-apoptotic and survival signals in fetal rat hepatocytes. Exp Cell Res 292, 209–218 (2004).

77. Vega, S. et al. Snail blocks the cell cycle and confers resistance to cell death. Genes Dev 18, 1131–1143 (2004).

78. Franco, D. L. et al. Snail1 suppresses TGF-β-induced apoptosis and is sufficient to trigger EMT in hepatocytes. J Cell Sci 123, 3467–3477 (2010).

79. del Castillo, G. et al. Autocrine production of TGF-β confers resistance to apoptosis after an epithelial-mesenchymal transition process in hepatocytes: Role of EGF receptor ligands. Exp Cell Res 312, 2860–2871 (2006).

80. Lyle, A. N. & Griendling, K. K. Modulation of Vascular Smooth Muscle Signaling by Reactive Oxygen Species. Physiology 21, 269–280 (2006).

81. Bedard, K. & Krause, K.-H. The NOX Family of ROS-Generating NADPH Oxidases: Physiology and Pathophysiology. (2007) doi:10.1152/physrev.00044.2005.-For.

82. Block, K. & Gorin, Y. Aiding and abetting roles of NOX oxidases in cellular transformation. Nature Reviews Cancer vol. 12 627–637 Preprint at https://doi.org/10.1038/nrc3339 (2012).

83. Fernandez, I. et al. Hic-5 mediates TGFβ-induced adhesion in vascular smooth muscle cells by a Nox4-dependent mechanism. Arterioscler Thromb Vasc Biol 35, 1198–1206 (2015).

84. Brown, D. I. & Griendling, K. K. Nox proteins in signal transduction. Free Radical Biology and Medicine vol. 47 1239–1253 Preprint at https://doi.org/10.1016/j.freeradbiomed.2009.07.023 (2009).

85. Babior, B. M., Lambeth, J. D. & Nauseef, W. The neutrophil NADPH oxidase. Arch Biochem Biophys 397, 342–344 (2002).

86. Bedard, K. & Krause, K.-H. The NOX Family of ROS-Generating NADPH Oxidases: Physiology and Pathophysiology. (2007) doi:10.1152/physrev.00044.2005.-For.

87. Schröder, K. NADPH oxidases: Current aspects and tools: NADPH oxidase current tools. Redox Biology vol. 34 Preprint at https://doi.org/10.1016/j.redox.2020.101512 (2020).

88. Dickinson, B. C. & Chang, C. J. Chemistry and biology of reactive oxygen species in signaling or stress responses. Nature Chemical Biology vol. 7 504–511 Preprint at https://doi.org/10.1038/nchembio.607 (2011).

89. Radi, R. Oxygen radicals, nitric oxide, and peroxynitrite: Redox pathways in molecular medicine. Proc Natl Acad Sci U S A 115, 5839–5848 (2018).

90. Sies, H. & Jones, D. P. Reactive oxygen species (ROS) as pleiotropic physiological signalling agents. Nature Reviews Molecular Cell Biology vol. 21 363–383 Preprint at https://doi.org/10.1038/s41580-020-0230-3 (2020).

91. Sies, H., Berndt, C. & Jones, D. P. Oxidative Stress. (2017) doi:10.1146/annurev-biochem.

92. Fukai, T. & Ushio-Fukai, M. Cross-Talk between NADPH Oxidase and Mitochondria: Role in ROS Signaling and Angiogenesis. Cells vol. 9 Preprint at https://doi.org/10.3390/cells9081849 (2020).

93. Reczek, C. R. & Chandel, N. S. The two faces of reactive oxygen species in cancer. Annu Rev Cancer Biol 1, 79–98 (2017).

94. Altenhöfer, S. et al. The NOX toolbox: Validating the role of NADPH oxidases in physiology and disease. Cellular and Molecular Life Sciences vol. 69 2327–2343 Preprint at https://doi.org/10.1007/s00018-012-1010-9 (2012).

95. Sies, H. Hydrogen peroxide as a central redox signaling molecule in physiological oxidative stress: Oxidative eustress. Redox Biology vol. 11 613–619 Preprint at https://doi.org/10.1016/j.redox.2016.12.035 (2017).

96. Szanto, I. NADPH Oxidase 4 (NOX4) in Cancer: Linking Redox Signals to Oncogenic Metabolic Adaptation. International Journal of Molecular Sciences vol. 23 Preprint at https://doi.org/10.3390/ijms23052702 (2022).

97. Sies, H. Oxidative eustress: On constant alert for redox homeostasis. Redox Biology vol. 41 Preprint at https://doi.org/10.1016/j.redox.2021.101867 (2021).

98. Sies, H. Oxidative eustress and oxidative distress: Introductory remarks. in Oxidative Stress: Eustress and Distress 3–12 (Elsevier, 2019). doi:10.1016/B978-0-12-818606-0.00001-8.

99. Lambris, J. D. Advances in Experimental Medicine and Biology. http://www.springer.com/series/5584.

100. Bienert, G. P. & Chaumont, F. Aquaporin-facilitated transmembrane diffusion of hydrogen peroxide. Biochimica et Biophysica Acta - General Subjects vol. 1840 1596–1604 Preprint at https://doi.org/10.1016/j.bbagen.2013.09.017 (2014).

101. Vermot, A., Petit-Härtlein, I., Smith, S. M. E. & Fieschi, F. Nadph oxidases (Nox): An overview from discovery, molecular mechanisms to physiology and pathology. Antioxidants 10, (2021).

102. Nisimoto, Y., Diebold, B. A., Constentino-Gomes, D. & Lambeth, J. D. Nox4: A hydrogen peroxide-generating oxygen sensor. Biochemistry 53, 5111–5120 (2014).

103. Breitenbach, M. et al. The defense and signaling role of NADPH oxidases in eukaryotic cells: Review. Wiener Medizinische Wochenschrift 168, 286–299 (2018).

104. Geiszt, M., Kopp, J. B., ter Vá rnai, P. & Leto, T. L. Identification of Renox, an NAD(P)H Oxidase in Kidney. www.pnas.orgcgidoi10.1073pnas.130135897.

105. Shiose, A. et al. A novel superoxide-producing NAD(P)H oxidase in kidney. Journal of Biological Chemistry 276, 1417–1423 (2001).

106. Ogboo, B. C. et al. Architecture of the NADPH oxidase family of enzymes. Redox Biology vol. 52 Preprint at https://doi.org/10.1016/j.redox.2022.102298 (2022).

107. Schröder, K., Wandzioch, K., Helmcke, I. & Brandes, R. P. Nox4 acts as a switch between differentiation and proliferation in preadipocytes. Arterioscler Thromb Vasc Biol 29, 239–245 (2009).

108. Guo, S. & Chen, X. The human Nox4: Gene, structure, physiological function and pathological significance. Journal of Drug Targeting vol. 23 888–896 Preprint at https://doi.org/10.3109/1061186X.2015.1036276 (2015).

109. Von Löhneysen, K., Noack, D., Hayes, P., Friedman, J. S. & Knaus, U. G. Constitutive NADPH oxidase 4 activity resides in the composition of the B-loop and the penultimate C terminus. Journal of Biological Chemistry 287, 8737–8745 (2012).

110. Takac, I. et al. The E-loop is involved in hydrogen peroxide formation by the NADPH oxidase Nox4. Journal of Biological Chemistry 286, 13304–13313 (2011).

111. Goyal, P. et al. Identification of novel Nox4 splice variants with impact on ROS levels in A549 cells. Biochem Biophys Res Commun 329, 32–39 (2005).

112. Serrander, L. et al. NOX4 activity is determined by mRNA levels and reveals a unique pattern of ROS generation. Biochemical Journal 406, 105–114 (2007).

113. Chen, F., Haigh, S., Barman, S. & Fulton, D. J. R. From form to function: The role of Nox4 in the cardiovascular system. Front Physiol 3 NOV, (2012).

114. Matsushima, S. et al. Tyrosine kinase FYN negatively regulates NOX4 in cardiac remodeling. Journal of Clinical Investigation 126, 3403–3416 (2016).

115. Lorenzo, A. F. G. et al. Heat shock protein 70 and CHIP promote Nox4 ubiquitination and degradation within the losartan antioxidative effect in proximal tubule cells. Cellular Physiology and Biochemistry 36, 2183–2197 (2015).

116. Palumbo, S. et al. Dysregulated Nox4 ubiquitination contributes to redox imbalance and age-related severity of acute lung injury. Am J Physiol Lung Cell Mol Physiol 312, 297–308 (2017).

117. Block, K., Gorin, Y. & Abboud, H. E. Subcellular Localization of Nox4 and Regulation in Diabetes. www.pnas.org/cgi/content/full/.

118. Shanmugasundaram, K. et al. NOX4 functions as a mitochondrial energetic sensor coupling cancer metabolic reprogramming to drug resistance. Nat Commun 8, (2017).

119. Prior, K. K. et al. The endoplasmic reticulum chaperone calnexin is a NADPH oxidase NOX4 interacting protein. Journal of Biological Chemistry 291, 7045–7059 (2016).

120. Helmcke, I., Heumü Ller, S., Tikkanen, R., Schröder, K. & Brandes, R. P. Identification of Structural Elements in Nox1 and Nox4 Controlling Localization and Activity. Antioxid Redox Signal 11, (2009).

121. Chen, K., Kirber, M. T., Xiao, H., Yang, Y. & Keaney, J. F. Regulation of ROS signal transduction by NADPH oxidase 4 localization. Journal of Cell Biology 181, 1129–1139 (2008).

122. Kuroda, J. et al. The superoxide-producing NAD(P)H oxidase Nox4 in the nucleus of human vascular endothelial cells. Genes to Cells 10, 1139–1151 (2005).

123. Eun, H. et al. High nuclear NADPH oxidase 4 expression levels are correlated with cancer development and poor prognosis in hepatocellular carcinoma. Pathology 51, 579–585 (2019).

124. Hilenski, L. L., Clempus, R. E., Quinn, M. T., Lambeth, J. D. & Griendling, K. K. Distinct Subcellular Localizations of Nox1 and Nox4 in Vascular Smooth Muscle Cells. Arterioscler Thromb Vasc Biol 24, 677–683 (2004).

125. Clempus, R. E. et al. Nox4 is required for maintenance of the differentiated vascular smooth muscle cell phenotype. Arterioscler Thromb Vasc Biol 27, 42–48 (2007).

126. Yan, S. R. & Berton, G. Regulation of Src family tyrosine kinase activities in adherent human neutrophils. Journal of Biological Chemistry 271, 23464–23471 (1996).

127. Vukelic, S. et al. Nox4 (NADPH oxidase 4) and PolDIP2 (polymerase δ-interacting protein 2) induce filamentous actin oxidation and promote its interaction with vinculin during integrin-mediated cell adhesion. Arterioscler Thromb Vasc Biol 38, 2423–2434 (2018).

128. Gough, N. R., Xiang, X. & Mishra, L. TGF-β Signaling in Liver, Pancreas, and Gastrointestinal Diseases and Cancer. Gastroenterology vol. 161 434-452.e15 Preprint at https://doi.org/10.1053/j.gastro.2021.04.064 (2021).

129. Crosas-Molist, E. & Fabregat, I. Role of NADPH oxidases in the redox biology of liver fibrosis. Redox Biology vol. 6 106–111 Preprint at https://doi.org/10.1016/j.redox.2015.07.005 (2015).

130. Senturk, S. et al. Transforming growth factor-beta induces senescence in hepatocellular carcinoma cells and inhibits tumor growth. Hepatology 52, 966–974 (2010).

131. Yu, J. H., Zhu, B. M., Riedlinger, G., Kang, K. & Hennighausen, L. The liver-specific tumor suppressor STAT5 controls expression of the reactive oxygen species-generating enzyme NOX4 and the proapoptotic proteins PUMA and BIM in mice. Hepatology 56, 2375–2386 (2012).

132. Crosas-Molist, E. et al. The NADPH oxidase NOX4 inhibits hepatocyte proliferation and liver cancer progression. Free Radic Biol Med 69, 338–347 (2014).

133. Peñuelas-Haro, I. et al. The NADPH oxidase NOX4 regulates redox and metabolic homeostasis preventing hepatocellular carcinoma progression. Hepatology (2022) doi:10.1002/hep.32702.

134. Ha, S. Y. et al. NADPH Oxidase 1 and NADPH oxidase 4 have opposite prognostic effects for patients with hepatocellular carcinoma after hepatectomy. Gut Liver 10, 826–835 (2016).

135. Eun, H. S. et al. Gene expression of NOX family members and their clinical significance in hepatocellular carcinoma. Sci Rep 7, (2017).

136. Lu, C. et al. NADPH oxidase DUOX1 and DUOX2 but not NOX4 are independet predictors in hepatocellular carcinoma after hepatectomy. Tumour Biology 32, 1173–1182 (2011).

137. Meitzler, J. L. et al. Decoding NADPH oxidase 4 expression in human tumors. Redox Biol 13, 182–195 (2017).

138. Gong, S., Wang, S. & Shao, M. NADPH Oxidase 4: A Potential Therapeutic Target of Malignancy. Frontiers in Cell and Developmental Biology vol. 10 Preprint at https://doi.org/10.3389/fcell.2022.884412 (2022).

139. Jiang, F., Liu, G. S., Dusting, G. J. & Chan, E. C. NADPH oxidase-dependent redox signaling in TGF-β-mediated fibrotic responses. Redox Biology vol. 2 267–272 Preprint at https://doi.org/10.1016/j.redox.2014.01.012 (2014).

140. Barry, A. E. et al. Hepatic Stellate Cells and Hepatocarcinogenesis. Frontiers in Cell and Developmental Biology vol. 8 Preprint at https://doi.org/10.3389/fcell.2020.00709 (2020).

141. Dooley, S., Delvoux, B., Lahme, B., Mangasser-Stephan, K. & Gressner, A. M. Modulation of transforming growth factor β response and signaling during

transdifferentiation of rat hepatic stellate cells to myofibroblasts. Hepatology 31, 1094–1106 (2000).

142. Crosas-Molist, E. & Fabregat, I. Role of NADPH oxidases in the redox biology of liver fibrosis. Redox Biology vol. 6 106–111 Preprint at https://doi.org/10.1016/j.redox.2015.07.005 (2015).

143. Proell, V. et al. TGF-β dependent regulation of oxygen radicals during transdifferentiation of activated hepatic stellate cells to myofibroblastoid cells. Comp Hepatol 6, (2007).

144. Sancho, P. et al. NADPH Oxidase NOX4 Mediates Stellate Cell Activation and Hepatocyte Cell Death during Liver Fibrosis Development. PLoS One 7, (2012).

145. Cui, W. et al. NOX1/nicotinamide adenine dinucleotide phosphate, reduced form (NADPH) oxidase promotes proliferation of stellate cells and aggravates liver fibrosis induced by bile duct ligation. Hepatology 54, 949–958 (2011).

146. Paik, Y. H. et al. The nicotinamide adenine dinucleotide phosphate oxidase (NOX) homologues NOX1 and NOX2/gp91phox mediate hepatic fibrosis in mice. Hepatology 53, 1730–1741 (2011).

147. Lan, T., Kisseleva, T. & Brenner, D. A. Deficiency of NOX1 or NOX4 prevents liver inflammation and fibrosis in mice through inhibition of hepatic stellate cell activation. PLoS One 10, (2015).

148. Dooley, S. & Ten Dijke, P. TGF-β in progression of liver disease. Cell and Tissue Research vol. 347 245–256 Preprint at https://doi.org/10.1007/s00441-011-1246-y (2012).

149. Ding, Z. Y. et al. Transforming growth factor β induces expression of connective tissue growth factor in hepatic progenitor cells through Smad independent signaling. Cell Signal 25, 1981–1992 (2013).

150. Liu, Y. et al. Transforming growth factor-β (TGF-β)-mediated connective tissue growth factor (CTGF) expression in hepatic stellate cells requires Stat3 signaling activation. Journal of Biological Chemistry 288, 30708–30719 (2013).

151. Jiang, J. X., Mikami, K., Venugopal, S., Li, Y. & Török, N. J. Apoptotic body engulfment by hepatic stellate cells promotes their survival by the JAK/STAT and Akt/NF-κB-dependent pathways. J Hepatol 51, 139–148 (2009).

152. Brenner, C., Galluzzi, L., Kepp, O. & Kroemer, G. Decoding cell death signals in liver inflammation. Journal of Hepatology vol. 59 583–594 Preprint at https://doi.org/10.1016/j.jhep.2013.03.033 (2013).

153. Jiang, J. X. et al. Reduced nicotinamide adenine dinucleotide phosphate oxidase 2 plays a key role in stellate cell activation and liver fibrogenesis in Vivo. Gastroenterology 139, (2010).

154. Yin, C., Evason, K. J., Asahina, K. & Stainier, D. Y. R. Hepatic stellate cells in liver development, regeneration, and cancer. Journal of Clinical Investigation vol. 123 1902–1910 Preprint at https://doi.org/10.1172/JCI66369 (2013).

155. Yang, W. et al. Single-Cell Transcriptomic Analysis Reveals a Hepatic Stellate Cell-Activation Roadmap and Myofibroblast Origin During Liver Fibrosis in Mice. LIVER BIOLOGY/ PATHOBIOLOGY | Hepatology 74, 2021 (2021).

156. Ying, F., Chan, M. S. M. & Lee, T. K. W. Cancer-Associated Fibroblasts in Hepatocellular Carcinoma and Cholangiocarcinoma. CMGH vol. 15 985–999 Preprint at https://doi.org/10.1016/j.jcmgh.2023.01.006 (2023).

157. Kalluri, R. The biology and function of fibroblasts in cancer. Nature Reviews Cancer vol. 16 582–598 Preprint at https://doi.org/10.1038/nrc.2016.73 (2016).

158. Yao, Y. et al. Prediction of CAF-related genes in immunotherapy and drug sensitivity in hepatocellular carcinoma: a multi-database analysis. Genes Immun 25, 55–65 (2024).

159. Park, Y. N., Kim, Y.-B., Yang, K. M. & Chanil, ; Increased Expression of Vascular Endothelial Growth Factor and Angiogenesis in the Early Stage of Multistep Hepatocarcinogenesis. Arch Pathol Lab Med vol. 124 (2000).

160. Winkler, J., Abisoye-Ogunniyan, A., Metcalf, K. J. & Werb, Z. Concepts of extracellular matrix remodelling in tumour progression and metastasis. Nature Communications vol. 11 Preprint at https://doi.org/10.1038/s41467-020-18794-x (2020).

161. Li, Y. et al. Cancer-associated fibroblasts promote the stemness of CD24 + liver cells via paracrine signaling. J Mol Med 97, 243–255 (2019).

162. Xiong, S. et al. Cancer-associated fibroblasts promote stem cell-like properties of hepatocellular carcinoma cells through IL-6/STAT3/Notch signaling. Am J Cancer Res 8, 302–316 (2018).

163. Zhu, G. Q. et al. CD36+ cancer-associated fibroblasts provide immunosuppressive microenvironment for hepatocellular carcinoma via secretion of macrophage migration inhibitory factor. Cell Discov 9, (2023).

164. Morén, A. et al. LXRα limits TGFβ-dependent hepatocellular carcinoma associated fibroblast differentiation. Oncogenesis 8, (2019).

165. Mikula, M., Proell, V., Fischer, A. N. M. & Mikulits, W. Activated hepatic stellate cells induce tumor progression of neoplastic hepatocytes in a TGF-β dependent fashion. J Cell Physiol 209, 560–567 (2006).

166. Liu, J. et al. Cancer-associated fibroblasts promote hepatocellular carcinoma metastasis through chemokine-activated hedgehog and TGF-β pathways. Cancer Lett 379, 49–59 (2016).

167. Song, M. et al. Cancer-Associated Fibroblast-Mediated Cellular Crosstalk Supports Hepatocellular Carcinoma Progression. Hepatology 73, 2021 (2021).

168. Shi, X., Young, C. D., Zhou, H. & Wang, X. Transforming growth factor-β signaling in fibrotic diseases and cancer-associated fibroblasts. Biomolecules vol. 10 1–22 Preprint at https://doi.org/10.3390/biom10121666 (2020).

169. Chen, J., Gingold, J. A. & Su, X. Immunomodulatory TGF-β Signaling in Hepatocellular Carcinoma. Trends in Molecular Medicine vol. 25 1010–1023 Preprint at https://doi.org/10.1016/j.molmed.2019.06.007 (2019).

170. Sia, D. et al. Identification of an Immune-specific Class of Hepatocellular Carcinoma, Based on Molecular Features. Gastroenterology 153, 812–826 (2017).

171. Gabrielson, A. et al. Intratumoral CD3 and CD8 T-cell densities associated with relapse-free survival in HCC. Cancer Immunol Res 4, 419–430 (2016).

172. Wang, J., Zhao, X. & Wan, Y. Y. Intricacies of TGF-β signaling in Treg and Th17 cell biology. Cellular and Molecular Immunology vol. 20 1002–1022 Preprint at https://doi.org/10.1038/s41423-023-01036-7 (2023).

173. Vignali, D. A. A., Collison, L. W. & Workman, C. J. How regulatory T cells work. Nature Reviews Immunology vol. 8 523–532 Preprint at https://doi.org/10.1038/nri2343 (2008).

174. Fontenot, J. D., Gavin, M. A. & Rudensky, A. Y. Foxp3 programs the development and function of CD4+CD25+ regulatory T cells. Journal of Immunology 198, 986–992 (2017).

175. Konkel, J. E. et al. Transforming Growth Factor-β Signaling in Regulatory T Cells Controls T Helper-17 Cells and Tissue-Specific Immune Responses. Immunity 46, 660–674 (2017).

176. Qin, H. et al. TGF-β Promotes Th17 Cell Development through Inhibition of SOCS3. The Journal of Immunology 183, 97–105 (2009).

177. Lee, Y. et al. Induction and molecular signature of pathogenic T H 17 cells. Nat Immunol 13, 991–999 (2012).

178. Ciofani, M. et al. A validated regulatory network for Th17 cell specification. Cell 151, 289–303 (2012).

179. Thomas, D. A. & Massagué, J. TGF-β directly targets cytotoxic T cell functions during tumor evasion of immune surveillance. Cancer Cell 8, 369–380 (2005).

180. David, C. J. & Massagué, J. Contextual determinants of TGFβ action in development, immunity and cancer. Nature Reviews Molecular Cell Biology vol. 19 419–435 Preprint at https://doi.org/10.1038/s41580-018-0007-0 (2018).

181. Crispe, I. N. Liver antigen-presenting cells. Journal of Hepatology vol. 54 357–365 Preprint at https://doi.org/10.1016/j.jhep.2010.10.005 (2011).

182. Liu, Z. et al. Fate Mapping via Ms4a3-Expression History Traces Monocyte-Derived Cells. Cell 178, 1509-1525.e19 (2019).

183. Sunderkötter, C. et al. Subpopulations of Mouse Blood Monocytes Differ in Maturation Stage and Inflammatory Response. The Journal of Immunology 172, 4410–4417 (2004).

184. Geissmann, F., Jung, S. & Littman, D. R. Blood Monocytes Consist of Two Principal Subsets with Distinct Migratory Properties. Immunity 19, 71–82 (2003).

185. Tran, S. et al. Impaired Kupffer Cell Self-Renewal Alters the Liver Response to Lipid Overload during Non-alcoholic Steatohepatitis. Immunity 53, 627-640.e5 (2020).

186. Ren, C. X. et al. Intratumoral and peritumoral expression of CD68 and CD206 in hepatocellular carcinoma and their prognostic value. Oncol Rep 38, 886–898 (2017).

187. Yunna, C., Mengru, H., Lei, W. & Weidong, C. Macrophage M1/M2 polarization. European Journal of Pharmacology vol. 877 Preprint at https://doi.org/10.1016/j.ejphar.2020.173090 (2020).

188. Chen, S. et al. Macrophages in immunoregulation and therapeutics. Signal Transduction and Targeted Therapy vol. 8 Preprint at https://doi.org/10.1038/s41392-023-01452-1 (2023).

189. Tremble, L. F. et al. Differential association of CD68+ and CD163+ macrophages with macrophage enzymes, whole tumour gene expression and overall survival in advanced melanoma. Br J Cancer 123, 1553–1561 (2020).

190. Ming Hu, J. et al. CD163 as a Marker of M2 Macrophage, Contribute to Predict Aggressiveness and Prognosis of Kazakh Esophageal Squamous Cell Carcinoma. Oncotarget vol. 8 www.impactjournals.com/oncotarget/ (2017).

191. Strizova, Z. et al. M1/M2 macrophages and their overlaps - myth or reality? Clinical Science vol. 137 1067–1093 Preprint at https://doi.org/10.1042/CS20220531 (2023).

192. Roszer, T. Understanding the mysterious M2 macrophage through activation markers and effector mechanisms. Mediators of Inflammation vol. 2015 Preprint at https://doi.org/10.1155/2015/816460 (2015).

193. Balkwill, F. R. & Mantovani, A. Cancer-related inflammation: Common themes and therapeutic opportunities. Seminars in Cancer Biology vol. 22 33–40 Preprint at https://doi.org/10.1016/j.semcancer.2011.12.005 (2012).

194. Zhang, W. et al. Depletion of tumor-associated macrophages enhances the effect of sorafenib in metastatic liver cancer models by antimetastatic and antiangiogenic effects. Clinical Cancer Research 16, 3420–3430 (2010).

195. Ho, D. W. H. et al. Single-cell RNA sequencing shows the immunosuppressive landscape and tumor heterogeneity of HBV-associated hepatocellular carcinoma. Nat Commun 12, (2021).

196. Liang, S. et al. NADPH Oxidase 1 in Liver Macrophages Promotes Inflammation and Tumor Development in Mice. Gastroenterology 156, 1156-1172.e6 (2019).

197. Vandierendonck, A. et al. NOX1 inhibition attenuates the development of a pro-tumorigenic environment in experimental hepatocellular carcinoma. Journal of Experimental and Clinical Cancer Research 40, (2021).

198. Shiau, D. J. et al. Hepatocellular carcinoma-derived high mobility group box 1 triggers M2 macrophage polarization via a TLR2/NOX2/autophagy axis. Sci Rep 10, (2020).

199. Teufelhofer, O. et al. Superoxide generation from Kupffer cells contributes to hepatocarcinogenesis: Studies on NADPH oxidase knockout mice. Carcinogenesis 26, 319–329 (2005).

200. He, C. et al. NOX4 modulates macrophage phenotype and mitochondrial biogenesis in asbestosis. JCI Insight 4, (2019).

201. Larson-Casey, J. L., Gu, L., Kang, J., Dhyani, A. & Brent Carter, A. NOX4 regulates macrophage apoptosis resistance to induce fibrotic progression. Journal of Biological Chemistry 297, (2021).

202. Zhang, J. et al. Tumoral NOX4 recruits M2 tumor-associated macrophages via ROS/PI3K signaling-dependent various cytokine production to promote NSCLC growth. Redox Biol 22, (2019).

203. Carnesecchi, S. et al. A key role for NOX4 in epithelial cell death during development of lung fibrosis. Antioxid Redox Signal 15, 607–619 (2011).

204. Lopez-Luque, J. et al. Dissecting the Role of Epidermal Growth Factor Receptor Catalytic Activity During Liver Regeneration and Hepatocarcinogenesis. (2016) doi:10.1002/hep.28134/suppinfo.

205. Ruiz de Galarreta, M. et al. β-Catenin Activation Promotes Immune Escape and Resistance to Anti-PD-1 Therapy in Hepatocellular Carcinoma HHS Public Access.

206. Chen, S., Zhou, Y., Chen, Y. & Gu, J. Fastp: An ultra-fast all-in-one FASTQ preprocessor. in Bioinformatics vol. 34 i884–i890 (Oxford University Press, 2018).

207. Dobin, A. et al. STAR: Ultrafast universal RNA-seq aligner. Bioinformatics 29, 15–21 (2013).

208. Li, B. & Dewey, C. N. RSEM: Accurate transcript quantification from RNA-Seq data with or without a reference genome. BMC Bioinformatics 12, (2011).

209. Liberzon, A. et al. The Molecular Signatures Database Hallmark Gene Set Collection. Cell Syst 1, 417–425 (2015).

210. Hänzelmann, S., Castelo, R. & Guinney, J. GSVA: Gene Set Variation Analysis for Microarray and RNA-Seq Data. BMC Bioinformatics vol. 14 http://www.biomedcentral.com/1471-2105/14/7http://www.bioconductor.org.Background (2013).

211. Merotto, L., Sturm, G., Dietrich, A., List, M. & Finotello, F. Making mouse transcriptomics deconvolution accessible with immunedeconv. Bioinformatics Advances 4, (2024).

212. Li, T. et al. TIMER2.0 for analysis of tumor-infiltrating immune cells. Nucleic Acids Res 48, W509–W514 (2020).

213. Ally, A. et al. Comprehensive and Integrative Genomic Characterization of Hepatocellular Carcinoma. Cell 169, 1327-1341.e23 (2017).

214. Cumbo, F., Fiscon, G., Ceri, S., Masseroli, M. & Weitschek, E. TCGA2BED: Extracting, extending, integrating, and querying The Cancer Genome Atlas. BMC Bioinformatics 18, (2017).

215. Grossman, R. L. et al. Toward a Shared Vision for Cancer Genomic Data. New England Journal of Medicine 375, 1109–1112 (2016).

216. Celià-Terrassa, T. et al. Normal and cancerous mammary stem cells evade interferon-induced constraint through the MIR-199a-LCOR axis. Nat Cell Biol 19, 711–723 (2017).

217. Zaidi, S., Gough, N. R. & Mishra, L. Mechanisms and clinical significance of TGF-β in hepatocellular cancer progression. in Advances in Cancer Research vol. 156 227–248 (Academic Press Inc., 2022).

218. Gonzalez-Sanchez, E. et al. The TGF-β pathway: A pharmacological target in hepatocellular carcinoma? Cancers vol. 13 Preprint at https://doi.org/10.3390/cancers13133248 (2021).

219. Crosas-Molist, E. et al. The NADPH oxidase NOX4 represses epithelial to amoeboid transition and efficient tumour dissemination. Oncogene 36, 3002–3014 (2017).

220. Mateyak, M. K., Obaya, A. J. & Sedivy, J. M. C-Myc Regulates Cyclin D-Cdk4 and-Cdk6 Activity but Affects Cell Cycle Progression at Multiple Independent Points.

MOLECULAR AND CELLULAR BIOLOGY vol. 19 https://journals.asm.org/journal/mcb (1999).

221. Zentella, A., Weis, F. M. B., Ralph, D. A., Laiho, M. & Massaguel, J. Early Gene Responses to Transforming Growth Factor-,B in Cells Lacking Growth-Suppressive RB Function. MOLECULAR AND CELLULAR BIOLOGY vol. 11 (1991).

222. Sanchez, A., Alvarez, M., Benito, M. & Fabrecat, I. Transforming Growth Factor F5 Modulates Growth and Differentiation of Fetal Hepatocytes in Primary Culture. JOURNAL OF CEI,l,ULAR PHYSIOLOGY vol. 165 (1995).

223. Ramjaun, A. R., Tomlinson, S., Eddaoudi, A. & Downward, J. Upregulation of two BH3-only proteins, Bmf and Bim, during TGFβ-induced apoptosis. Oncogene 26, 970–981 (2007).

224. Soukupova, J. et al. Epithelial–mesenchymal transition (Emt) induced by tgf-β in hepatocellular carcinoma cells reprograms lipid metabolism. Int J Mol Sci 22, (2021).

225. Ungefroren, H., Witte, D. & Lehnert, H. The Role of Small GTPases of the Rho/Rac Family in TGF-B-induced EMT and Cell Motility in Cancer. Dev Dyn (2018) doi:10.1002/dvdy.24505.

226. Santibáñez, J. F., Kocić, J., Fabra, A., Cano, A. & Quintanilla, M. Rac1 modulates TGF-β1-mediated epithelial cell plasticity and MMP9 production in transformed keratinocytes. FEBS Lett 584, 2305–2310 (2010).

227. Liu, Z. Z., Taiyab, A. & West-Mays, J. A. MMP9 differentially regulates proteins involved in actin polymerization and cell migration during TGF-β-induced EMTin the Lens. Int J Mol Sci 22, (2021).

228. Schulien, I. & Hasselblatt, P. Diethylnitrosamine-induced liver tumorigenesis in mice. in Methods in Cell Biology vol. 163 137–152 (Academic Press Inc., 2021).

229. Memon, A., Pyao, Y., Jung, Y., Lee, J. Il & Lee, W. K. A modified protocol of diethylnitrosamine administration in mice to model hepatocellular carcinoma. Int J Mol Sci 21, 1–13 (2020).

230. Bruix, J., da Fonseca, L. G. & Reig, M. Insights into the success and failure of systemic therapy for hepatocellular carcinoma. Nature Reviews Gastroenterology and Hepatology vol. 16 617–630 Preprint at https://doi.org/10.1038/s41575-019-0179-x (2019).

231. Rizvi, F. et al. Simvastatin reduces TGF-β1-induced SMAD2/3-dependent human ventricular fibroblasts differentiation: Role of protein phosphatase activation. Int J Cardiol 270, 228–236 (2018).

232. Helfinger, V. et al. Genetic deletion of Nox4 enhances cancerogen-induced formation of solid tumors. doi:10.1073/pnas.2020152118/-/DCSupplemental.

233. Jong, H. S. et al. Attenuation of transforming growth factor β-induced growth inhibition in human hepatocellular carcinoma cell lines by cyclin D1 overexpression. Biochem Biophys Res Commun 292, 383–389 (2002).

234. Meyer, C., Liu, Y., Kaul, A., Peipe, I. & Dooley, S. Caveolin-1 abrogates TGF-β mediated hepatocyte apoptosis. Cell Death Dis 4, (2013).

235. Tobar, N., Guerrero, J., Smith, P. C. & Martínez, J. NOX4-dependent ROS production by stromal mammary cells modulates epithelial MCF-7 cell migration. Br J Cancer 103, 1040–1047 (2010).

236. Jiménez-Altayó, F. et al. Redox stress in Marfan syndrome: Dissecting the role of the NADPH oxidase NOX4 in aortic aneurysm. Free Radic Biol Med 118, 44–58 (2018).

237. Liu, Z. M., Tseng, H. Y., Tsai, H. W., Su, F. C. & Huang, H. S. Transforming growth factor β-interacting factor-induced malignant progression of hepatocellular carcinoma cells depends on superoxide production from Nox4. Free Radic Biol Med 84, 54–64 (2015).

238. Doppler, W. & Jansen-Dürr, P. Regulation of mitochondrial ROS production by HIC-5: a common feature of oncogene-induced senescence and tumor invasiveness? FEBS Journal vol. 286 456–458 Preprint at https://doi.org/10.1111/febs.14746 (2019).

239. Lee, J. S. et al. Application of comparative functional genomics to identify best-fit mouse models to study human cancer. Nat Genet 36, 1306–1311 (2004).

240. Zhang, Q. et al. Proteomic analysis of DEN and CCl4-induced hepatocellular carcinoma mouse model. Sci Rep 14, (2024).

241. Helfinger, V. et al. Hydrogen peroxide formation by Nox4 limits malignant transformation. doi:10.1101/177055.

242. Renne, S. L. et al. Hepatocellular carcinoma: A clinical and pathological overview. Pathologica vol. 113 203 Preprint at https://doi.org/10.32074/1591-951X-295 (2021).

243. Antonio Díaz, L., Antonio Díaz, L. P. & Barrera, F. M. Clasificaciones En Gastroenterología Clasificación Barcelona Clinic Liver Cancer (BCLC) de Carcinoma Hepatocelular. Gastroenterol. latinoam vol. 26 (2015).

244. Willumsen, N. et al. Fibrotic activity quantified in serum by measurements of type III collagen pro-peptides can be used for prognosis across different solid tumor types. Cellular and Molecular Life Sciences vol. 79 Preprint at https://doi.org/10.1007/s00018-022-04226-0 (2022).

245. Shah, K. Targeting Tumour-Associated Fibroblasts in Cancers. Frontiers in Oncology vol. 12 Preprint at https://doi.org/10.3389/fonc.2022.908156 (2022).

246. Ntellas, P. & Chau, I. Updates on Systemic Therapy for Hepatocellular Carcinoma. American Society of Clinical Oncology Educational Book 44, (2024).

247. Salehi, F., Behboudi, H., Kavoosi, G. & Ardestani, S. K. Oxidative DNA damage induced by ROS-modulating agents with the ability to target DNA: A comparison of the biological characteristics of citrus pectin and apple pectin. Sci Rep 8, (2018).

248. Srinivas, U. S., Tan, B. W. Q., Vellayappan, B. A. & Jeyasekharan, A. D. ROS and the DNA damage response in cancer. Redox Biology vol. 25 Preprint at https://doi.org/10.1016/j.redox.2018.101084 (2019).

249. Paino, I. M. M. et al. Phagocytosis, oxidative burst, and produced reactive species are affected by iron deficiency anemia and anemia of chronic diseases in elderly. Biol Trace Elem Res 129, 116–125 (2009).

250. Nunes, P., Demaurex, N. & Dinauer, M. C. Regulation of the NADPH Oxidase and Associated Ion Fluxes During Phagocytosis. Traffic vol. 14 1118–1131 Preprint at https://doi.org/10.1111/tra.12115 (2013).

251. Hoang, H. M., Johnson, H. E. & Heo, J. Rac-dependent feedforward autoactivation of NOX2 leads to oxidative burst. Journal of Biological Chemistry 297, (2021).

252. Matsumoto, M. et al. NOX1/NADPH oxidase is involved in the LPS-induced exacerbation of collagen-induced arthritis. J Pharmacol Sci 146, 88–97 (2021).

253. Helfinger, V., Palfi, K., Weigert, A. & Schröder, K. The NADPH oxidase Nox4 controls macrophage polarization in an NFκB-dependent manner. Oxid Med Cell Longev 2019, (2019).

254. Lee, C. F., Qiao, M., Schröder, K., Zhao, Q. & Asmis, R. Nox4 is a novel inducible source of reactive oxygen species in monocytes and macrophages and mediates oxidized low density lipoprotein-induced macrophage death. Circ Res 106, 1489–1497 (2010).

255. Canton, M. et al. Reactive Oxygen Species in Macrophages: Sources and Targets. Frontiers in Immunology vol. 12 Preprint at https://doi.org/10.3389/fimmu.2021.734229 (2021).

256. Zhang, M. et al. Both cardiomyocyte and endothelial cell Nox4 mediate protection against hemodynamic overload-induced remodelling. Cardiovasc Res 114, 401–408 (2018).

257. Tidwell, T. R., Røsland, G. V., Tronstad, K. J., Søreide, K. & Hagland, H. R. Metabolic flux analysis of 3D spheroids reveals significant differences in glucose metabolism from matched 2D cultures of colorectal cancer and pancreatic ductal adenocarcinoma cell lines. Cancer Metab 10, (2022).

258. Štampar, M., Breznik, B., Filipič, M. & Žegura, B. Characterization of In Vitro 3D Cell Model Developed from Human Hepatocellular Carcinoma (HepG2) Cell Line. Cells 9, (2020).

259. Huang, B. W. & Gao, J. Q. Application of 3D cultured multicellular spheroid tumor models in tumor-targeted drug delivery system research. Journal of Controlled Release vol. 270 246–259 Preprint at https://doi.org/10.1016/j.jconrel.2017.12.005 (2018).

260. Ivascu, A. & Kubbies, M. Rapid generation of single-tumor spheroids for high-throughput cell function and toxicity analysis. J Biomol Screen 11, 922–932 (2006).

261. Han, S. J., Kwon, S. & Kim, K. S. Challenges of applying multicellular tumor spheroids in preclinical phase. Cancer Cell International vol. 21 Preprint at https://doi.org/10.1186/s12935-021-01853-8 (2021).

262. Mitrakas, A. G. et al. Applications and Advances of Multicellular Tumor Spheroids: Challenges in Their Development and Analysis. International Journal of Molecular Sciences vol. 24 Preprint at https://doi.org/10.3390/ijms24086949 (2023).

263. Shi, W. et al. Facile Tumor Spheroids Formation in Large Quantity with Controllable Size and High Uniformity. Sci Rep 8, (2018).

264. BOGAJEWSKA-RYLKO, E. et al. When is immunohistochemistry useful in assessing tumor necrotic tissue? Anticancer Res 41, 197–201 (2021).

265. Yakavets, I. et al. Advanced co-culture 3D breast cancer model for investigation of fibrosis induced by external stimuli: optimization study. Sci Rep 10, (2020).

266. Dominijanni, A. J., Devarasetty, M., Forsythe, S. D., Votanopoulos, K. I. & Soker, S. Cell Viability Assays in Three-Dimensional Hydrogels: A Comparative Study of Accuracy. Tissue Eng Part C Methods 27, 401–410 (2021).

267. Oz, O., Iscan, E., Batur, T. & Ozturk, M. 3d organoid modelling of hepatoblast-like and mesenchymal-like hepatocellular carcinoma cell lines. Hepatoma Res 7, (2021).

268. Broutier, L. et al. Human primary liver cancer-derived organoid cultures for disease modeling and drug screening. Nat Med 23, 1424–1435 (2017).

269. Grimes, D. R. et al. The role of oxygen in avascular tumor growth. PLoS One 11, (2016).

270. Grimes, D. R. & Fletcher, A. G. Close Encounters of the Cell Kind: The Impact of Contact Inhibition on Tumour Growth and Cancer Models. Bull Math Biol 82, (2020).

271. Wang, A. & Fu, L. Fibronectin regulates the activation of THP-1 cells by TGF-b. Inflammation Research (2001) doi:1023-3830/01/030142-7 $ 1.50+0.20/0.

272. Michael, D. R., Salter, R. C. & Ramji, D. P. TGF-β inhibits the uptake of modified low density lipoprotein by human macrophages through a Smad-dependent pathway: A dominant role for Smad-2. Biochim Biophys Acta Mol Basis Dis 1822, 1608–1616 (2012).

273. Chistiakov, D. A., Killingsworth, M. C., Myasoedova, V. A., Orekhov, A. N. & Bobryshev, Y. V. CD68/macrosialin: Not just a histochemical marker. Laboratory Investigation 97, 4–13 (2017).

274. Ming Hu, J. et al. CD163 as a Marker of M2 Macrophage, Contribute to Predict Aggressiveness and Prognosis of Kazakh Esophageal Squamous Cell Carcinoma. Oncotarget vol. 8 www.impactjournals.com/oncotarget/ (2017).

275. Kwiecień, I. et al. CD163 and CCR7 as markers for macrophage polarization in lung cancer microenvironment. Central European Journal of Immunology 44, 395–402 (2019).

276. Xie, D. K. et al. Phenotypic comparison and the potential antitumor function of immortalized bone marrow-derived macrophages (iBMDMs). Front Immunol 15, (2024).